NOTE TO USERS

Quantification of air leaks through the building envelope using infrared thermography

Marianne Bérubé Dufour

A thesis

in

The Department

of

Building, Civil and Environmental Engineering

Presented in Partial Fulfillment of the Requirements

for the Degree of Master in Applied Sciences at

Concordia University

Montreal, Quebec, Canada

August 2005

Your file Votre référence
ISBN: 0-494-10216-0
Our file Notre référence
ISBN: 0-494-10216-0

ABSTRACT

Quantification of air leaks through the building envelope using infrared thermography

Marianne Bérubé Dufour, M.A.Sc.

Airtightness defects are the most frequent building envelope failures observed in recently built houses. Whereas thermal insulation levels can be visually controlled on site, the designed level of airtightness is not easily achieved and controlled during the construction process. Air leakage through the building envelope may significantly increase building energy consumption for heating and cooling. Methods such as fan pressurization using a blower door apparatus have been developed for the measurement of the overall airtightness of building envelopes and assemblies. In order to locate precisely air leakage sites throughout the building envelope, infrared thermography is nowadays barely used. For the quantification of the air leaks however no method has been developed yet.

The development of a method for such quantification in terms of crack dimensions using infrared thermography is the objective of this project.

A laboratory experimental procedure has been developed for the acquisition of thermograms of surface temperature distributions due to air leaks through the building envelope. Air leaks through a sample single layer building envelope assembly with a crack of variable width have been reproduced in an environmental chamber inside which conditions met during building envelope thermography surveys were reproduced. The reference emitter technique has been used for the improvement of the accuracy of the

absolute temperature measurements with infrared thermography. A qualitative study of the thermograms obtained is presented highlighting the differences between temperature patterns due air leaks through the assembly under different conditions. Also, quantitative relationships between assembly surface temperature distributions due to air leaks and crack dimensions are established. Two methods are presented and discussed, the first based on image segmentation technique and the second on tomography, for building envelope cracks sizing using infrared thermography. For length of crack, the first method, profiles segmentation, yields measurements extracted from thermograms with a 5% difference and, for width dimension, the last method, profiles calibration, led to measurements with a 16% difference. Therefore, the use of infrared thermography to quantify air leak sites is very promising to be included in energy audit to provide energy savings estimation that would results from repairing air leaks.

Acknowledgments

I have always aspired to pursue graduate studies, but I have never had I a clear idea in which field. I will forever be passionate about architecture, and what I have learned from the architecture school is a rich knowledge that I will never forget. However, I found in building engineering a challenging area to continue my studies. During my Master I found also people that I want to thank.

First I want to thank my supervisor Dominique Derome. She gave me, two years ago, my first chance. Since then, she has always been there, answering my questions and believing in my work but allowing me space to learn on my own. Dominique, you are a role model for me.

I had also the chance to have as supervisor Radu Zmeureanu. I want to thank him for the pertinent feedbacks and ideas on everything I was proposing. He also always took the time to explain the engineering basics which were new to me.

For my Master I had the chance to have as supervisors what I have always looked for in professors.

I must thank the Energy Efficiency Fund of Gaz Métro: they participated in funding an NSERC grant that financially supported me for the last two years. The context of this industrial scholarship gave me the opportunity to start to apply my research in industry. A special thank you to Jean-Pierre Finet.

I could not have done it also without the Concordia faculty, staff and my colleagues. I had the chance to take advantage of the experience of Paul Fazio who was my professor for the majority of my Masters courses. Also, I appreciated very much the help of Luc Demers, Sylvain Belanger and Joe Hrib. Thank you, Guylaine Desmarais; it

helps me so much to have someone that I know who understands. Then the student colleagues, and friends, Hua Ge, Anik Teasdale-St-Hilaire, Luis Candanedo, Sami Chebil, and others: they were often teachers to me. Also, in the last few months, I had the chance to be introduced to researchers from other universities: special thanks to the Belgians for the discussions and ideas.

Actually, this thesis is not an end, but a beginning. I hope to have the chance to work with each of you during the rest of my studies and in my professional work.

Finally, my friends, I could dedicate this thesis to you, Noémie Bernier-Solomon, and Anne and Mimi, among others. This thesis is why sometimes I was not there with you as much as I wanted; but, you have to know that I enjoyed the Master experience a lot. However, without my parents, Jeannine Bérubé and Paul-André Dufour, and my three brothers, Félix, Vincent and François, nothing of this would have been possible.

TABLE OF CONTENTS

LIST OF FIGURES

LIST OF TABLES

NOMENCLATURE

Symbol	Definition	Units
a	*fitted parameter*	-
area	*measured crack area*	m^2
A	*calibration constant*	-
b	*fitted parameter*	-
B	*calibration constant*	-
B_1	*infiltration interaction coefficient*	1/3
c	*fitted parameter*	-
c_p	*specific heat of air*	J/kg*K
C	*power law flow coefficient*	$m^3/s/Pa^n$
C_p	*surface pressure distribution coefficient*	-
C_D	*discharge coefficient for a large opening*	0.6 or 1
D	*distance tested*	m
E_λ	*emissivity power for a blackbody*	$W/(m^2 \cdot \mu m)$
f_s	*stack flow factor*	-
f_w	*wind flow factor*	-
F_{s-e}	*view factor between the surface and the environment*	-
∇f	*gradient of function f*	-
g	*gravity acceleration*	9.8 m/s^2
G	*magnitude of the gradient of the function f*	-

Symbol	Definition	Units
G_x	*magnitude of the gradient of the function f relative to x*	-
G_y	*magnitude of the gradient of the function f relative to y*	-
h (x,y)	*effect of the geometric degradation on the camera response at (x,y)*	camera output units
h_i	*inside surface coefficient*	$W/(m^2 \cdot K)$
h_c	*convection coefficient*	$W/(m^2 \cdot K)$
H	*height of the opening*	m
H_e	*building height eaves height*	m
H_{NPL}	*height of the Neutral Plane Level*	m
i_{fg}	*latent heat of vaporization of water at the temperature of indoor air*	J/kg vapor
I ()	*camera response function*	camera output units
L	*total radiance*	$W/(m^2 \cdot sr)$
L_b	*effective radiance of a blackbody*	$W/(m^2 \cdot sr)$
L_{eff}	*effective radiance*	$W/(m^2 \cdot sr)$
$L_{\lambda,b}$	*spectral radiance of a blackbody*	$W/(m^2 \cdot sr)$
$L_{\lambda,s}$	*surface spectral radiance*	$W/(m^2 \cdot sr \cdot \mu m)$
$\dot{m}$	*moisture accumulation rate*	kg/s
m_c	*humidity content*	kg moisture / kg dry air
$m_{c,out}$	*humidity content at air temperature out*	kg moisture / kg dry air
n_1	*sample sizes*	-
n_2	*sample sizes*	-
n	*power law flow exponent*	-

Symbol	Definition	Units
$n(x,y)$	*effect of noise on the ideal camera at (x,y)*	camera output units
p_w	*surface pressure due to wind*	Pa
Δp	*pressure difference through the building envelope*	Pa
Δp_a	*air pressure difference due to stack effect*	Pa
Δp_r	*reference pressure difference*	Pa
P	*corrected pressure difference*	Pa
P_1	*pressure differences before testing*	Pa
P_2	*pressure differences after testing*	Pa
P_s	*stack effect reference pressure*	Pa
P_{test}	*pressure difference measured*	Pa
P_w	*façade pressure due to wind*	Pa
ΔP	*pressure difference tested*	Pa
q	*air flow rate*	m^3/s
Q	*total airflow rate through the building envelope*	m^3/s
Q_{50}	*predicted airflow rate at 50 Pa*	m^3/s
Q_{env}	*airflow rate corrected*	m^3/s
Q_E	*equivalent airflow calculated*	m^3/s
Q_{fan}	*airflow rate measured*	m^3/s
Q_i	*air infiltration rate*	m^3/s
Q_m	*mass flow rate*	kg/s
Q_r	*predicted airflow rate at the reference pressure difference*	m^3/s

Symbol	Definition	Units
Q_s	*airflow rate due to stack effect*	m^3/s
Q_v	*volumetric flow rate*	m^3/s
Q_{vLFE}	*volume airflow rate measured by laminar flow element*	m^3/s
Q_w	*airflow rate due to wind effect*	m^3/s
R_{wall}	*wall resistance*	$(m^2 \cdot K)/K$
$S(\lambda)$	*sensitivity function for the spectral band*	-
$S[x,y]$	*effect of radiometric degradation on ideal camera response at (x,y)*	camera output units
S_w	*wind shelter coefficient*	-
T	*corrected temperature*	°C
$T(x,y)$	*camera response to the surface temperature and the at (x,y)*	camera output units
T_N	*temperature normalized*	-
T_s	*surface temperature*	K
T_r	*reflected temperature*	K
T_{atm}	*atmosphere temperature*	K
T_e	*environment temperature*	K
T_i	*inside temperature*	°C
T_{IR}	*temperature measured by the camera*	°C
T_{IRref}	*temperature measured by the camera over the reference*	°C
T_o	*outside temperature*	°C
T_{ref}	*temperature measured by the thermocouple over the reference*	°C
T_s	*surface temperature*	K

Symbol	Definition	Units
$T_{s,i}$	*inside surface temperature*	°C
T_p	*panel surface temperature*	°C
TI	*temperature index*	-
ΔT	*temperature difference tested*	°C
ΔT_{IR}	*error on temperature measurement using thermography with a reference emitter*	K
ΔT_{ref}	*reference emitter temperature setting error*	K
ΔT_{TC}	*thermocouple temperature error*	K
ΔT_{FOV}	*error on data inside a field of view of thermograms*	K
U	*wind speed*	m/s
U_e	*unobstructed wind speed at eaves height*	m/s
volume	*volume of the tested building*	m^3
w_e	*estimated crack width*	m
w_m	*measured crack width*	m
W_i	*inside humidity ratio*	kg moisture /kg dry air
W_o	*outside humidity ratio*	kg moisture /kg dry air
X	*longitudinal position*	m
Y	*normalized temperature*	-
	Greek alphabet	
ε	*emissivity of the surface*	-
ε_λ	*spectral emissivity of the surface*	-
μ_1	*mean of sample 1*	m

Symbol	Definition	Units
μ_2	*mean of sample 2*	m
v_o	*specific volume of air*	m^3/kg
ρ_{crack}	*air density at the crack location*	kg/m^3
ρ_{in}	*outside air density*	kg/m^3
ρ_{LFE}	*air density at LFE location*	kg/m^3
ρ_o	*outside air density*	kg/m^3
σ_1	*standard deviation of the sample 1*	m
σ_2	*standard deviation of sample 2*	m
τ	*transmissivity of the atmosphere*	-

Chapter 1 Introduction

1.1 Context

Airtightness defects are the most frequent building envelope failures observed in recently built houses (Dussault 2005). In contrast to thermal insulation levels, the designed level of airtightness is not easily achieved and controlled during the construction process.

Air leakage through the building envelope may significantly increase the building energy consumption for heating and cooling. Since the building sector constitutes a large part, i.e. 30%-35%, of the total energy use, improving the airtightness of building envelopes can result in significant reduction of energy use, which is a major contemporary concern. In fact, airtightness retrofit measures have been found effective measures to decrease energy consumption of buildings for heating and cooling (Zmeureanu 2000 and Zmeureanu *et al* 1998).

Air leakage can also lead to interstitial condensation and moisture accumulation within the envelope. Such moisture occurrence can result in deterioration of materials and reduction of thermal resistance. In addition, the effects on the building envelope of moisture transport by air leaks can be worsened when insulation level retrofit measures are undertaken without improvement on the airtightness (Desmarais 2000).

Methods have been developed for the measurement of the overall airtightness of building envelopes and assemblies. For example, fan pressurization using a blower door apparatus is the common on-site method used to measure the overall airtightness of

houses. The airtightness measurement of houses are given in terms of effective leakage area at 10 Pa and/or air change per hour at 50 Pa pressure difference between outside and inside; these measurements are used for comparison purpose and/or as input for building energy consumption modeling for prediction of retrofit measures savings (Riley 1993).

As a means to locate precisely air leakage sites throughout the building envelope, infrared thermography is nowadays barely used. Thermographic surveys are usually carried out during the depressurization of the building envelope, which is required for the overall airtightness measurement; the depressurization induces cold air infiltration throughout the entire envelope (ASTM 1998). Moreover, studies have shown that thermographic building envelope surveys increase the motivation of owners to undertake the proposed airtightness retrofit measures (Derome *et al* 2004).

For the quantification of the air leaks however, no method has been developed yet. The development of a method for such quantification using infrared thermography is the general objective of this project.

1.2 Objectives

The specific objectives of this project are:

1. To give an overview of the use of infrared thermography for building envelope evaluation in situ and for building envelope research.
2. To develop an experimental set up to reproduce air leakage through the building envelope.

3. To develop an experimental procedure to acquire, in addition to qualitative thermograms, accurate measurements of assembly surface temperature distributions due to air leaks using infrared thermography.
4. To develop a method for the quantification of air leaks through the building envelope in terms of crack dimensions based on measurements with infrared thermography.

An experimental procedure has been developed for the acquisition of thermograms of surface temperature distribution due to air leaks through the building envelope. The tests were carried out in a medium size environmental chamber. The reference emitter technique has been used for the improvement of the accuracy of the absolute temperature measurements with infrared thermography.

Results obtained throughout the experimental procedure have been analyzed to assess the accuracy of the proposed method. A qualitative study of the thermograms and a quantitative analysis of the assembly surface temperature distribution matrices acquired have been done. Two methods have been studied, the first based on image segmentation technique and the second on tomography, for building envelope crack sizing using infrared thermography.

1.3 Thesis organization

The context and objectives of the project have been stated in the previous section of Chapter 1.

Chapter 2 presents the literature review on building envelope, building envelope testing and infrared thermography basics. Then, existing standard methods for infrared thermographic survey are exhaustively presented, compared and analyzed.

The experimental protocol is described in Chapter 3, including the specimen and experimental set up, and the testing conditions reproduced in a medium size environmental chamber. The methods developed for the evaluation of the radiometric measurement parameters, the emissivity, and the ambient and reflected temperatures are discussed.

Also in Chapter 4, a qualitative analysis of the thermograms of the assembly surface temperature distributions due to air leaks is accomplished. The results of a method used for the visualization of the air jet are presented also. Chapter 4 presents also the assembly surface temperature distribution matrices obtained and the methods developed for crack sizing. The lateral and longitudinal temperature profiles are analyzed and their relationships with crack dimensions are highlighted. Based on these relationships, two methods are proposed and evaluated for crack sizing using thermography.

Conclusions, contributions and recommendations for future work are at the end of the thesis in Chapter 5.

Chapter 2 Literature review

The present literature review provides the state-of-the-art knowledge relating to the use of infrared thermography for the quantification of air leaks through the building envelope.

The first section of the literature review presents essential elements to the understanding of building envelope air leakage and the air leakage consequences on the building envelope performance. First the building envelope is presented as a system of interrelated elements and the air barrier concept is introduced. Second, the existing mathematical characterizations of air leakage through the entire building envelope are presented with the calculation methods used for the corresponding thermal loads and moisture accumulation potentials. Actual methods developed for the evaluation of the building envelope performance are presented focusing on airtightness. Methods for entire building envelope airtightness measurement are described in details; however, no method has been found for single air leak measurement.

The second section introduces first the infrared thermography as a non-destructive testing method. The equipment and techniques are described in order to better understand the applications presented then. Since infrared thermography surveys are still barely used when evaluating the building envelope and since surveys results are often incorrectly analyzed by the evaluators (Derome et al 2004), the principles and methods for the use of infrared thermography when evaluating the building envelope energy performance are thoroughly studied in this literature review. Finally, similar building studies using infrared thermography are also summarized and discussed.

2.1 Building envelope

The building envelope answers to basic requirements of structural strength, durability, economy, and aesthetics. In addition, the building envelope functions as a separator between indoor and outdoor environments, allowing to control indoor conditions in acceptable ranges (Hutcheon and Handegord 1983). As a whole, the building envelope must perform as a filter for rain, light, noise, fire as well as flows of heat, water vapor and air. To achieve its functions, the building envelope works has a system of interrelated components with different functions, e.g. air barrier.

2.1.1 Building envelope components

Rain screen system Rain penetration can affect building envelope materials and thus the performance of the envelope. The possible effects of water combined with other phenomena on building envelope are dimensional change, corrosion, decay, mold, blistering, efflorescence, leaching and deterioration (Latta 1962).

Water penetration in the envelope occurs when three factors occur: a water source, an opening and a driving force. It can be prevented by eliminating only one of those factors. Water flowing on envelope can be minimized but not avoided and neither openings. The break of the driving forces can instead be used to prevent rain penetration (Garden 1963). The possible driving forces are kinetic energy, gravity, capillarity and the force due to pressure difference.

As an economical and light substitute to traditional solid masonry or as more resilient systems then sealed finish system, the rain screen wall manages the water

reaching the wall assembly. This type of system is composed of a rain screen, a pressure-equalization chamber, and a watertight air tight back wall as shown in Figure 2.1.

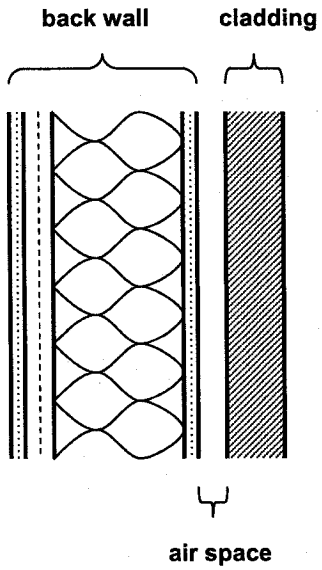

Figure 2.1 Rain screen wall components

Vapor retarder Water vapor diffusion can lead to moisture-accumulation related problems that are similar to rain penetration ones albeit of much smaller magnitude.

A layer with low vapor permeance is introduced in the envelope assembly to decrease the transmission of vapor from the high vapor pressure side (inside in cold climate winter) to low vapor pressure side (outside in cold climate winter) of the building. For example, it should be located at the warm side of the insulation layer in heating climate. The drying of the wall if there is any water introduced by diffusion or any source in the assembly should be allowed by the system.

Insulation High heat losses have an effect on thermal comfort, increase heating and cooling loads, and favor cold surfaces condensation (Ball 1961).

An insulation layer is installed in a building to mainly reduce the flow of heat. The insulation layer can be placed at different locations in the building envelope system: inside the cavities of the stud structure, between furrings at the inside face of the back wall or continuously at the outside face of the back wall. However, the ideal situation is a continuous outside insulation protecting the structure, hence avoiding problems related to thermal bridges.

Air barrier Much more moisture can be introduced in the wall assembly by air leakage than by diffusion phenomenon (Latta 1976). Infiltration and exfiltration also have an effect on comfort and indoor air quality as well as heating and cooling loads (Wilson 1961).

There must be an airtight layer in the assembly; the placement is, however, less critical than for the vapor tight layer. Also, the air barrier must be sufficiently strong or supported to resist wind loads. Any penetration of the air barrier should be sealed to insure continuity.

2.1.2 Building envelope systems

Various materials and techniques are constantly being developed so that the building envelope improves its performance in the control of heat, water and air flows. The functions of the building envelope can be achieved by different material layers and, sometimes, the same layer can have more than one function. The best practices proposed by CMHC's for woodframe envelopes (CMHC 1999) offer examples of different

building envelope assemblies. Below are three variations of air barrier approaches (Figure 2.2).

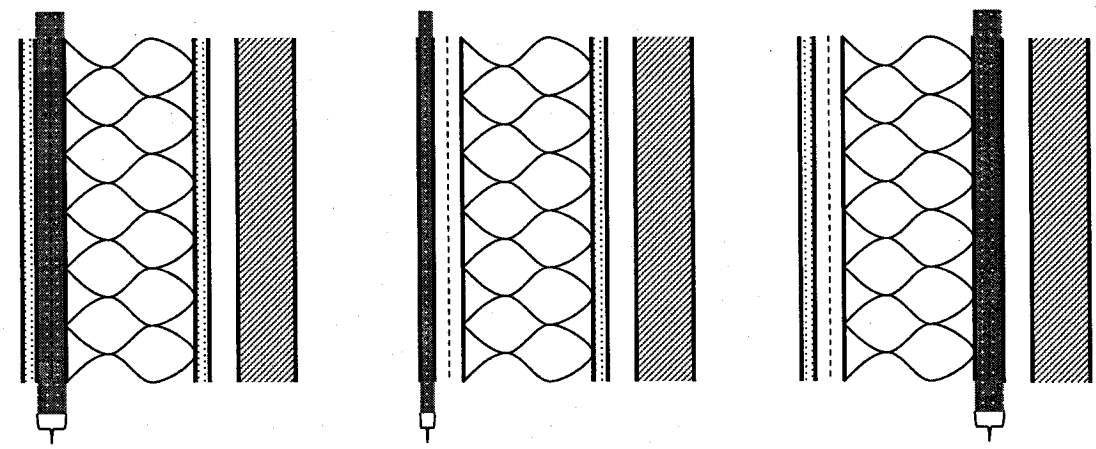

a) basic polyethylene **b) airtight drywall sheeting** **c) exterior airtight**

Figure 2.2 Air barrier approaches

Basic polyethylene stud wall In the "basic polyethylene stud wall" (Figure 2.2a), the air barrier is the polyethylene sheet placed continuously on the interior surface of the studs and taped at all edges. The polyethylene constitutes also the vapor barrier installed on the warm side. Perforated asphalt building paper or spun bonded polyolefin membrane is used as the watertight vapor permeable material layer of the rain screen.

Airtight drywall In the "airtight drywall" approach (Figure 2.2b), the interior gypsum board and gaskets at junctions constitute the air barrier. The vapor barrier role is played by vapor impervious paint or untapped polyethylene sheet. Spunbonded

polyolefin membrane or construction paper is used as the watertight layer of the rain screen.

Exterior airtight sheathing element In the "exterior airtight sheathing element" (Figure 2.2c), a sheathing membrane, for example polyolefin, is sandwiched between the two boards of exterior sheathing, for example fiberboards, to constitute the air barrier. The vapor barrier is the polyethylene sheet. Perforated asphalt building paper is used as watertight layer of the rain screen.

As cladding for all these systems, any rain screen can be used, like brick veneer, wood siding, aluminum siding, etc.

2.2 Airflow through the building envelope

Flows of heat, vapor, and air through the building envelope are driven by differences between outdoor and indoor conditions. These flows are described by mathematical equations that can be associated with the general transport phenomena equation: a flow that is proportional to a potential difference. The mathematical descriptions of air leakage are presented here with the air leakage thermal loads and moisture accumulation potential calculation methods.

The driving force for the airflow is the air pressure difference across the assembly. Airflow through cracks or other unintentional openings of building envelope is known as air leakage which includes infiltration and exfiltration movements.

2.2.1 Driving mechanisms

Pressure differences through the building envelope can result from stack effect, wind and unbalanced mechanical ventilation.

The pressure difference due to stack effect is caused by the air density difference between inside and outside air resulting from temperature difference. Assuming constant atmospheric pressure over the height of the building and no stratification within the building, the stack air pressure difference for a horizontal opening is:

$$\Delta p_a = \rho_o \cdot \left(\frac{T_o - T_i}{T_i} \right) \cdot g \cdot (H_{NPL} - H) \qquad (2.1)$$

where Δp_a is the air pressure difference due to stack effect [Pa];

ρ_o the outside air density [kg/m^3] ;

T_o and T_i , respectively the outside and inside temperature [°C];

g, gravity acceleration [9.8 m/s^2]; and

H and H_{NPL} , the height of the opening and the height of the Neutral Plane Level (NPL) [m].

The NPL height, which is at the mid-height of buildings for uniformly distributed openings, is governed by the opening distribution through the building envelope. In addition, the NPL will be obviously influenced by interior compartimentation but also by wind and mechanical ventilation effects (ASHRAE 2001).

Pressure differences due to wind depend on wind direction and speed, air density, façade orientation, and surrounding conditions. The surface pressure due to wind is given by:

$$p_w = C_p \cdot \rho_o \cdot \frac{U^2}{2} \qquad (2.2)$$

where p_w is the surface pressure [Pa];

C_p, a surface pressure coefficient [dimensionless] which is a function of location on the building envelope and wind direction;

U, the wind speed [m/s] which can be locally influenced by sheltering.

Pressure differences through the building envelope are calculated taking into account inward and leeward façade pressures, building compartimentation and openings distribution (ASHRAE 2001).

Mechanical systems affect also pressure differences through the building envelope (AHSRAE 2001). The interior static pressure should be adjusted so that airflows in and out are equal. Unbalanced systems increase infiltration or on the contrary, increase exfiltration.

The relative importance of wind and stack depends on the building height, compartimentation, location, envelope openings, terrain and shielding from the environment. The taller the building, the more the stack effect will dominate while the more exposed is the building the more the wind will play a role (ASHRAE 2001).

Pressure differences due to each of the three mechanisms can be added together. Total flow rates though openings must be calculated from the total pressure difference since flow rates are not linearly related to pressure differences (ASHRAE 2001).

2.2.2 Air leakage

Unintentional openings through the building envelope can have different geometry. Each geometry has specific flow characteristics and different geometries are present through the same building envelope.

The following power law equation is used to calculate the airflow rate of a building envelope opening or an entire building envelope that combines different kinds of opening characteristics of the whole building envelope:

$$Q = C \cdot \Delta p^n \tag{2.3}$$

where Q is the total airflow rate through the building envelope [m^3/s];

Δp, the pressure difference through the building envelope [Pa]; and

C and n, the flow coefficient [$m^3/s/Pa^n$] and the exponent [-], respectively.

The exponent is related to the geometry of the crack. Its value lays between 0.5 and 1 for mainly turbulent flows in large short openings or laminar flow for small long openings. The C and n values are obtained for a specific building envelope from the airtightness measurement; the test procedure for the measurement is explained in the next section of this literature review. The typical value of the exponent is 0.65 for a common building envelope configuration (Hutcheon and Handegord 1983).

The power law has historically been preferred to a quadratic form to describe airflow through a building envelope. Walker *et al* (1997) examines its theoretical validity and summarizes some studies which focus on the characterization of arrays of cracks. A power-law has also been defined by Sherman (1992) for laminar flow in short pipes.

2.2.3 Air infiltration models

In order to calculate air infiltration under natural conditions used for thermal load estimations and also ventilation, the results of tests at higher pressure differential are used. The procedures and calculations for the airtightness measurement of buildings are explained in the next section of this literature review. Of the different models developed,

the ones using the power law for the description of the envelope leakage lead to more realistic simulation results.

As an example, the AIM-2 model, used in building energy analysis evaluation software Hot2000 (Riley 1993), is presented here. This model computes, for a single-zone building, separately the airflow due to stack and wind effects (Walker and Wilson 1990).

The airflow rate due to stack effect is calculated with the following relationship:

$$Q_s = C \cdot f_s P_s^n \tag{2.4}$$

where Q_s is the airflow rate due to stack effect [m^3/s];

C is the power law coefficient [$m^3/s*Pa^n$];

f_s, stack flow factor related to the effect of the opening distributions [-], it is calculated using leakage coefficients for ceiling and walls;

n, the power law exponent [-]; and

P_s, stack effect reference pressure [Pa] calculated with:

$$P_s = \rho_0 g H_e \left(\frac{T_i - T_o}{T} \right) \tag{2.5}$$

where H_e is the building eaves height.

The airflow rate due to wind is computed with:

$$Q_w = C \cdot f_w P_w^n \tag{2.6}$$

where Q_s is the airflow rate due to wind [m^3/s];

C is the power law coefficient [$m^3/s*Pa^n$];

f_w, a wind factor related to the effect of the opening distributions [-], it is calculated using leakage coefficients for ceiling and walls;

n, the power law exponent; and

P_w, the façade pressure [Pa] calculated with:

$$P_w = \rho_o \frac{(S_w \cdot U_e)^2}{2} \tag{2.7}$$

where S_w is the wind shelter coefficient [-]; and

U_e, the unobstructed wind speed at eaves height [m/s].

The two flows are then superposed and added:

$$Q = \left(Q_s^{\frac{1}{n}} + Q_w^{\frac{1}{n}} + B_1 (Q_s \cdot Q_w)^{\frac{1}{2n}} \right)^n \tag{2.8}$$

where Q is the total airflow rate through the building envelope [m^3/s];

Q_s, the airflow rate due to stack effect [m^3/s];

Q_w, the airflow rate due to wind effect [m^3/s];

n, the power law exponent; and

B_1, an interaction coefficient, empirically estimated to 1/3.

2.2.4 Thermal loads due to air infiltration

Air infiltration increases thermal loads in two ways: the incoming air must be heated or cooled to the inside temperature, and the amount of energy needed is called the sensible heating, and the moisture content of the incoming air must be controlled, and this lead to latent heating (McQuiston *et al* 2000).

The energy consumption for the heating or cooling of the infiltrated air is calculated for sensible heating load:

$$q_s = \frac{Q_i}{v_o} c_p (T_i - T_o) \tag{2.9}$$

where q_s is the energy required for sensible heating [W];

Q_i is the air infiltration rate [m^3/s];

v_o, the specific volume of air [m^3/kg] ;

c_p, specific heat of air [J/kg*K]; and

T_i and T_o, respectively the inside and outside temperature.

For latent heating, the energy consumption for the heating or cooling of the infiltrated air is calculated:

$$q_l = \frac{Q_i}{v_o}(W_i - W_o)i_{fg} \tag{2.10}$$

where q_l is the energy required for latent heating [W];

Q_i is the air infiltration rate [m^3/s] ;

v_o, the specific volume of air[m^3/kg];

i_{fg}, latent heat of vaporization of water at the temperature of indoor air [J/kg vapor]; and

W_i and W_o, respectively the inside and outside humidity ratio [kg moisture/kg dry air].

2.2.5 Air leakage and vapor transport

When the air exfiltration takes place at a rapid flow rate through a large opening to the outside, the air is not cooled and condensation formation is avoided. However, when air leaks along an uninterrupted and long path from inside to outside, the air can be cooled and condensation accumulation may happen (Hutcheon and Handegord 1983, Desmarais 2002).

The potential of water accumulation can be estimated knowing the air leakage rate. A simple crude method of estimation was presented by Hutcheon and Handegord (1983). First, the mass flow rate is defined as:

$$Q_m = \frac{q}{v_o} \tag{2.11}$$

where q is the air flow rate [m^3/s]; and

v_o, the specific volume [m^3/kg].

The amount of moisture in the air can be calculated:

$$\dot{m} = Q_m \cdot m_c \tag{2.12}$$

where Q_m is the mass flow rate[kg/s]; and

m_c, the humidity content [kg moisture / kg dry air].

Because the air cannot be cooled below the outside temperature, the saturated humidity ratio the moisture leaving the wall can be calculated:

$$\dot{m} = Q_m \cdot m_{c,out} \tag{2.13}$$

where Q_m is the mass flow rate [kg/s]; and

$m_{c,out}$, the humidity content at exterior air temperature [kg moisture / kg dry air].

The maximum condensation rate can then be estimated subtracting the two moisture rates. More advanced methods include the determination of the air leakage path in the assembly (Janssens 1998).

2.3 Building envelope testing

In order to assess the performance of the building envelope in regards to energy consumption and moisture accumulation related problems, evaluation methods for research on specimens in laboratory, and for assessment of buildings in situ exist. Thermal resistance and airtightness measurement methods follow.

2.3.1 Thermal resistance measurement

2.3.1.1 In the field

Heat Flux Transducers (HFT) provide the user a mean to measure heat flux through assemblies in situ that, along with temperature across the wall, can be used to calculate thermal resistances. The HFT are positioned on uniform sections of assemblies, e.g. not over wood studs and not over air space when convection may occur. Heat Flux Transducers are thermopiles that produce electric current when there is temperature difference at either side of the HFT (Flanders 1994).

The Standard Practice ASTM C1130 (1990c) describes the calibration procedure for thin heat flux transducers; the sensitivity measurement method and the method to account for the disturbance of the heat flow by the apparatus. The Standard Practice ASTM C1046 (1995a) describes in-situ use of HTF in combination to temperature transducers. The Standard Practice ASTM C1155 (1995b) describes how to calculate thermal resistance from the in situ data acquired with HTFs.

2.3.1.2 Laboratory

Under laboratory controlled steady-state conditions, the calibrated hot box apparatus is used to measure the thermal resistance value of a tested assembly. The superseded ASTM C976 (1990a) described two different standards methods for uniform or nonuniform specimens. The resistance is calculated using the heat flow measurements from the metering chamber and temperature of the assembly surfaces and/or air temperature and surface coefficients.

The former ASTM C236 (1989) proposed a similar method using a guarded hot box. However, the specimen is surrounded by the metering box instead of insulation. The metering box walls are kept at the chamber temperature; thus, the lateral heat flow from the specimen is minimized.

These two standard methods have been withdrawn since 2005; now, ASTM C1363 (2005) proposes methods for thermal resistance measurement of envelope assemblies by means of any hot box apparatus.

2.3.2 Airtightness measurement

2.3.2.1 In the field

The fan pressurization or depressurization method, well known as the blower door test, is used to evaluate the overall air tightness of a building envelope of single zone buildings. Different standard methods describe the procedure to follow: CAN/CGSB-149.10-M86 (1986), ASTM E779 (1987), and ASTM E1827 (1996). The first one describes also the pressurization fan construction and the airflow calibration procedure of this device. ASTM E779 (1987) proposes a general method procedure while E1827 (1996) focuses on the technique using blower door fan.

The blower door method consists of the pressurization or depressurization of a building to set air pressure differentials across the entire envelope of a building. Air flow rates, which are required to maintain different magnitudes of pressure difference across the building envelope, are measured. The set of measurements are fitted with the power law equation in order to determine the overall airtightness and other leakage characteristics of the envelope.

The equipment required consists of a blower door or a fan with controllable flow, a manometer and a flow meter. For the test, the operable intentional openings (e.g. chimney trap, windows, etc.) must be closed while the partition wall openings (e.g. doors) must be opened to create a single zone. The environmental conditions for the test are a wind speed of less than 2 m/s and an inside/outside temperature difference of less than 15°C. The pressure measurements are usually done between 10 Pa and 50 Pa pressure differences through the building envelope.

A set of corrections must be made on the measurements according to the zero pressure and the density difference between the inside and outside air. The first correction consists of the scaling of each pressure difference measurement with:

$$P = P_{test} - \left(\frac{P_1 + P_2}{2} \right) \tag{2.14}$$

where P is the corrected pressure difference [Pa];

P_1 and P_2, pressure differences [Pa] before and after testing; and

P_{test} the measured pressure difference [Pa].

The air leakage rate is corrected with equations derived from the mass conservation law. The first equation is for depressurization and the second for pressurization:

$$Q_{env} = Q_{fan} \left(\frac{\rho_{in}}{\rho_{out}} \right) \tag{2.15}$$

$$Q_{env} = Q_{fan} \left(\frac{\rho_{out}}{\rho_{in}} \right) \tag{2.16}$$

where Q_{env} is the airflow rate corrected;

Q_{fan}, the airflow rate [m^3/s] measured; and

ρ_{in} and ρ_{out} are air densities respectively inside and outside [kg/m^3].

The pressure difference/airflow data are fitted with the power law (eq. 2.3). The value of the exponent is indicative of the dominant type of openings in the building envelope; exponent near to 0.5 is indicative of few large openings and near 1, of many small openings. This fitting of the power law is also used to calculate various airtightness parameters, as explained below.

Airtightness parameters

Different parameters are used for evaluation of the airtightness of the building envelope. The most used ratings are the Air Changes per Hour at 50 Pa (ACH_{50}) and the Effective Leakage Area at 4 Pa (ELA_4).

The air change per hour relates the fan flow required to maintain 50 Pa pressure difference to the volume of the building by giving the volume of air exhausted in one hour in terms of volume of building. The ACH_{50} is calculated with:

$$ACH_{50} = \frac{Q_{50}}{volume} \tag{2.17}$$

where Q_{50} is the predicted airflow rate [m^3/s] at 50 Pa of pressure difference using the fitted power law equation of the building; and

volume, the volume (m^3) of the tested building.

The effective leakage area provides the area of one large opening that would produce the same flow as measured in the whole building at the reference pressure (ASHRAE 2001). It is calculated with the following equation:

$$ELA = Q_r \frac{\sqrt{\rho/2 \cdot \Delta p_r}}{C_D} \tag{2.18}$$

where Q_r is the predicted airflow rate [m^3/s] at the reference pressure;

ρ, the air density [kg/m^3];

Δp_r, the reference pressure difference [Pa];

C_D, the discharge coefficient for a large opening, typically taken 0.6 or 1.

Sherman (1995) presents a survey of the different data calculated from the blower door test results and also their functions. Table 2.1, which is a summary of the survey, shows that blower door data are used not only to rate airtightness of building envelopes, but also to verify ventilation standards compliance, to calculate energy load and to be used in models for natural infiltration calculations.

Table 2.1 Results from the blower door test and their use (derived from Sherman 1995)

		GENERAL			STANDARD		MODEL		LOAD and COSTS	
		general	normalized	normalized Minneapolis	Ashrae 136	Ashrae 62	LBL	AIM	general	ACCA infiltration load
Air flow	CFM50	x								
	ACH50		x							
	CFM50 / square foot of floor area		x							
	CFM50 / square foot of surface area			x						
Area	Equivalent Leakage Area						x			
	Effective Leakage Area							x		
Infiltaration	CFM				x					
	ACH				x					
	CFM / person				x					
	Winter Infiltration									x
	Summer infiltration									x
Ventilation	CFM needed					x				
	LBL ELA					x				
	Heating								x	
	Cooling								x	

Airtightness Measurement Software

Automated data acquisition and calculation software for blower door exist. They are usually based on standard methods (Retrotec 1993 and Energy Conservatory 1998). Systems include a multi-purpose data logging and an automated building air tightness testing system. The software adjusts the speed of the blower door fan, monitors the building envelope/fan pressures, and processes the data. The software obtains pressure, the difference of pressure through the envelope and flow values needed for further calculations. The calculations of various airtightness ratings are automatically done by the software.

Natural Ventilation

To measure the air change rate directly, tracer gas dilution methods must be used. The standard method ASTM E 741 (1993a) describes three techniques: concentration decay, constant injection, and constant concentration.

Single assembly

A standard method is proposed to measure air leakage through installed exterior windows and doors. E783 (1993b) is a method using a sealed test chamber that allows the pressurization of the tested door or window with a fan. The result is expressed in terms of rate of air leakage per unit of length of operable crack [m^3/h-m] or area [m^3/h-m^2].

2.3.2.2 In laboratory

Single assembly

Test methods exist also for testing of windows, doors, and curtain walls in the laboratory. The assembly is installed on one face of a test chamber and, as air is supplied or exhausted from the chamber, the air flow is measured. The assembly can be tested under specified pressure conditions following the standard method ASTM E283 (1991a) or under specified pressure and temperature difference following the standard method ASTM E1424 (1991b). The result is expressed in terms of rate of air leakage per unit of length of operable crack [m^3/h-m] or area [m^3/h-m^2].

2.4 Infrared thermography

As a non-destructive testing method, infrared thermography is used both to locate and measure differences in thermal resistance level and to locate airtightness defects through the building envelope.

Recent publications (Maldague 2001 and ASNT 2003) cover infrared radiation theory, infrared thermography technology, and applications. In addition to scientific publications, infrared camera manufacturers' publications (Öhman 2001, FLIR 2003 and FLIR 2004) are useful to understand infrared camera design and performance. For up-to-date knowledge and research state on infrared thermography and related research topics, the Optical Engineering Society or SPIE and the American Society Nondestructive Testing are associations organizing conference and publishing periodicals in the area. A detailed description of the technology and the testing principles and methods is presented in the next section.

2.4.1 Infrared cameras

Infrared cameras, also known as radiometers, have four major components (ASNT 2005): an optical component that gathers the radiation from the surface; a detector that converts the radiation into a signal; an electronic component that conditions the signal; and microprocessor that processes the signal and display digital images (Figure 2.3).

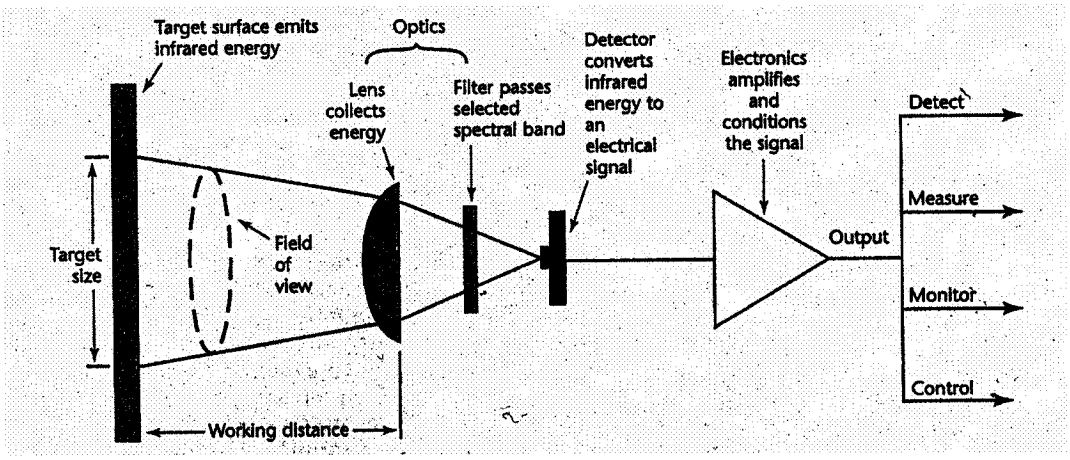

Figure 2.3 Infrared camera components (from ASNT 2005)

Detectors and systems

Detectors are the primary components of infrared camera systems. There are two families of infrared radiation detectors: thermal and photonic detectors (Maldague 2001). For thermal detectors; the radiation measurement is based on changes in material properties such as electrical conductivity, electric polarity or volume when the detectors are heated. For the photonic detectors, the radiation measurement is based on excitations generated such as electron flow or voltage, when radiation reaches the detector. The two

families of detectors have their specific characteristics; for example, the response of thermal detectors response does not depend on the wavelength while the photonic detectors response time is short because no heating is needed.

Two major systems exist to create temperature mappings from single detectors (Maldague 2001). The detectors can be arranged in arrays directly providing mappings; this system is called Focal Plane Array (Figure 2.4). Otherwise, a single detector can be associated with a scanning system. FPAs simplify the camera's design; also, without scanning system, FPAs have faster response. However, with scanning systems, an internal temperature reference located inside the camera can be seen during the scanning process and used to calibrate signal for temperature measurement while an external reference must be used with FPA systems.

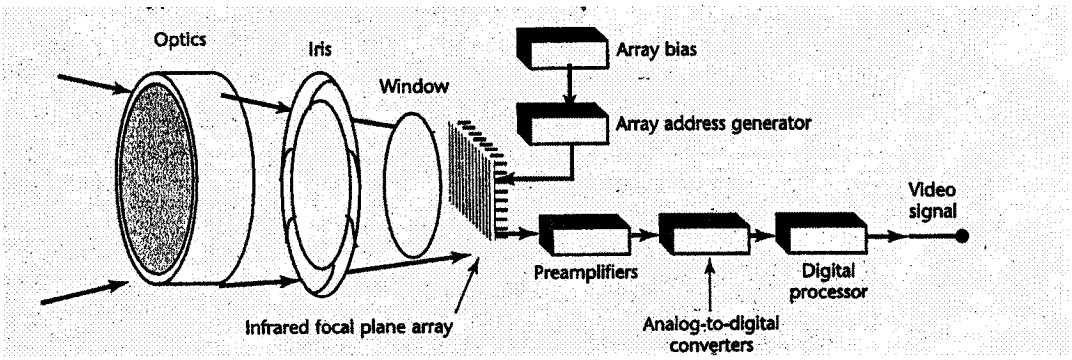

Figure 2.4. Focal plane array system components (from ASNT 2005)

Wavelength band

The infrared spectrum ranges from 1 to 100 μm. The detectors and filters set the operating spectral range of infrared cameras. Operating wavelengths are selected first to

be compatible with atmosphere infrared transmission windows: 3 to 5 μm, and 8 to 12 μm are bands inside which atmosphere transmission has the highest values (Figure 2.5).

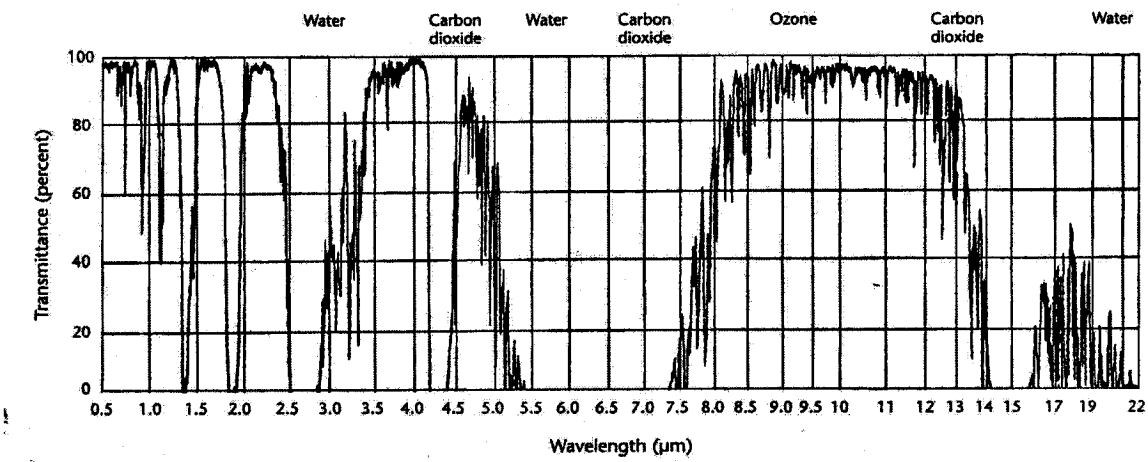

Figure 2.5 Infrared radiation atmospheric transmissions bands (from Maldague 2001)

The surface temperature dictates also the band to be used: maximum radiation peak and band change with surface temperature according to the Planck's emissivity power distribution. Finally, the emissivity of the object can change with wavelength. The range inside which the emissivity is the highest should be chosen as it is advantageous for accurate measurements (Maldague 2001).

Radiometry equation

Figure 2.6 shows a radiometric measurement configuration: the surface emits radiation, the surface also reflects radiation coming from the surroundings, the atmosphere emits also radiation, and all the radiation is transmitted through the atmosphere.

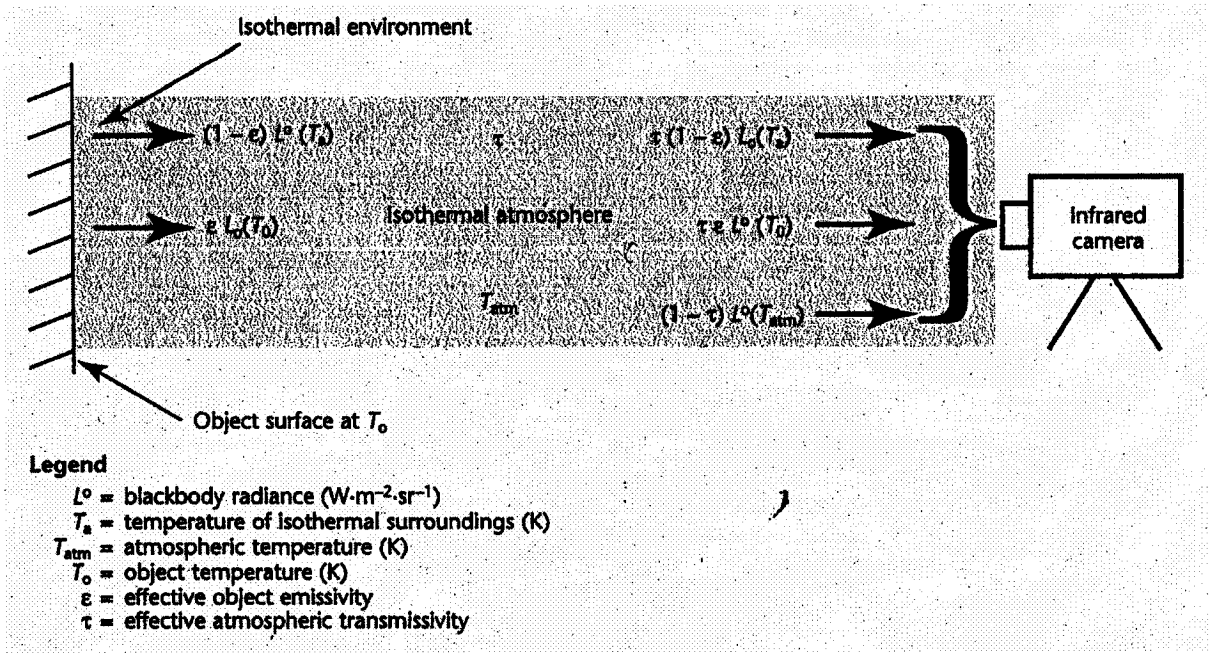

Figure 2.6 Radiometric measurement configuration and radiation sources (from ASNT 2005)

What infrared cameras measure is the effective radiation intensity inside a detection small solid angle, from a small surface area, and also for sometimes a large detection spectral band or radiance (ASNT 2005).

The spectral radiance of a blackbody can be defined as:

$$L_{\lambda,b} = \frac{E_{b,\lambda}}{\pi} \tag{2.19}$$

where $L_{\lambda,b}$ is the spectral radiance[$W/(m^2 \cdot sr)$];

E_λ, the Planck's emissivity power distribution for a blackbody [$W/(m^2 \cdot \mu m)$].

Integrating over the spectral range of the detector to be used, the effective radiance [$W/(m^2 \cdot sr)$] can be calculated.

Also, the spectral radiance of a surface can be calculated from the equivalent blackbody spectral radiance with:

$$L_{\lambda,s} = \varepsilon_\lambda L_{\lambda,b}(T_s) \tag{2.20}$$

where $L_{\lambda,s}$ is surface spectral radiance [W/(m^2·sr·μm)];

$L_{\lambda,b}$, the spectral radiance of a blackbody [W/(m^2·sr·μm)];

ε_λ , the spectral emissivity of a surface; and

T_s, the surface temperature [K].

The fundamental equation of radiometry gives the total radiation intensity that reaches the detector as (ASNT 2005):

$$L = \tau\varepsilon L_b(T_s) + \tau(1-\varepsilon)L_b(T_r) + (1-\tau)L_b(T_{atm}) \tag{2.21}$$

where L is the total radiance reaching the detector [W/(m^2·sr)];

the L_b is the effective radiance of a blackbody [W/(m^2·sr)];

ε, the emissivity of the surface;

τ the transmissivity of the atmosphere; and

T_s, T_r, and T_{atm}, respectively the surface, ambient surface and atmosphere temperature [K].

The fundamental equation of radiometry is based on the assumptions that the atmosphere is homogeneous and isothermal; and that the environment is isothermal. The emissivity of the surface is the average emissivity over the temperature range of the surface that is considered to be grey. The transmissivity is the average transmissivity of the atmosphere under the experimental conditions.

Temperature Calibration

The radiance measured by the camera is actually also a function of the sensitivity of the camera system (ASNT 2005). The effective radiance is:

$$L_{eff} = \int_{\Delta\lambda} S(\lambda) L_{\lambda} d\lambda \tag{2.22}$$

where L_{eff} is the effective radiance [W/(m^2·sr)];

L_{λ}, the surface spectral radiance [W/(m^2·sr·μm)];

S(λ), the sensitivity function for the spectral band used.

However, it should be noted that the sensitivity of an infrared camera system cannot be easily determined, and that the sensibility changes with time.

A calibration procedure must therefore be carried out in the laboratory to determine the sensitivity. A blackbody measured at short distance is used to find the correlation between the radiance and the surface temperature. In practice, the correlation is found between system output units (volt for example), instead of effective radiance [W/(m^2·sr)], and surface temperature [K].

The calibration curve has a form analog to the Planck's law equation:

$$I = \frac{A}{Ce^{B/T} - 1} \tag{2.23}$$

where I is the camera response [camera output units]; and

A, B, and C are calibration constants.

Effectively, assuming linear response of the detector to the total radiance; the response of detectors would be proportional to the Planck's law equation (ASNT 2005).

Processors

Camera processors include calculation tools so that the surface temperature is automatically calculated taking into account the radiometry equation (eq 2.21) and the calibration equation (eq. 2.23) presented before. Analysis tools are also included for

temperature measurement analysis such as isotherms, and areas, lines and spots. Isotherms highlight the area of same temperature for comparison of same temperature area; various temperature statistics such as mean, maximum, minimum temperatures and histograms can be computed for inside defined areas; and temperature profiles can be plotted.

Also, it is the processor that produces temperature distribution images, or the thermogram. The thermogram is a digital image (Maldague 2001) that is a matrix of elements, generally of 8 or 16 bits each, stored where rows and columns give element location. The level and range settings allow using a section of the camera temperature range (Maldague 2001) for more precise temperature scale. Figure 2.7 shows the relation between the level and range used and the camera calibration curve.

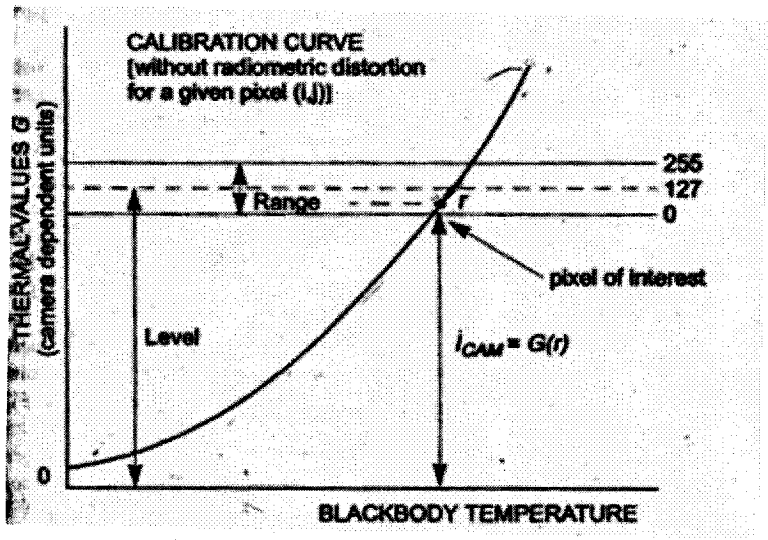

Figure 2.7 Calibration curve and level and range settings for an 8-bit stored system (from ASNT 2005)

The primary representation of the matrix from these data is in grey scale; however, other color palettes can be used.

2.4.2 Infrared cameras performance

Infrared cameras are used both to obtain a qualitative temperature pattern and to quantitatively measure surface temperature at specific locations. The performance of an infrared system depends therefore both on thermal sensitivity and spatial resolution.

Noise Equivalent Temperature Difference

The Noise Equivalent Temperature Difference (NETD) specifies the thermal sensitivity of the system. The NETD is the root mean square of the random noise signal converted to a temperature difference. The NETD cannot be easily calculated from the characteristics of an infrared camera system; therefore, the NEDT measurement is usually done in the laboratory.

The random noise signal is measured, the root mean square is calculated, and the calibration curve of the camera is used to convert signal into temperature (Öhman 2001) (Figure 2.8).

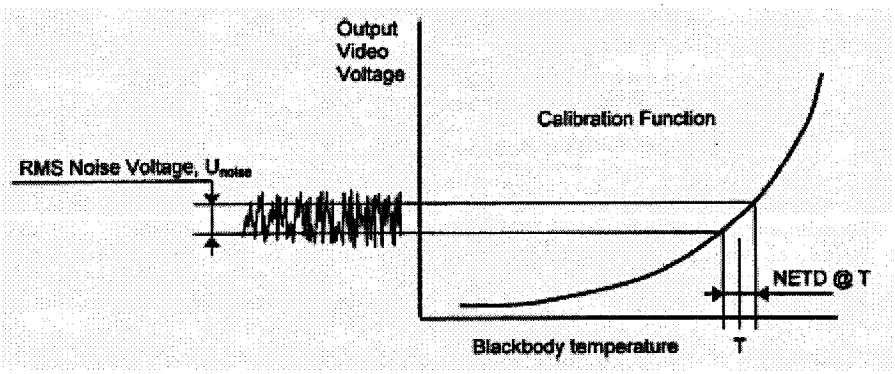

Figure 2.8 NETD and calibration curve (from Öhman 2001)

The NETD varies with the temperature measured because of the nonlinearity of the calibration function with temperature. The NEDT is usually specified in terms of the temperature difference at 30°C.

Slit Response Function

There are different ways to describe spatial resolution. The spatial resolution is given in element per line based on either the Instantaneous Field of View (FOV) or the Slit Response Function (SRF).

The IFOV is the angle subtended, in terms of the angular width in milliradian, by a detector in the case of an ideal optical system. As a number of elements per line the resolution is the number of IFOV contained within the length of the FOV (Öhman 2001).

The SRF is based on the practical performance of an optical and electrical system. The SRF cannot be easily calculated from the characteristics of an infrared camera system. Therefore, the SRF is measured using the set up showed in Figure 2.9. A slit of higher temperature than the background is visualized several times with the infrared camera decreasing its width.

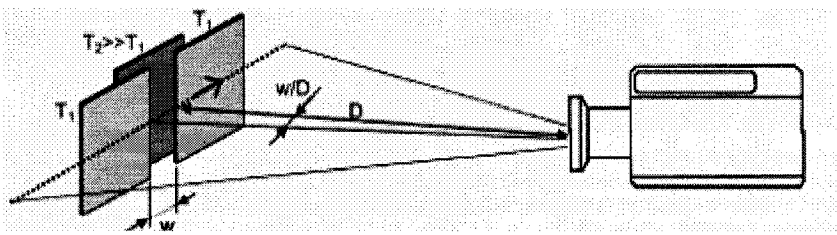

Figure 2.9 SRF measurement method (from Öhman 2001)

The signal profile perpendicular to the slit is measured (Figure 2.10). When the width is large enough, the signal is constant; it is the modulation equivalent to 1. The signal values for thinner widths are recorded and plotted (Figure 2.11).

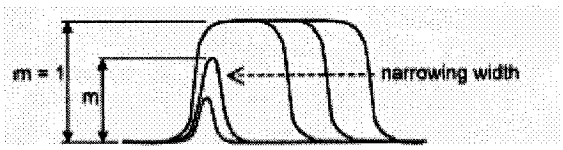

Figure 2.10 Signal responses recorded for SRF measurement (from Öhman 2001)

The first part of the curve for both systems, as shown in Figure 2.11, follows the ideal expected signal values and is related to the slit to IFOV ratio. Effectively, an ideal camera system would measure the average radiance of the object, i.e. a radiance proportional average of the crack and the panel area in the instantaneous field of view area. The difference between the signal and the idealized signal in the last section of the curve is due the optical and electronic systems effects.

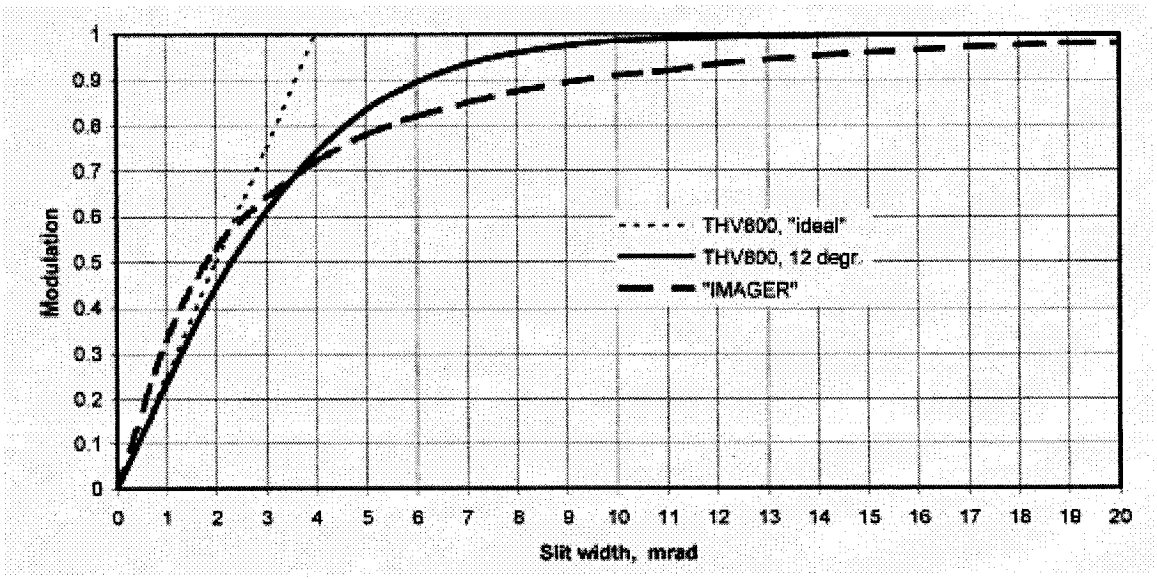

Figure 2.11 SRF of different infrared cameras (from Öhman 2001)

The SRF is the angular width [milliradian] required to read 90 % of the modulation. As a number of elements per line, the resolution is the number of SRF contained within the length of the FOV (Öhman 2001).

Minimum Resolvable Temperature Difference

The Minimum Resolvable Temperature Difference (MRTD) is related to both thermal sensitivity and spatial resolution. The MRTD describes the imaging performance of the camera. The MRTD measurement is subjective as the result can change with the operator.

In contrast to SRF measurement, the MRTD measurement (Öhman 2001) is done with low temperature difference between the target and the background. A four bar pattern at varying temperature is visualized with the infrared camera (Figure 2.12).

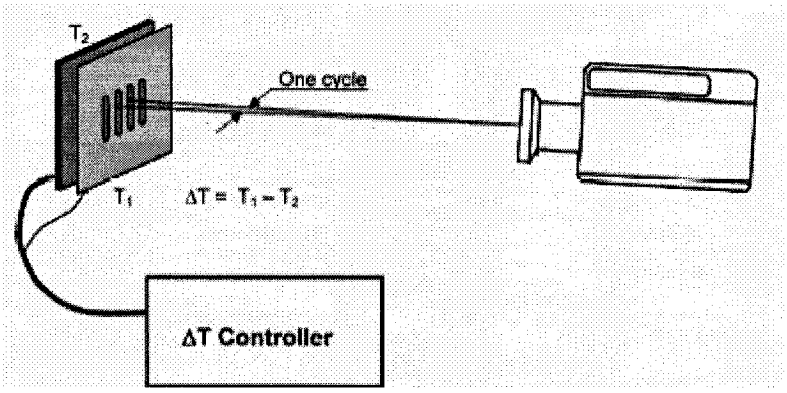

Figure 2.12 MRTD measurement method (from Öhman 2001)

The operator adjusts the temperature difference to the value for which the image of the four bars just disappears on the camera display. Thermal pattern spatial frequency, calculated in cycle per milliradian, can be changed for different MRTD calculation.

2.4.3 Infrared thermography techniques

Infrared thermography is used to visualize and measure temperature distribution. The temperature distribution can then be used to investigate the surface or the material under the surface. There are two major infrared thermography techniques (Maldague 2001).

Passive thermography

In passive thermography, the surface temperature distribution visualized is under typical conditions. Passive thermography is often qualitative; abnormal temperature distributions, or temperature differences, are indications of abnormal situations. Passive thermography can also be quantitative. In this case, heat transfer modeling is used to relate temperature distribution to specific discontinuities or thermal events.

Active thermography

In active thermography, heating of the specimen using different methods is required to obtain surface temperature distributions under atypical conditions. Using *pulse thermography,* the specimen is heated for a short period of time and the temperature distribution decay is studied as the presence of surface defects modifies the surface temperature decay. Using *step heating,* the surface is heated for specific time

duration and the temperature distribution rise is studied. Different coating material and thickness influences the temperature distribution increase. Using *locking thermography*, thermal waves are generated in the specimen by periodical heating, and the oscillating temperature distribution is studied: the specimen internal characteristics change the thermal distribution waves. Quantitative active thermography uses the inverse problem technique. From temporal temperature distributions analysis, the specimen characteristics are evaluated using heat transfer modeling using reversible operator optimization techniques.

Now that the thermography equipment and techniques have been presented, the use of infrared thermography for assessing the building envelope follows.

2.5 Infrared thermography applications

The first attempts using infrared thermography for building were done in the sixties with the first infrared imaging system. Real progress has been accomplished by private companies, research institutes and universities in the seventies and eighties in United States, Canada and Sweden. The research aim was to use infrared thermography in the evaluation of building envelope performance. Theoretical and practical knowledge had thus been accumulated driving to the development of standard infrared investigation methods. At that time, infrared equipment has been adapted to the building envelope evaluation (Maldague 2001).

Works towards the use of infrared thermography for building envelope evaluation have been published widely in papers. Now, books give overviews of the knowledge accumulated. From this literature, principles of thermography for building envelope

evaluation are first presented. Then, standard methods developed for qualitative interpretation and quantitative measurement are described.

2.5.1 Infrared thermography for in-situ building survey

Infrared thermography is mainly used to evaluate the heat control and air barrier aspects of the performance of the building envelope.

2.5.1.1 Principles

The assessment of insulation level variations is based on the observation of the distribution of wall surface temperatures due to thermal resistance variations: effectively, the surface temperature depends on the thermal resistance of the wall. Figure 2.13 shows thermograms of a wall: the bottom section is less insulated than the rest of the wall and the wood stud sections of the wall, that are thermal bridges, are also apparent.

However, the surface temperature depends also on difference of temperature between either sides of the assembly. Thus, temperature difference between inside and outside is one factor influencing thermal resistance levels evaluation: higher temperature difference accentuates surface temperature variations due insulation level (Pettersson 1980).

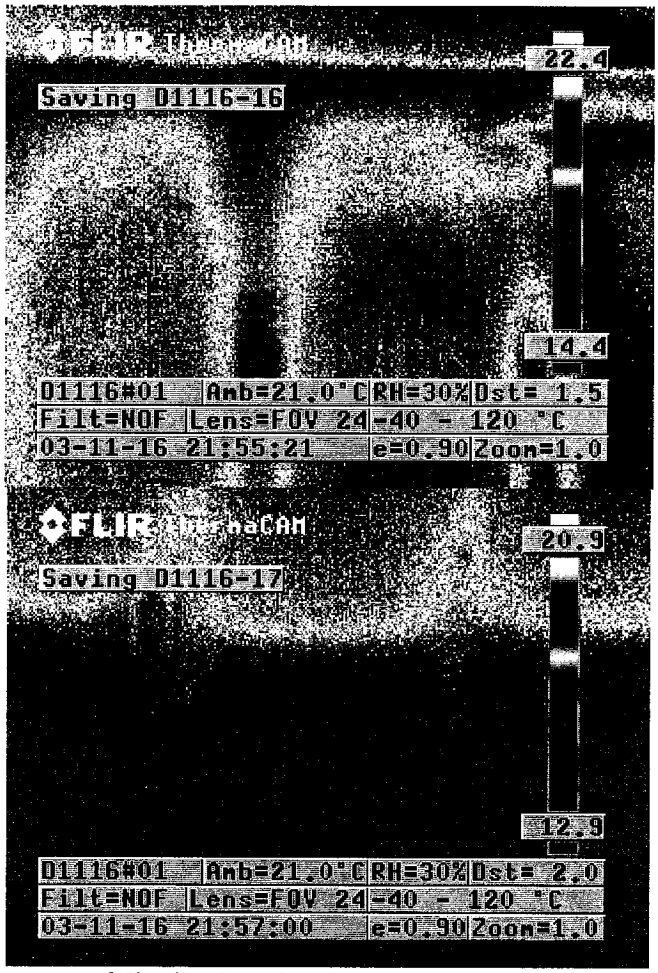

Figure 2.13 Thermogram of distribution of surface temperature showing variation of thermal resistance in the wall

Non-stationary temperature conditions can also influence surface temperature. Inside or outside temperature variations creates temperature oscillation that will be propagated differently through the assembly according to the thermal diffusivity. Infrared thermography insulation level inspection cannot therefore be performed efficiently under variations of temperature (Pettersson 1980). For example, sun radiation on a brick clad wall will result in nonuniform temperature conditions that vary with the duration and the magnitude of the irradiation. Also, solar radiation coming through a window on an inside surface will result in the equalization of the surface temperatures.

In addition, the value of the thermal resistance of the boundary layer at the surface of the assembly has an influence on the surface temperature. The value of surface resistance is composed of convective and radiative heat transfer; the parameters influencing their values will influence the surface temperature. Sources of interference influencing the value of the surface resistance are: radiation sources toward or near the surface and air currents directly toward the surface. Commonly, the changes in temperature due the variation in the value of the boundary layer thermal resistance are gradual and symmetrically distributed over the surface located at the junctions of surfaces. Figure 2.14 shows, at the junction of an inside wall, the influence of the inside surface coefficient on the surface temperature. In comparison, thermal bridges can be observed at junction between partition walls and roof.

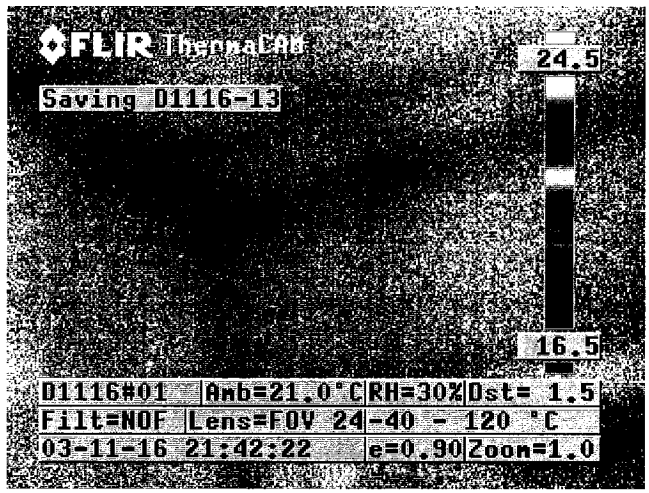

a)

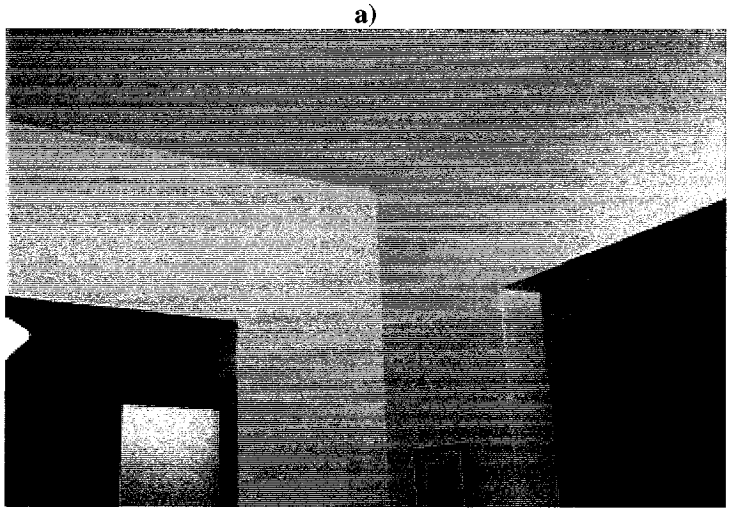

b)

Figure 2.14 Thermogram showing the distribution of surface temperature (a) due to surface coefficient and (b) thermal bridges at the junction of partition walls and roof

The localization of air leaks by infrared thermography is done through the observation of the surface temperature distributions of assemblies. In effect, cold air infiltrating across an assembly changes the temperature of the surfaces adjacent to the openings on the warm side of the assembly. Figure 2.15 shows the effect of depressurization on an air leak at exterior wall and floor junction, as seen from inside the room.

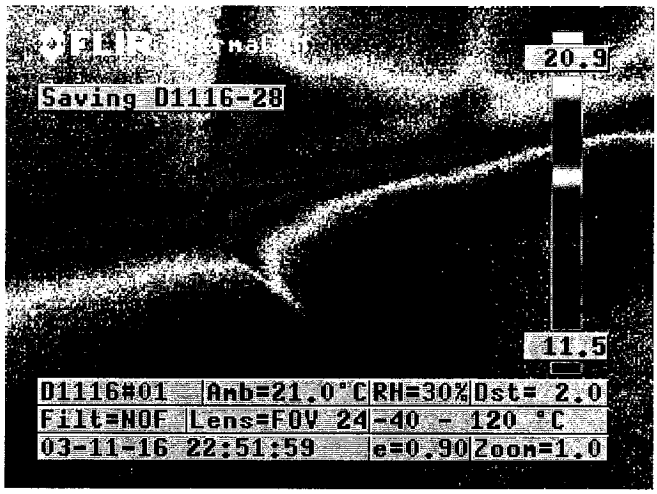

a)

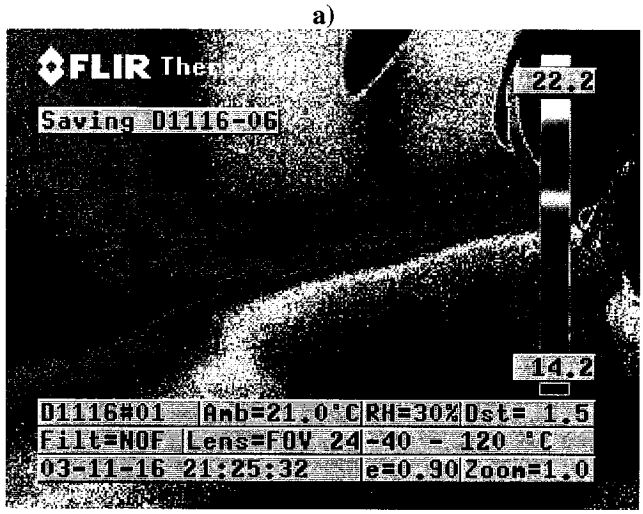

b)

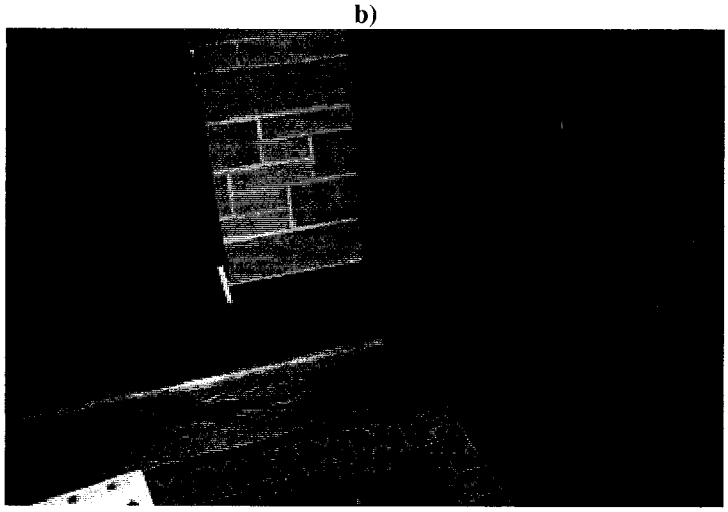

c)

Figure 2.15 Thermogram of surface temperature variation due to an air leak before (a) and after depressurization (b) of the building envelope at exterior wall and floor junction (c)

The magnitude of the air movement depends on both the nature of the openings and the pressure differential across the assembly (Pettersson 1980). The air movement is commonly provoked by depressurizing the building mechanically to overcome natural pressure differential due to wind conditions, stack effects, and mechanical ventilation system. The temperature of the surface around the openings will be then be changed clearly.

The presence of water and moisture in the materials change the thermal properties of the assembly; therefore, indirectly, moisture can also be detected with thermography. This type of inspection is performed after an abrupt temperature drop: in this situation, humid areas surface temperature change more slowly that the rest of the assembly due to the latent heat of water.

2.5.1.2 Standard Methods

Official publications, describing an infrared thermography procedure for detection of insulation and airtightness defects, are not so numerous but come from reputable sources.

ASHRAE published in 1981 a standard that could be considered as an overview of methods with broad explanations about conditions and equipments:

Standard 101-1981 "Application of Infrared Sensing Devices to the Assessment of Building Heat Loss Characteristics"

Compared to standards usually stated as reference procedures, the ASHRAE standard is nonspecific about equipment, conditions and for purposes.

The International Standard Organization has published:

ISO 6781 "Thermal insulation- Qualitative detection of thermal irregularities in building envelopes- Infrared method"

This standard proposes a complete infrared practice for building envelope inspection of thermal, moisture and air leakage defects. Reference thermograms are annexed. A brief presentation of basic knowledge necessary to understand the equipment and method requirements is attached.

The ASTM has published, in its construction sections, the following standards:

C1060 "Standard Practice for Thermographic Inspection Installations in Envelope Cavities of Frame Buildings"

C1153 "Standard Practice for Location of Wet Insulation in Roofing Systems Using Infrared Imaging"

The first one is specifically about thermal and moisture defects in lightweight frame construction. The second one is the only standard procedure to locate moisture that can be used for every roof types. In the Evaluation section, a part of an infrared technique is presented in:

E1186 "Standard Practices for Air Leakage Site Detection in Building Envelopes and Air Retarder Systems"

This constitutes complement of the ASTM C1060 to evaluate the whole building envelope.

Three standards have been written as for supplementary measurements related to infrared survey:

E 1933 "Standard Test Methods for Measuring and Compensating for Emissivity Using Infrared Imaging Radiometers"

E 1862 "Standard Test Methods for Measuring and Compensating for Reflected Temperature Using Infrared Imaging Radiometers"

E 1897 "Standard Test Methods for Measuring and Compensating for Transmittance of an Attenuating Medium Using Infrared Imaging Radiometers"

Those standards can be considered as supplements to be used to improve the results of the inspection. They constitute three independent methods to measure one of the parameters used by the camera when it is imaging the wall temperature gradient. These parameters are usually estimated from literature or with ancillary equipment. Such parameters allow achieving some quantitative on-field measurements but are beyond the scope of the standards C 1060, E 1186.

Another standard has also been published specifically for equipment specifications:

E 1311 "Standard Test Method for Minimum Detectable Temperature Difference for Thermal Imaging Systems"

From Canada, there is a CGSB standard:

149-GP-2MP Manuel d'analyse thermographique des enveloppes de bâtiment

This document is proposed also as reference for teaching this complex method. General building science knowledge is briefly explained and a report presentation annexed.

Contents Analysis

Standards present a whole and/or specific procedure; they may or not contain methods, conditions and equipment principles explanations. An analysis between

standards and a synthesis on standard methods follows, comparing date of publication and specific scopes in terms of building types, anomaly types. The distinction between building construction types can be done regarding the weight of building construction or different components of the building. The building characteristics have a significant impact on the favorable conditions and methods for thermography of building survey.

The ASHRAE-101 was published in 1981 and has not been reviewed since that time. Actually, the ASHRAE committee had decided to let ASTM continue in the development in this field. The first edition of the ISO 6781 was published in 1983.The CGSB (F) 149-GP-2MP standard followed a large Canadian research project about infrared thermography for building survey in the '80. It has been published in 1986. There are four standard practices from ASTM. Chronologically, the first one published was C1060 in 1990; it is about inspection of insulation installation. In the same year, the C 1155 for determining the thermal resistance has complemented the later one. Then in 1997, the C 1060 has been reapproved and the C 1153 published and it deals about locating wet insulation in roofing systems. The last one, E 1186, was approved in 1998 for the detection of air leakage sites.

The ISO 6781 and CGSB 149-GP-2MP standards are presented in a general way without any distinction about the type of building construction. The ASHRAE-101 is actually clearer about construction type. Precise information about conditions is presented in tables for the different categories from light to heavyweight construction. Also for wall or roof, different methods are proposed. The ASTM standards are the only ones giving precision in their scope about the kind of building construction for which they were written specifically for. The ASTM C 1060 for insulation is in particular

written for light frame buildings. Even though it is not clearly stated in the scope the calculation of the thermal resistance with the C 1155 method, it seems also to be only intended for lightweight construction type. The C 1153 for wet insulation can is used only for roof survey from the exterior while the air leakage site detection according to E 1186 can be done for any kind of building construction. Table 2.2 presents a summary of the standards scope study in terms of construction type.

Table 2.2 Comparison of the scope of standard methods for the envelope thermography survey

	Lightweight	Heavyweight	Unspecified	Wall	Roof	Unspecified
ASHRAE 101	x	x		x	x	
ISO 6781			x			x
CGSB 149			x			x
ASTM C 1060	x			x		
ASTM C 1155	x					x
ASTM E 1186	x	x		x	x	
ASTM E 1153			x		x	

Infrared thermography for building survey is mostly used in building envelope thermal losses assessment. That is why ASHRAE-101, ISO-6781 and CGSB149-GP-2MP have been written. The air leakage and moisture method seem to be presented in a complementary way. The ASTM standards have actually been written separately regarding those three different kinds of defaults: C1060 for thermal defect, E 1186 for airtightness default but the last one, ASTM C 1153, for moisture location cannot be considered as a general reference for moisture defects. C 1153 is written for a specific type of wetting defect appearing only in roofs. Thus, moisture detection method is only presented in ASTM in a complementary way like for the other standards. Table 2.3 presents a summary of the standards defect types study.

Table 2.3 Comparison of the scope of standard methods for building envelope thermography survey in terms of defect types

	Defect type			
	insulation	airtightness	moisture	water
ASHRAE 101	x	c	c	x
ISO 6781	x	x	c	
CGSB 149-GP-2MP	x	c	c	
ASTM C 1060	x			
ASTM C 1155	x			
ASTM E 1186		x		
ASTM E 1153				x

c = considered as complement

Actually, for a whole procedure for different types and parts of construction and looking for every kind of defects, the ASTM standards should be used together. The C 1060 and the E 1186 present the methods for thermal and moisture defect investigation and for air leakage site detection in the envelope. For wet roof investigation, which complements the general envelope survey, the C 1153 has to be used. The ASTM standards were written mainly for lightweight construction. The ISO and CGSB standards can be consulted when another type of construction occurs as their scopes do not state specifications about the type of construction. However, for precise values, the ASHRAE standard constitutes a trustable source of reference. This standard, which has been written first, gives specifics values regarding the conditions of survey for each type of construction.

Standards ASHRAE 101, ISO 6781, CGSB 149-GP-2MP, ASTM C1060 and ASTM E 1186 can be compared for the entire wood-frame survey. Each of the phases of a whole thermography procedure is compared in Table 2.4. The ASTM standards are used as basic references being the last ones published.

Table 2.4 Comparison of contents of building envelope thermography survey standard methods for a wood-frame construction

ASHRAE 101	ISO 6781	CGSB 149	ASTM C1060	ASTM E1186	Procedure for thermographic survey of building enclosure
					Previous on field/laboratory preparation
	x				*reference thermogram production*
x			x		*equipemtn testing*
x		x	x	x	Choice of thermography type
			x		1. Previous analysis
		x			*analysis of the request*
		x			*review of contract documents*
		x			*study of theexecution drawings*
					2. Infrared Equipement Specifications
	x	x	x	x	*spatial resolution*
x	x	x	x	x	*thermal resolution*
x		x			*setting and recording possibilities*
					3. Survey conditions
x	x	x	x	x	*climatic conditions*
	x			x	*depressurization conditions*
x	x	x	x	x	*other condtions*
					4. Thermography
x	x	x	x		*general survey*
		x			*detailed survey*
x					*quantitative measurment*
					5. Interpretation of the data
	x	x	x	x	*qualitative interpretation*
x					*caculations*
x	x	x	x		6.Report
					7. Interpretation of the problem
		x			compilation of the findings
		x			synthesis
					8. Solutions proposition
		x			*provide alternative solution*
		x			*plan retrofit*

The supplementary standards do not present infrared procedures for survey. They can be separated in two subjects: equipment specifications and complementary methods to increase the accuracy of temperature reading. Most of the equipment requirements are

inherent to the capacity of the infrared camera; the specifications of the manufacturer can thus be looked at. The MRTD is the only performance criterion specific for building survey that has to be previously tested. The MRTD indicates the ability of the operator to discern the temperature difference with the system tested (Section 2.4.2 Infrared cameras performance). The notion of MRTD was stated and described in the first ASHRAE-101. Since then, every standard written refers to this concept to rate the equipment. In the ASTM C1060, a brief method is suggested, but for the particular scope of this standard. In 1997, ASTM E 1213 standard has been written evaluating the capacity of any equipment. The complementary methods written by ASTM are about reflected temperature, surface emissivity and transmittance of a medium. E 1862, E 1933 and E 1897 present the way to calculate the value of each parameter and to compensate it with the infrared equipment. Those standards can be used for any kind of building thermography increasing the accuracy of the temperature data measured.

2.5.1.3 Quantitative measurement

For thermal resistance measurement, infrared thermography is used to find appropriate locations for heat flux transducer following ASTM C1046 (1995a).

Also, surface temperatures can be measured by infrared thermography for the method proposed by the Standard Practice ASTM C1046 (1995a). With lightweight material components a stationary heat flow can be established and the temperature used directly. In heavyweight construction, steady-state thermal conditions rarely occur. The effect of diurnal variation and heating cycles combine to have a continually changing thermal environment and a high thermal mass not in step with the temperature differences

in the building (Hart 1991). Under these conditions, the temperature measured taken at one instant in time is misleading. The thermal resistance value can after be derived from the average heat flux divided by the average inside/outside temperature difference in a cumulative process.

Infrared thermography is used also as a complement tool to measure thermal resistance values of envelope components. The conditions required for quantitative evaluation are more severe. Usually, thermograms are recorded for subsequent laboratory processing and analysis (Hart 1991). Surface temperature is used assessing resistance value. Wall resistance can also be calculated with surface temperature, and outside and inside air temperature with:

$$R_{wall} = \frac{(T_o - T_i)}{h_i(T_{s,i} - T_i)} \tag{2.24}$$

where R_{wall} is the wall resistance [$(m^2 \cdot K)/W$]

T_i, the inside air temperature [°C];

T_o, the outside air temperature [°C];

$T_{s,i}$, the inside surface temperature [°C];

h_i, the inside surface coefficient [$W/(m^2 \cdot K)$].

Standard method ASHRAE 101 proposes to determine if an assembly is insulated or not and to estimate the thermal resistance using a method based on temperature indexes. Temperature indexes are the fraction of the air-to-air temperature difference which occurs across the building component and the outside surface film. Temperature indexes are calculated with:

$$TI = \frac{T_{s,in} - T_{in}}{T_{in} - T_{out}} \tag{2.25}$$

where TI is the temperature index [-].

A well insulated wall will have a TI greater than 0.95 while an uninsulated wall will have a TI of 0.85 or lower. TI graphs exist to estimate the thermal resistance of the wall using TI values.

2.5.2 Infrared thermography for laboratory studies

Research requires the most precise and accurate results possible under specific controlled conditions. Infrared thermography laboratory methods must be, thus, more detailed. Also, specimens and set up vary with research purpose and facilities. At this time, there is no one standard method describing the use of infrared thermography for absolute temperature measurement in laboratory in the context of building envelope studies.

The complementary standard methods presented above can constitute parts of an entire laboratory procedure. Then, the best sources of method descriptions and explanations are laboratories procedures developed in the context of similar research. Türler *et al* (1997) gives a detailed method using a reference emitter to improve temperature measurement accuracy. The method has been developed in the context of research studies on heat transfer model validation.

2.5.2.1 Standards

Three standards propose method that can be used for laboratory measurements. These standards describe methods to measure specific characteristics and to compensate for it with an infrared imager.

E1833 "Standard Test Methods for Measuring and Compensating for Emissivity Using Infrared Imaging Radiometers"

Emissivity of the surface material must be measured for experimental conditions to get emittance value of the material under those conditions and the infrared imager used. Therefore, the literature values of emissivity are rarely used.

Two methods are proposed in the ASTM E1933 (1999). A simple method, the noncontact thermometer method, is based on imager compensation instead of calculation. The surface to be tested must be brought to a temperature 10 to 20°C colder or warmer than the background temperature. A surface-modifying material of emissivity near to 1 is applied to the surface tested. A thermogram is taken of the surface. The temperature is red over the modifying material and recorded. The emissivity is adjusted using the integrated software, to read the plain surface the temperature previously recorded over the modified surface. The emissivity corresponding to the right temperature is the one of the surface material in those conditions and for this specific equipment.

E1862 "Standard Test Method for Measuring and Compensating for Reflected Temperature Using Infrared Imaging Radiometers.

The standard method E1862 (1997) proposes a direct and a reflector method for measurement of the equivalent background temperature. The direct method consists of taking a thermogram in the angle of incidence of the specimen and averaging the temperature over the field of view.

The reflective method uses a highly reflective mirror to measure an equivalent background temperature. A thermogram is taken of this mirror installed on the object position. The temperature is averaged over the mirror infrared image to get the equivalent background temperature to be used for corrections in the software. Comparing to the direct method the thermograph and the imager are taken into account with the use of a background mirror.

E1897 "Standard Test Methods for Measuring and Compensating for Transmittance of an Attenuating Medium Using Infrared Imaging Radiometers"

The standard method E1897 (1997b) proposes a method to measure transmissivity of a medium using a built-in computer into the camera. The standard proposes also two methods for compensating for the transmissivity of an attenuating medium using the built-in computer when the emissivity of the specimen and the transmittance of the medium are known and when the emissivity of the surface and the transmittance of the medium are unknown but the specimen temperature is known.

2.5.2.2 Thermography chamber

A thermography chamber has been designed by the Lawrence Berkeley National Laboratory where studies of heat transfer through glazing elements are undertaken. A

detailed description of the chamber is given by Türler *et al* (1997). Being a modified climate chamber, the thermography chamber allows, under uniform thermal radiation conditions, the control and measurement of air temperature and velocity on one face of a specimen while also enabling an infrared camera to measure with an unobstructed view the specimen. Testing have been done also on insulated glazing by Elmahdy (1996) using a guarded hot box set-up. Ge *et al* (2001) undertook testing on curtain walls in an environmental chamber.

2.5.2.3 Reference emitter technique

The use of a reference emitter improves the accuracy of absolute temperature measurements. A reference emitter is a temperature-controlled device with a known surface emittance. Some reference emitters are available commercially such as blackbody used for calibration but custom-made references are also used. A reference emitter is constituted of a temperature controlled liquid system, a highly conductive plate and a finish of the same material as the object (Türler *et al* 1997). The reference emitter must stay in the field of view of each thermogram while the focus is made on the specimen. The difference is used to correct the rest of the infrared data of the thermogram. Linear correction can be done on a temperature measurement when the difference between the reference emitter surface temperature and the surface temperature is small. A specific error analysis must be done to calculate the error on referenced temperature measurement.

2.5.3 Research studies

2.5.3.1 Building envelope research studies

Infrared thermography is used at the research level for more than ten years in the building envelope field. This is an indirect result of developments of equipments and methods but also to the needs of valuable information related to heat transfer through the building envelope. Research projects using this technology have been undertaken mainly about the validation of complex heat transfer modeling.

Simplifications are common for studying the heat transfer through building envelope; a common simplification is to assume one-dimensional heat flow. Also, conventional apparatus and techniques quantify the performance of an assembly as a homogeneous material, without allowing the relative comparison of subcomponents. Infrared thermography, which gives a mapping of the surface temperatures, presents information about spatial and non homogeneous material heat transfer effects. Therefore, this technology is being used for complex heat transfer studies to give basic understanding of complex heat flow phenomena, to validate thermal analysis models, and to develop new energy-efficient products.

A collaborative window study project led to an overview of the complexity and the possibilities of the infrared thermography used for complex heat transfer analysis. Glazing units having different characteristics have been modeled with two-dimensional model and thermograms have been taken in laboratory. Instead of common global performance evaluation of windows, local performance comparisons have been done.

As presented in an overview paper (Arasteh *et al* 1992), a primary challenge was for both groups to create a procedure to acquire quantitative measurements of building

envelope assembly surface temperature using infrared thermography in laboratory. The infrared measurements from two different laboratories could be compared providing the opportunity for discussion about the methods. The temperature accuracy on infrared measurement was evaluated to 0.5°C for thermographic measurements.

The major objective of the project was the comparison of two-dimensional heat transfer simulations with experimental measurements for purpose of validation. The results showed good agreement between modeled and measured surfaces temperature distributions. Each measurement/calculation location surface temperature values fell in a range of 1°C.

The differences in the results were attributed to a few factors. In modeling, the surface coefficient was considered constant, while in reality it varies. Also, different methods were used to measure the surface coefficient. Nevertheless, the difference in temperature due to the variations of surface coefficient values was evaluated as being of the same order of magnitude as the uncertainty and thus insignificant. The spatial uncertainty coming from thermographic measurements is also seen as a significant factor. The laboratories used different methods to locate measurements. Regarding local parameters, this issue is of great interest.

This research demonstrated possibilities of using infrared thermography as a tool for heat transfer study. This research pointed out issues of accuracy and uncertainty using of infrared camera to validate heat transfer models. Such issues are also relevant for other types of studies.

2.5.3.2 Indoor environment quality

Studies have been done in the field of indoor environment quality, specifically, looking at air flow. The study of indoor comfort requires among others the measurement of air temperature and velocity through the room; therefore, the use of infrared thermography for visualization and measurement of room air temperature as well as air flow temperature distributions has been studied for more than ten years. Commonly, either many measuring devices or the translation of a single device was used to measure temperature across the area of interest.

Early studies by Hassani (1994) proposed using a radiation target screen to visualize and measure air temperature distribution. Two potential challenges have been pointed out for the measurement of air temperature: the air temperature calculation from the screen temperature and the accurate measurement of the screen temperature with the infrared camera. Effectively, an energy balance calculation has to be performed for the estimation of the air temperature from the screen temperature, including the radiant energy transferred to the screen from the surroundings and the heat transfer by convection of the air to the screen. Since the screen is at thermal equilibrium, the air temperature can be calculated with:

$$T_{air} = T_s - \frac{\varepsilon\sigma F_{s-e}\left(T_e^{\,4} - T_s^{\,4}\right)}{h_c} \tag{2.26}$$

where T_s is the surface temperature [K];

ε, the average emissivity of the surface [-];

F_{s-e}, the view factor between the surface and the environment [-];

T_e and T_s, respectively the mean environment and the surface temperatures [K]; and

h_c the convection coefficient [W/(m^2·K)]that must be measured.

If the convection heat transfer mechanism is dominant over the radiative heat transfer, the surface temperature is close to the air temperature, and the calculation with equation 2.26 is useless.

The type of screen is the key issue for the method accuracy. The type of screen has an effect on the convective and radiative heat transfer dominance as well as on the flow disturbance. Using a porous fiberglass screen, a larger turbulent boundary layer is present and the radiant exchange is much lower than the convective one due to the higher surface coefficient than an acrylic sheet (Hassini 1994). Subsequent research by Cehlin *et al* (2000) compared thin paper sheet and aluminum foil. They found that the flow was not disturbed by both screens and that the paper sheet led to more precise measurement by the infrared camera due to the high emissivity than the aluminum foil. The method effectiveness for low velocity displacement has also been demonstrated (Cehlin 2000).

As a more recent technical development, particle image velocimetry (PIV) has been successfully used in combination with infrared thermography in order to visualize together air temperature and velocity distribution (Linden *et al* 2000).

2.6 Conclusion of the literature review

In summary, air leakage through the building envelope can lead to an increase of building energy consumption and to moisture accumulation related problems. The literature review presented the current possibilities when evaluating the building envelope performance. Infrared thermography which is not a commonly used and well understood technique for building envelope evaluation has been introduced also. At this time, the methods developed for the measurement of airtightness allow a whole building envelope

airtightness rating. In addition, infrared thermography can be used for the precise location of the air leaks throughout the building envelope.

The next logical step in order to extend the knowledge in the area of building envelope airtightness evaluation would be to develop a method for the quantification of each air leak separately. Effectively, it would lead to evaluation of the increase energy consumption and moisture accumulation potential due to the different airtightness defects. Since infrared thermography is already used for evaluating the performance of the building envelope and specially to locate single defects, it would be logical to study the possibilities of using this technique for the quantification of the single air leaks.

For such a study of quantification of air leaks using infrared thermography, accurate measurement of assembly surface temperature distributions due air leaks through the building envelope, in addition to qualitative thermograms, had to first be obtained since this kind of data were not available yet.

Chapter 3 Experimental protocol

The project aimed at quantifying air leaks through the building envelope by infrared thermography. In the context of this project, an experimental protocol had to be developed first for the acquisition, using infrared thermography, of accurate matrices, in addition to qualitative thermograms, of assembly surface temperature distribution due to air leaks through the building envelope since that kind of protocol was not developed yet.

3.1 Development of the protocol

The experiment consisted of the reproduction of air leaks through a sample building envelope assembly with a crack in an environmental chamber and the recording of thermograms of assembly surface temperature distributions due to air leaks. In order to simplify the experimental set up and results analysis, the specimen tested was the physical model of a single layer envelope assembly with direct air leakage path across the assembly.

For both the overall envelope airtightness measurement and the location of the air leaks using infrared thermography in the field, procedures exist (ASTM 1996 and ASTM 1998). The experimental method developed for the actual project took into account, in terms of testing conditions, overall airtightness measurement standard methods and qualitative evaluation methods for the building envelope using infrared thermography. The conditions, of temperature and pressures differences across the assembly found in situ are known. These in situ conditions were reproduced in an environmental chamber for the actual experiment. Also, an infrared camera similar to those used for thermography surveys has been selected for the experiment. Therefore, the qualitative

thermograms and the assembly surface temperature distribution matrices due to air leaks obtained from the actual experiment would be similar to the assembly surface temperature distributions obtained by the surveyors in the field.

The existing standard method for the location of the air leaks throughout the building envelope (ASTM 1998) leads to qualitative results only. The development of the experimental procedure for the acquisition of the infrared thermography quantitative results, or accurate assembly surface temperature distribution matrices, had to look at other protocols. The related building research studies presented in Chapter 2 (section 2.5.3) were used for the development of the actual protocol. These research studies actually developed procedures for the accurate measurements of surface temperature using infrared thermography in laboratory. These procedures include the measurement of emissivity and reflected temperature and the use of a reference emitter among others. In the case of these studies, the application was different, curtain wall (2.5.3.1) in one case and air jet from diffuser (2.5.3.2) in another. Therefore, these methods had to be adapted for application of the actual experiment, i.e. air leaks through cracks in wall assemblies.

The objectives of the experimental protocol were:

1. To perform a series of tests of air leaks through the building envelope under conditions similar to field conditions for building thermography survey.
2. To develop a method, using infrared thermography in laboratory, to acquire accurate assembly surface temperature distribution matrices due to air leaks.
3. To provide a data base of thermograms and assembly surface temperature distribution matrices due to air leaks through the building envelope.

3.2 Infrared thermography equipment

3.2.1 Infrared camera and software

In the selection of an infrared camera, specifications similar to infrared cameras commonly used for qualitative in-situ building envelope surveys were used as basis. The characteristics were:

1. *the possibility of mobile on-field use*: cameras used in the field are be specially designed to be resistant to variations of temperature and to shocks;
2. *the operating temperature range*: cameras used for building survey have an operating temperature range that covers the surface temperatures met during building surveys;
3. *the detectors and system types*: cameras used by building surveyors are cameras affordable in the market;
4. *the wavelength band compatibility to the assembly surface temperatures measured and glazing material transmission wavelength band*: cameras used for building surveys are usually long wave radiation sensitive because the peak of emissivity power for assembly surface temperature fall in long wavelength band and glazing materials have lower transmissivity in long wave spectral ranges;
5. *the performance characteristics in terms of resolution and sensitivity*: cameras used in the field have good temperature sensitivity and resolution to meet the standard methods requirements;
6. *the in-built calculation tools availability for the measurement parameters correction:* cameras used during building surveys have in-built tools for the

adjustment of the temperature measured according to the emissivity, and the ambient conditions.

7. *the possibilities of image adjustment of level and range for better visualization*: cameras used for building surveys should allow setting of range/level easily during the survey for better visualization of the defects;
8. *the temperature analysis tools offered*: cameras used by building surveyors offer temperature analysis tools and facilitate thermograms analysis.

The specifications of the camera used, ThermaCAM S60 developed by FLIRSystems company, are summarized in Table 3.1. The Appendix A.1 presents also a MathCAD reproduction of the calibration curve over the temperature range of the camera.

Table 3.1 Specifications of Infrared Camera ThermaCAM S60 (derived from FLIR)

ThermaCAM S60	
Operating temperature	from -40 to 120°C
Detector	
Type	Focal Plane Array of uncooled microbolometers
Spectral range	7.5 to 13 µm
Performance	
Resolution	FOV 24° x 18° / IFOV 1.3mrad or 320x240 pixels
Sensitivity	0.08°C at 30°C
Measurement corrections	emissivity, transmission, reflected temperature
Imaging	
level/range adjustment	yes
palettes	various
analysis tools	spot, line area, histogram statistics
Accuracy	2°C or 2% of the reading

This model is accompanied by a dedicated software, ThermaCAM Researcher created by FLIRSystems company, that allows:

- live thermal event data analysis, and

- remote control of the camera.

Also, with this software, temperature data can be exported in formats compatible to common data processing softwares such as Excel or Mathlab for more specific analysis.

3.2.2 Chamber for thermography

The tests were carried out in an environmental chamber (3 m x 3 m x 2.5 m) in which the ambient temperature was controlled. Precautions had to be taken to ensure the uniformity of chamber surface temperature. The chamber had to be slightly modified for this experiment:

- the equipment generating heat was located behind the specimen, and
- the chamber walls were covered with matt paper.

These measures were taken in order to avoid uncontrolled warming of the plate surface and irregularities in the reflected temperature. The evaluation of the effectiveness of these measures was not performed.

The air jet was the only air movement considered in this experiment. The air movement induced by the air jet was not considered.

The relative humidity in the chamber could not be controlled; however, the emissivity variation due to condensation over the panel tested or atmosphere transmissivity variations were not parameters considered in this experiment. The relative humidity was not a parameter studied but was assumed to be relatively constant, around 30% RH.

3.2.3 Specimen preparation

The specimen was prepared with low-emissivity location markers (Türler *et al* 1997) that reflect the reflected temperature and appear on the thermogram with a temperature different than the one of the specimen. These markers of known locations were used as location references to retrieve the exact locations and dimensions, in the thermograms.

3.3 Experimental set-up

The experimental set-up aims at reproducing the condition of a crack, similar to those found in the building envelope. Through this crack, air, which is warmer or colder than indoor air, moves due to air pressure differences induced in a similar way as in blower door tests.

3.3.1 Specimen

A single layer assembly, represented by a plywood panel (Figure 3.1), was used in order to simplify the experimental set up and results analysis. The panel was designed to hold a crack with a length of 150 mm and an adjustable width varying from 0.5 mm to 10 mm in order to be able to test different crack widths and aspect ratios. Plywood was chosen not only for the ease of the construction of the panel, but also because this material has emissivity and reflectivity characteristics similar to common building inside wall surface materials such painted gypsum board and wood.

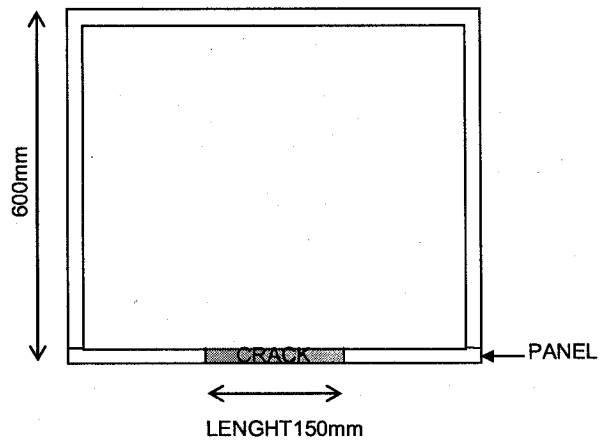

a) Plan view of the sealed box with the location of crack

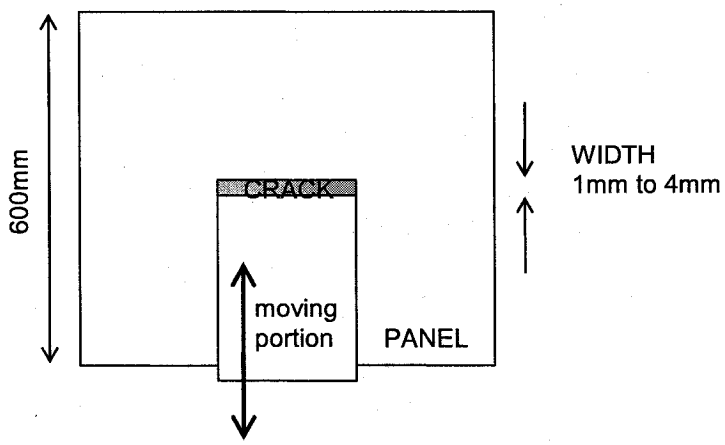

b) Face view of the tested panel with a moving portion

Figure 3.1 Sealed box and tested panel

The panel containing the crack was installed on one face of a sealed box so the panel is tested in a similar way. The set-up is similar to the use in situ for that single windows and doors using a sealed tested chamber. An air pump was connected to the box to induce air pressure differences across the panel (Figure 3.2). The air pump was needed

because a laminar flow element was used to measure the flow induced and this device lead to flow pressure losses.

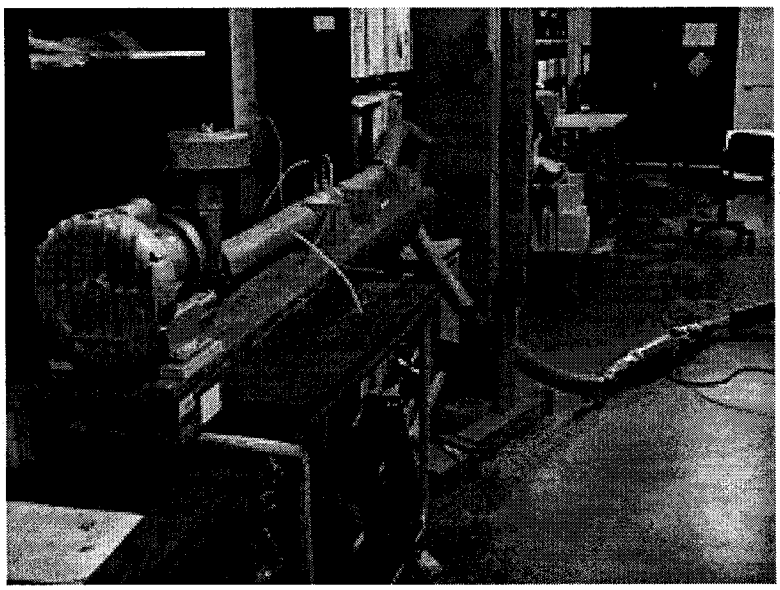

a) Air pump and electrical heating system connected to the sealed box

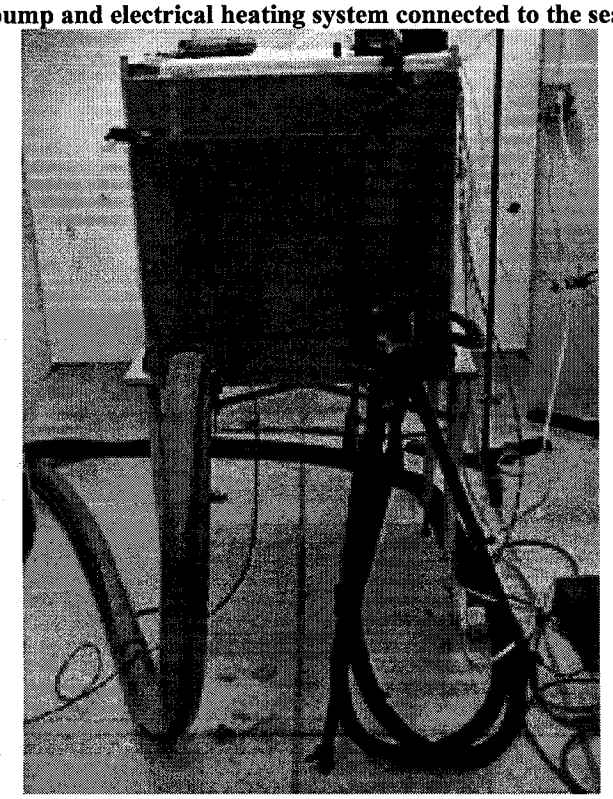

b) Specimen installed on the sealed box

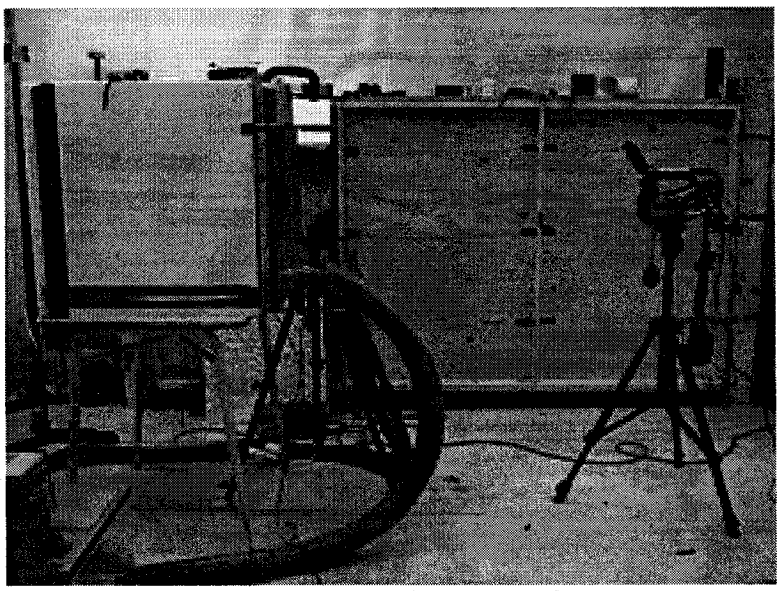

c) Sealed box in the environmental chamber

Figure 3.2 Experimental set-up developed to reproduce air leaks through the building envelope

In Canada, most blower door tests would occur when the outdoor air is colder that the indoor air. In order to simplify the experimental set-up, the experiment was undertaken with warm air entering the cold environment of the chamber. An electrically controlled light bulb installed in the box was used to heat and keep the air leaking through the crack at a set temperature.

3.3.2 Simulated conditions

The parameters of the experimental conditions and their different magnitudes tested were selected to cover the range of conditions met in the field during building envelope survey using infrared thermography. The difference of pressure across the building envelope and the temperature difference between exfiltrating air through the envelope and ambient temperature in the building were the two major condition parameters stated in standards (ASTM 1998); also, the distance between the crack and the

infrared camera and the crack width were considered as important condition parameters. The following parameters and magnitudes led to a set of 36 tests (Table 3.2):

1. opening width (1 mm, 2 mm, and 4mm);
2. pressure difference on both sides of the crack (10 Pa, 30 Pa and 50 Pa);
3. temperature of the air infiltrating through the crack (20°C and 25°C), while the chamber was kept at 10°C); and
4. distance between the specimen and the camera (0.75 m and 1.5 m).

The distances at which thermograms were taken were similar to the distances encountered in-situ during a house infrared thermography survey. The relationships between the crack dimensions and the camera resolution drove the choice of distances to be used in tests: for smaller crack widths of 1 mm, the camera was installed at a distance of 0.75 m from the crack; for the 2mm, the camera was installed at a distance of 1.5 m. The smallest crack width, 1mm, was determined as the smallest crack width accurately measurable with the equipment available. The larger crack width, 4mm, although wider that most cracks encountered in the field, was tested for comparison purpose. The distances are similar to the distances used in the field to record thermograms of defects. They are common distances available in small rooms. Also, the fields of view of the camera at those distances allow to have thermograms including the defect found and a section of the assembly without defect.

Table 3.2 Experimental Conditions

	opening [m]					ΔTemp [°C]		ΔP [Pa]			distance [m]	
	length		width									
	0.075	0.15	0.001	0.002	0.004	10	15	10	30	50	0.75	1.5
test 1		x	x				x	x			x	
test 2		x	x				x	x				x
test 3		x	x				x		x		x	
test 4		x	x				x		x			x
test 5		x	x				x			x	x	
test 6		x	x				x			x		x
test 7		x	x			x		x			x	
test 8		x	x			x		x				x
test 9		x	x			x			x		x	
test 10		x	x			x			x			x
test 11		x	x			x				x	x	
test 12		x	x			x				x		x
test 13		x		x		x		x			x	
test 14		x		x		x		x				x
test 15		x		x		x			x		x	
test 16		x		x		x			x			x
test 17		x		x		x				x	x	
test 18		x		x		x				x		x
test 19		x		x			x	x			x	
test 20		x		x			x	x				x
test 21		x		x			x		x		x	
test 22		x		x			x		x			x
test 23		x		x			x			x	x	
test 24		x		x			x			x		x
test 25	x				x	x		x			x	
test 26	x				x	x		x				x
test 27	x				x	x			x		x	
test 28	x				x	x			x			x
test 29	x				x	x				x	x	
test 30	x				x	x				x		x
test 31	x				x		x	x			x	
test 32	x				x		x	x				x
test 33	x				x		x		x		x	
test 34	x				x		x		x			x
test 35	x				x		x			x	x	
test 36	x				x		x			x		x

Parameters monitored for each tests

The stability of the parameters and the surface temperature of the plate had to be verified before the thermographic data recording of each test. Also, the parameters had to be measured precisely and noted down at the moment of the thermographic data recording for further analysis. Furthermore, the flow rate had to be also measured for

each test for supplementary analysis. Table 3.3 shows the measured parameters and the apparatus used.

Table 3.3 Condition parameters, magnitudes tested and monitoring equipment used

Parameters	Magnitudes	Measurement apparetus
Crack width	0.001 / 0.002/ 0.004 m	Various thickness metal sheets
Camera distance	0.75 / 1.5 m	Ruler
Air to ambiant temperature difference	10 / 15 °C	Thermocouples
Pressure difference through the envelope	10 / 30 / 50 Pa	Manometer
Air flow		Laminar flow element

For the measurement of air temperatures, thermocouples were used. Figure 3.3 shows the location of the thermocouple used for the measurement of the leaking air temperature. Pressure differences between both sides of the panel were measured with a manometer. The laminar flow element coupled with a flow meter previously installed with the pump, was used for the airflow rates measurement. For distances, markers on the floor were precisely installed. Metal sheets 1, 2 and 4 mm thick were used to set the opening width of the crack for each test.

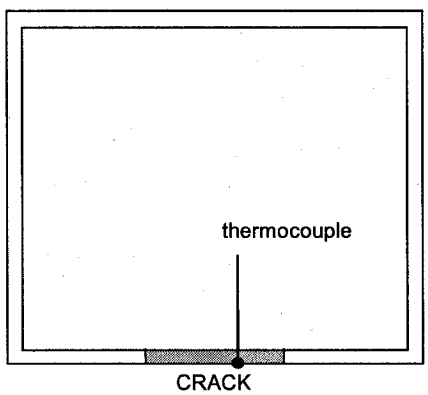

Figure 3.3

Section view of the sealed box at the crack height and location of the thermocouple used box for the measurement of the leaking air temperature

A data acquisition system was used to electronically monitor the air temperature in the crack space and the ambient air temperatures. However, the pressure difference between both side of the panels and the flow rate had to be monitored manually. The distance and the crack width were set prior the tests.

A parameter monitoring sheet (Appendix B1) was produced to be filled for each test. Upon attainment of steady-state of air temperatures, the parameters were recorded every 30 seconds with the data acquisition system for ten minutes and the mean calculated. Pressure differences and flow rates were checked regularly and recorded before and during the thermographic data recording time.

The flow rate measurement necessitated two corrections. First, because the laminar flow element is calibrated for a specific air viscosity, the measured flow had to be adjusted according to the viscosity of the air at the laminar flow element measurement position according to the tables provided by the manufacturer. Then, the flow rate at the crack position had to be calculated from the flow rate corrected according to the air density difference between the two positions with:

$$Q_v = \frac{Q_{vLFE} * \rho_{LFE}}{\rho_{crack}} \tag{3.1}$$

where Q_v is the volumetric flow [m^3/s];

Q_{vLFE}, the volume air flow [m^3/s] at the laminar flow element measurement point;

ρ_{LFE}, the air density [kg/m^3] at that location;

ρ_{crack}, the air density [kg/m^3] at the crack location.

No significant differences have been observed between the measured and corrected values because the air viscosities and densities tested were not different enough.

3.4 Experimental procedure

With the objective of acquiring the most precise and accurate thermographic data, an experimental procedure for the thermographic data acquisition has been developed based on several standard methods (ASTM 1996, ASTM 1998, ASTM 1999, ASTM 1997a, ISO 1983) primarily created for field building surveys and on laboratory thermography procedures of three laboratories (Elmahdy 1996, Türler *et al* 1997, Ge *et al* 2001).

The procedure started with two preliminary tests to characterize the sample surface emissivity and the infrared reflected temperature conditions. After verification of the steady-state conditions, the 36 tests were undertaken using the reference emitter technique. Finally, the recorded data was processed before the analysis. Appendix C1 presents a schema of the experimental procedure.

3.4.1 Emissivity measurement

The following method from ASTM Standard Test Method E1933 (1999) was used to measure the plywood panel emissivity. A piece of the material was mounted on the reference emitter and heated to achieve a 10°C difference with respect to ambient conditions. A portion of the material painted black was used as a black body reference as shown in Figure 3.4. The temperatures measured by the camera over each section were compared setting the emissivity value to 1 in the camera menu. The emissivity was then

adjusted until the temperature recorded over the unpainted section was the same as the temperature measured on the painted section.

Figure 3.4 Piece of plywood heated used for the measurement of plywood emissivity

3.4.2 Reflected temperature

The procedure of ASTM E1862 (1997a) was followed to measure the reflected temperature. An aluminum sheet had to be wrinkled (Figure 3.5) to present the same diffuse reflective characteristics as the tested plywood used for the test. Thermograms of the plate were taken with the emissivity set to 1 before the tests. The average temperature measured over the plate would be the equivalent to the background temperature.

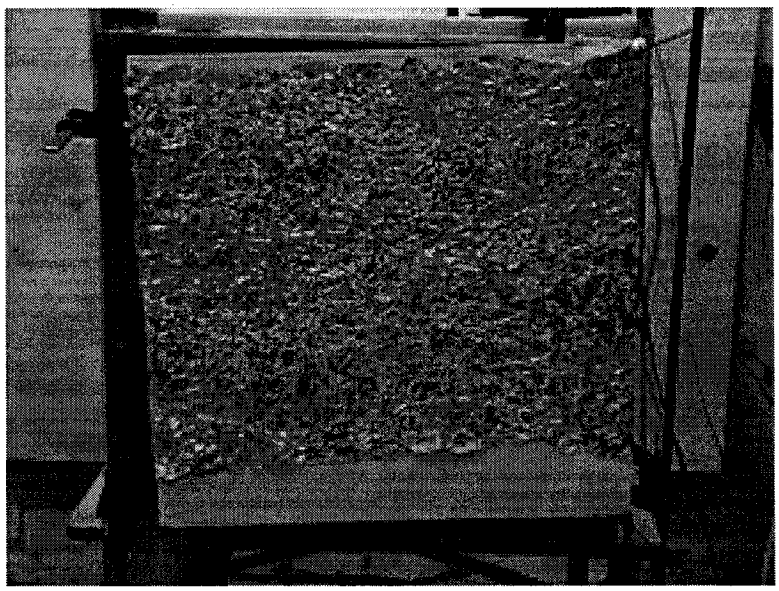

Figure 3.5 Aluminum foil used for the measurement of the background temperature

3.4.3 Steady-state verification

In addition to the stability of the conditions and the leaking air temperature itself, the temperature stability of assembly surface temperatures was verified before thermographic data recording for each test. The dedicated software was used for live analysis of the assembly surface temperature before steady-state was established.

3.4.4 Reference emitter

The reference emitter technique proposed by Türler *et al* (1997) has been followed. A customized reference emitter, previously designed for an experiment by Ge (2002), was installed in the field of view of each thermogram. The reference emitter was made from a solid block of copper in which a continuous fluid channel was machined. The device was insulated on five faces except for the front. The block was connected to a

constant temperature bath (Appendix D1). The reference emitter was covered with a thin piece of the plywood used for the experiment (Figure 3.6).

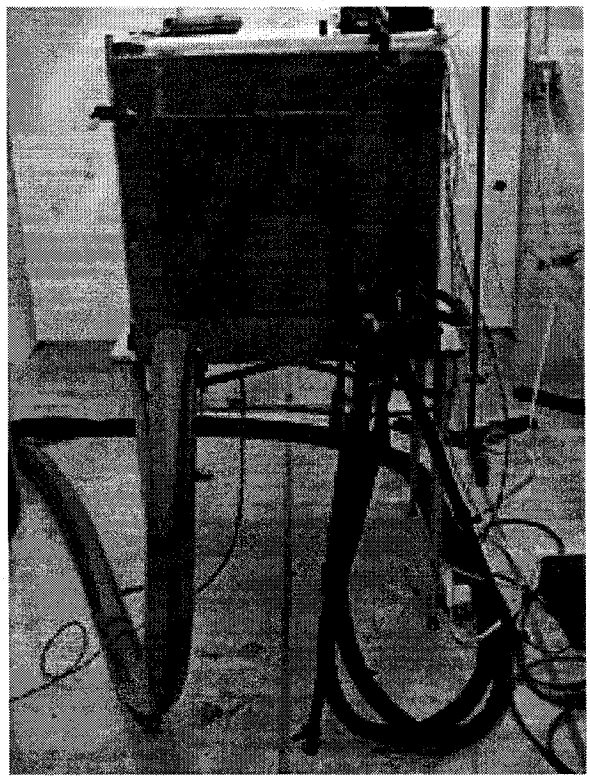

Figure 3.6 Reference emitter used to estimate the temperature offset measured by the camera installed in the field of view of the tested panel thermograms

If the reference emitter had been at less than 5°C of the surface temperature as advised by Türler *et al* (1997), the inbuilt resistance temperature detector would have had to be used for the surface temperature estimation. Then, the thin wood piece resistance and surface coefficient would have had to be known to calculate the surface temperature. However, the reference emitter was kept at ambient temperature to allow the measurement of its surface temperature with a surface mounted thermocouple. The

reference emitter temperature was actually 10 to 15 °C or lower than the surface temperature.

The temperature offset calculated between the reference emitter temperature using the thermocouple and the camera have been subtracted or added linearly to all the panel surface temperatures (Türler *et al* 1997) using the formula:

$$T = T_{IR} - \left(T_{IRref} - T_{ref}\right) \tag{3.2}$$

where T is the corrected temperature [°C];

T_{IR}, the temperature [°C] measured by the camera;

T_{IRref}, the temperature [°C] measured by the camera over the reference; and

T_{ref}, the temperature [°C] measured by the thermocouple.

In addition, the shutter included in the camera was manually activated before the recording of each thermogram. This shutter eliminates the influence of all internal radiation sources located anywhere from the reference back to the detector itself.

3.4.5 Thermograms recording

Upon attainment of steady state regime, one thermogram of the front of the panel of the tested assembly was recorded for each of the 36 tests. These thermograms were recorded for the development of the methods for quantification of air leaks in terms of crack dimensions using infrared thermography.

In addition to these thermograms, one thermogram of a paper sheet positioned perpendicularly (Figure 3.7) to the air flow was taken for each test, based on the method developed by Hassini (1994) and Cehlin *et al* (2000). These thermograms have been recorded in order to study the air jet temperature distribution. The screen temperature is

used, in the context of this thesis, to qualitatively study the air jet temperature distributions. The estimates of the air temperature in the jet would require the formulation of the energy balance (Section 2.5.3.2).

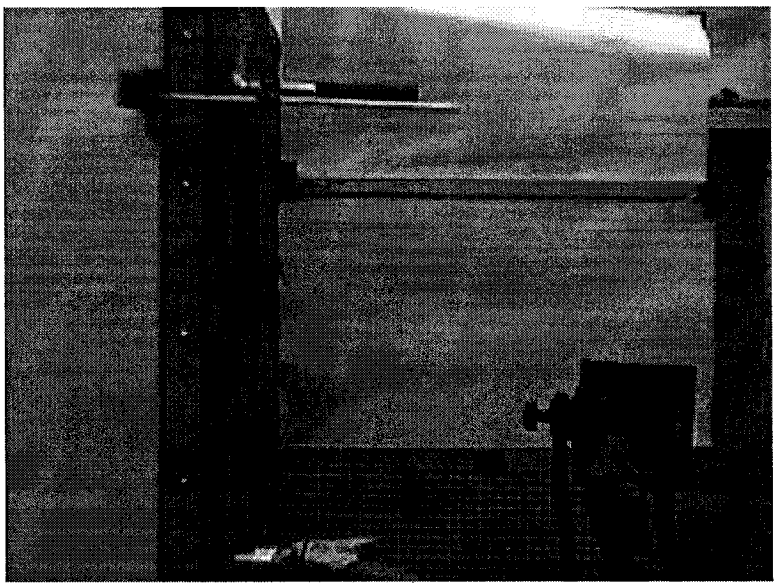

Figure 3.7 Paper screen used for the visualization of air jet temperature distribution

3.4.6 Data Processing

Two levels of data processing were used to obtain accurate temperature measurements (Appendix C2). First, corrections were done with the help of the dedicated software for the parameters affecting the infrared measurements: emissivity, background temperature, ambient relative humidity and temperature, and distance.

Second, temperature matrices were extracted from the thermograms and were transferred to the data processing software. The infrared temperature data of each thermogram were scaled according to the temperature differences of the reference emitter. Also, with the help of the low-emissivity markers, coordinate axes were

incorporated to the temperature matrices giving the spatial location of each temperature data.

3.5 Error Analysis

The accuracy calculation is an important issue when measuring temperature with thermography in order to analyze the significance of error sources and try to minimize them. Analyzing the accuracy of surface temperature measurement obtained using a reference emitter, the magnitude of the error on the surface temperature distributions presented in Sections 4.3 and 4.4 has been estimated and several error analyses have been performed.

3.5.1 Measurement Error

Information about the measurement accuracy as provided by the manufacturer is given both in absolute and relative terms. In the case of the camera used in the project, the error is ± 2°C or 2% of the temperature in °C, implying that the highest value of relative or absolute value should be used. This error is specified for a blackbody at short distance.

For a non blackbody surface in other conditions than 30°C and short distance, the total error, is the sum of the partial errors of each parameter of the radiometry equation. The total accuracy on temperature measurement is calculated with (Öhman 2001):

$$\Delta T = \pm\sqrt{\left(\frac{\delta T_s}{\delta \varepsilon}\cdot\Delta\varepsilon\right)^2+\left(\frac{\delta T_s}{\delta T_r}\cdot\Delta T_r\right)^2+\left(\frac{\delta T_s}{\delta \tau}\cdot\Delta\tau\right)^2+\left(\frac{\delta T_s}{\delta T_{amb}}\cdot\Delta T_{amb}\right)^2+\left(\frac{\delta T_s}{\delta T_{tot}}\cdot\Delta T_{tot}\right)^2} \tag{3.3}$$

where ε is the emissivity of the object;

τ the transmissivity of the atmosphere;

T_s, is the surface temperature [K];

T_r and T_{amb}, are the reflected temperature, and ambient temperature [K]; and

T_{tot}, the temperature of the total radiation that reaches the detector of the camera [K].

Since the variables and parameters are related to the temperature by using the calibration curve of the camera (eq. 2.23), the calculation of the each of the partial errors must be done in two steps:

$$\Delta T_p = \frac{\delta T_s}{\delta I} \cdot \frac{\delta I}{\delta p} \cdot \Delta p \tag{3.4}$$

where I is the calibration curve [output unit of the camera]; and

p stands for parameter.

The calculation program 'Temp_err.xls' created by FLIR Systems (Öhman 2001) was used to calculate the accuracy under the experimental conditions tested. For the calculations, no error has been considered for the atmosphere transmittance, $\Delta\tau$, because the atmosphere transmittance was equal to the unity for the distance and condition tested. No error has been considered also for the emissivity measurement; the total error on emissivity would have to be calculated rearranging the radiometry equation so that the emissivity is isolated. The thermocouple error on temperature measurement has been used for the ambient temperature measured, ΔT_{amb}. The error on the total temperature measurement, ΔT_{tot}, includes errors due to the offset and the camera calibration unfit since the error related to random noise is in comparison negligible (Öhman 2001). The error on reflected temperature measurement was calculated with the same program setting the emissivity equal to one; the error, ΔT_r, was equal to 1.81°C.

The Appendix E (Figure E.1) shows the total error results in table and plot. There was no partial error related to emissivity and transmissivity under the tested conditions. There was also no error related to ambient temperature, because the atmosphere transmissivity being equal to the unity, its emissivity is zero. Therefore, the major sources of error are the reflected temperature and, mainly, the error of camera offset and response. For an object in similar conditions to the conditions tested, or surface temperature at 20°C inside a room at 10°C, the total error on absolute temperature measurement was 2.48°C.

3.5.2 Error on referenced temperature measurement

The error on temperature measurement using a reference emitter was analyzed by Türler *et al* (1997). In this analysis, the error on the temperature measurement using thermography with a reference emitter is (Türler *et al* 1997):

$$\Delta T_{IR} = \pm\sqrt{\left(\frac{\delta T_s}{\delta \varepsilon}\cdot \Delta\varepsilon\right)^2 + \left(\frac{\delta T_s}{\delta T_r}\cdot \Delta T_r\right)^2 + \left(\frac{\delta T_s}{\delta T_{tot}}\cdot \Delta T_{tot}\right)^2} \qquad (3.5)$$

The transmissivity and atmosphere was not considered in the calculation. The emissivity error would have to be calculated based on the radiometry equation rearranged so that the emissivity is isolated. The random noise, notion presented and discussed earlier in section 2.4.2 of the thesis, is taken into account for the total equivalent temperature error and the background error. The random noise can also be reduced by averaging the data over space and time. The final error is calculated with:

$$\Delta T = \Delta T_{IR} + \Delta T_{ref} + \Delta T_{TC} + \Delta T_{FOV} \qquad (3.6)$$

where ΔT_{IR} is the error on temperature measurement using thermography with a reference emitter;

ΔT_{ref}, the reference emitter temperature setting error [K];

ΔT_{TC}, the thermocouple temperature error [K]; and

ΔT_{FOV}, that can be measured comparing every data inside a field of view of thermograms [K].

An analysis by Türler *et al* (1997) for the measurement of temperature using infrared thermography for an experiment on thermal resistance value of glazing units undertaken in an environmental chamber using the reference emitter technique led to an error value of 0.5°C.

3.5.3 Error calculation for the present experiment

The error for the experiment set up and conditions has been calculated with:

$$\Delta T_{IR} = \pm \sqrt{\left(\frac{\delta T_s}{\delta T_r} \cdot \Delta T_r\right)^2 + \left(\frac{\delta T_s}{\delta T_{amb}} \cdot \Delta T_{amb}\right)^2 + \left(\frac{\delta T_s}{\delta T_{tot}} \cdot \Delta T_{tot}\right)^2} \qquad (3.7)$$

For the calculations, no error was considered for the atmosphere transmittance. The transmittance is automatically computed by an in-built tool in the camera using distance, and atmosphere temperature. This assumption is acceptable because the atmosphere transmittance was equal to the unity for the distance and condition tested. No error has been calculated for the emissivity measurement (Section 3.4.1). The ambient temperature error was equal to the thermocouple error or 0.5°C. The error on the reflected temperature was judged equal to 0.5°C. It would have been equal to the random noise level plus the thermocouple; however, in averaging of the data over the field of view, the

reflected temperature error is diminished significantly (Section 3.4.2). For the error on the total temperature, which is equal to the random noise level, the Noise Equivalent Temperature Difference (NETD), or the precision which is equal to 0.08°C for the ThermaCAM S60, was used because no measurement of the noise level was undertaken.

The total error on the temperature measurement has been calculated with:

$$\Delta T = \Delta T_{IR} + \Delta T_{TC} \tag{3.8}$$

where ΔT_{IR} is the error computed using equation 3.7; and

ΔT_{TC} is the thermocouple temperature error [K].

The error on the temperature of the reference emitter was not measured. The performance across the field of view of the camera would be a relevant source of error to measure.

The Appendix E2 presents a MathCAD calculation of the accuracy under the experimental conditions using a reference emitter. The accuracy on temperature measurement for a 20°C surface was calculated to be 0.6°C. This value is much lower than the 1.87°C value calculated for the experiment without the use of a reference emitter (Section 3.5.1) and similar to the 0.5°C value calculate by Türler *et al* (1997) for a similar experiment.

3.6 Summary of the experimental protocol

In summary, an experimental protocol was developed for the acquisition, using infrared thermography, of thermograms of assembly surface temperature distributions due air leaks through the building envelope. Air leaks through a single layer assembly holding cracks (1 and 2 mm by 0.150m and 4 mm by 0.075mm) were reproduced in an

environmental chamber. The air leaks were induced by air pressure differences of 10, 30 and 50 Pa and the temperature of the leaking air was 10°C and 15°C higher than the ambient temperature in the chamber. Thermograms were recorded at distances of 0.75 and 1.5m between the camera and the assembly.

The radiometric measurement parameters (emissivity, and ambient and reflected temperature) were measured so to adjust the temperature results. The reference emitter technique was implemented to improve the accuracy of the absolute temperature measurement using thermography.

A series of 36 tests have been carried out following this procedure in order to obtain a data base of thermograms and, extracted from these thermograms, assembly surface temperature distribution matrices due to air leaks through the building envelope. The error on the absolute temperature measurement using the reference emitter technique has been estimated to ±0.6°C. Also, thermograms of a paper screen installed perpendicularly to the crack were recorded.

The monitored variables, the thermograms, and the assembly surface temperature distribution matrices are presented and analyzed in the next chapter.

Chapter 4 Analysis

This chapter presents the analysis of the monitored conditions, the different parameters measured throughout the experimental procedure, the thermograms and the assembly surface temperature distribution matrices due to air leaks through the assembly.

First, the experimental results from the monitoring of the experimental conditions are presented in order to assess the achievement of the conditions determined for the tests (Section 4.1.1). Also, the different parameters such as emissivity, reflected temperature, and offset of the reference emitter measured throughout the experimental procedure are discussed in order to evaluate the efficiency of the experimental protocol (Section 4.1).

Then, the thermograms of assembly surface temperature distributions due to air leaks are analyzed in qualitative way (Section 4.2). Therefore, the qualitative relation between different air leaks, in terms of temperature and pressure difference and crack width can be highlighted. In addition, the thermograms of the supplementary test carried out using the paper screen are qualitatively analyzed in order to characterize the air leak jet.

For the quantitative analysis, relationships between the shape of the temperature profiles, which have been extracted from the assembly surface temperature distribution matrices, on the lateral and longitudinal axes of the cracks and the crack dimensions are highlighted (Section 4.3.2). Also, temperature measured at the crack location using infrared thermography and established relationships with crack widths are presented (Section 4.3.3).

Finally, two additional methods developed for accurate crack sizing of building envelope cracks using thermograms of assembly surface temperature distributions due to air leaks obtained from infrared thermography are presented and discussed (4.4). The first method is based on image segmentation technique and the second on tomography.

4.1 Experimental results

4.1.1 Monitoring of the conditions

The stability of air temperature, ambient temperature, pressure difference and flow was achieved with the set-up. The experimental conditions monitored are presented for each test in Appendix F. Also, the variations of the conditions during the tests have been considered negligible.

4.1.2 Emissivity

The painted section of the plywood effectively showed a higher temperature than the plain one (Figure 4.1). The measured emissivity value of the plywood was 0.87 which is comparable to the value of 0.9 that is commonly used for this material; and to the tabulated value of 0.82 (FLIR 2004).

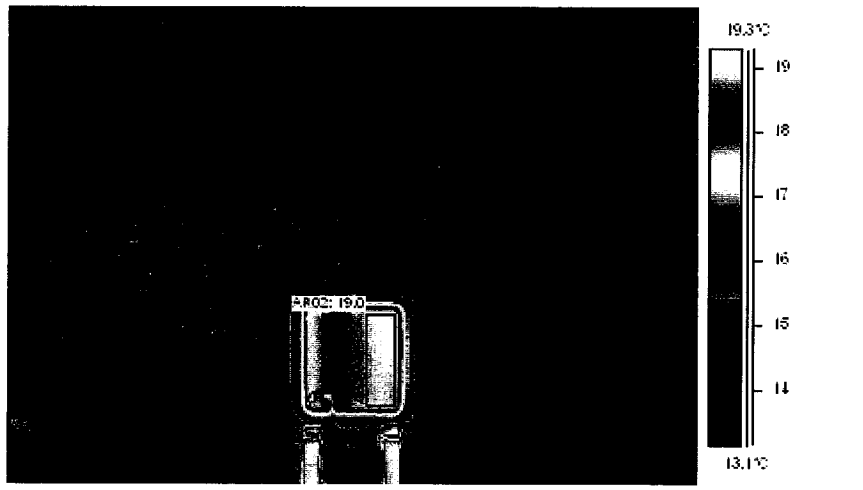

Figure 4.1 Thermogram taken for the emissivity measurement using heated piece of the material with one section painted in black

The measured emissivity is the emissivity normal to the surface that is effective for the spectral range of the camera at the tested temperature. For this experiment, the panel surface is considered to be a grey surface that does not change the emissivity with temperature. These assumptions are realistic because the temperatures range under which the plywood was tested was small. Also, for the range of angles between the panel and the camera view used for this experiment, the emissivity of the panel surface can be considered constant.

4.1.3 Reflected temperature

The measured reflected temperature which was about 2°C greater than the ambient temperature can be explained by the presence of the camera and lights. The operator was not inside the chamber during tests; thus, her presence did not affect the correction. Figure 4.2 shows the thermogram of the reflected temperature mirror. The

reflected temperature was used measured only once as ambient conditions were constant for the entire the set of tests.

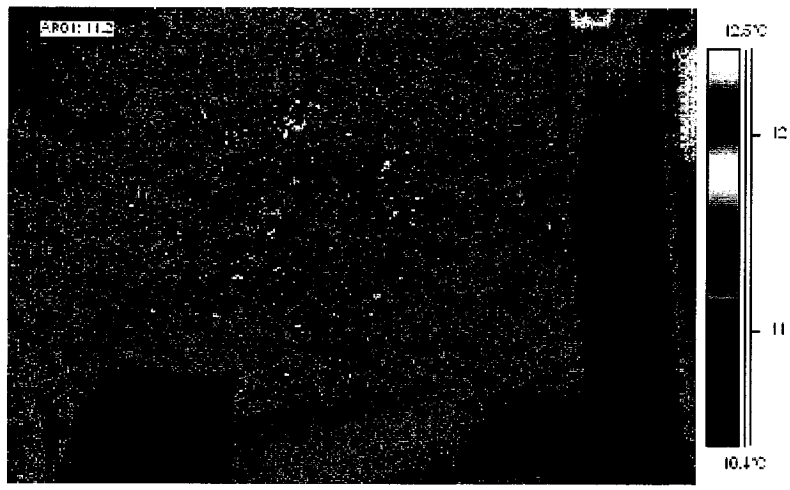

Figure 4.2 Thermogram of the aluminum mirror used to measure the reflected temperature

4.1.4 Time required to achieve steady-state regime

A ten-minute period was generally enough to achieve stable surface temperature of the panel after the system had reached steady state. The temperature bin distribution, the maximum, minimum, and average temperature and the profiles stablity were verified for this purpose using the dedicated software. An example of the software screen is in Appendix G. The ten-minute period corresponds to the minimal period needed before field localisation of air leaks through the building envelope according to the relevant standard method (ASTM 1998).

4.1.5 Data Processing

The following comments were made on the effects of the corrections using the in-built calculation tool according to the measurement parameters on the temperature

measured. The distance, and the ambient relative humidity and temperature had no effect, because the atmosphere transmissivity does not change at short distance; emissivity and the background temperature have a combined effect going up to more than 1°C. Under the tested conditions, setting the emissivity of the 20°C assembly equal to what 1, the temperature measured is equal to 18.9°C; while setting the emissivity to 0.87, the temperature measured is 20.2°C. Finally, setting the right reflected temperature at 12°C, the temperature measured becomes 20.0°C. Therefore, under the condition tested, the setting of the emissivity and the reflected temperature have a noticeable effect on the temperature adjustment; whereas, precise ambient relative humidity and temperature, and distance setting do not really affect the temperature to be measured.

The magnitude of radiation from the surface and the reflected radiation under the condition tested have been calculated (Appendix H) in order to have an idea of the proportion of the radiation reaching the detector that comes from the surface and that is reflected. In fact, for a 20°C surface with 12°C reflected temperature, 88% of the radiation that reached the detector was emitted radiation while more that 12% was reflected radiation of the background.

4.1.6 Reference emitter

Linear corrections have been done using the offset measured over the reference emitter because of the small temperature difference between the reference and the surface. To have an idea of the difference between the linear corrections used and the equivalent nonlinear corrections, taking into account the calibration curve, they have been both calculated (Appendix I1 and I2). A 0.5°C correction due to an infrared

temperature measured of 10.5°C over a 10°C reference emitter is equivalent to a correction of 0.49°C and 0.56°C on 20°C and 25°C surfaces respectively.

The offsets between infrared measurements of the reference emitter temperature and thermocouple measurement of the reference emitter (Appendix I3) were generally positive. The temperature measured was, in average, 0.2°C higher than the reference temperature. Therefore, the camera was reading higher temperatures. However, the average value of 0.2°C is inside the thermocouple accuracy magnitude which is equal to 0.5°C.

The preciseness of this correction has not been demonstrated with the data obtained in this experiment. The only other temperatures measured with a contact sensor were the ambient air and air temperature at the crack location and were not surface temperatures.

4. 2 Qualitative Analysis of the thermograms

Thermograms of the 36 tests were first examined and compared qualitatively. At the thermogram stage, temperature data were adjusted according to the measurement parameters. However, the temperature data at this stage were not scaled according to the reference emitter. In a thermogram field of view (Figure 4.3a), the crack is located where there are high temperatures at the center of the image. The four low-emissivity markers are also visible; they delimit the area to be analyzed. The reference emitter stands in the left corner of the image. The level and range of temperature were adjusted to cover only the panel surface temperature span; therefore, details of the temperature gradient have been emphasized (Figure 4.3 b).

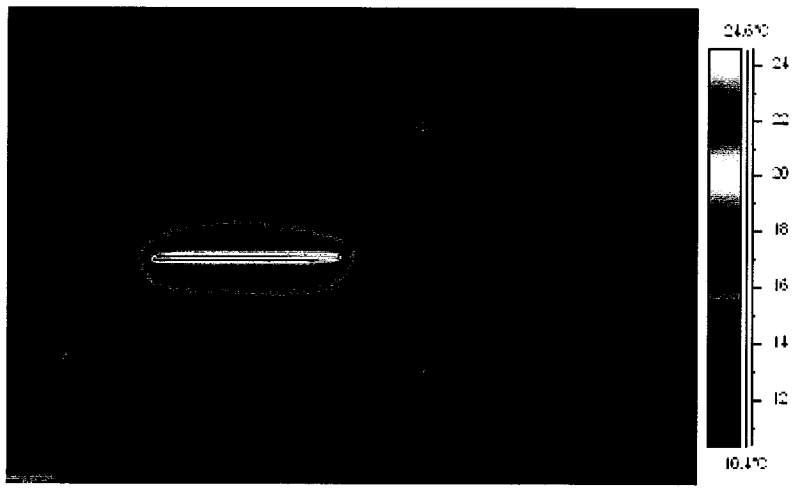

a)

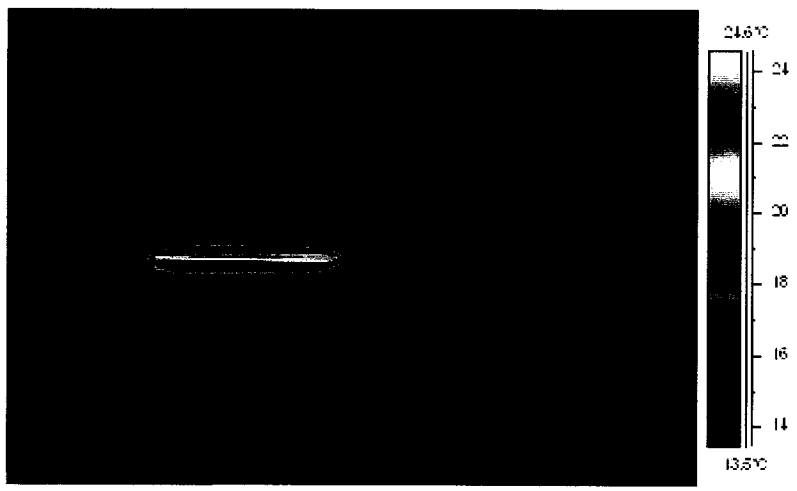

b)

Figure 4.3 Thermogram of the panel surface temperature distribution due to air leaks setting without setting (a) and setting Level/Range to cover the temperature range (b)

In addition to the level and span setting, different color palettes can be used to enhance the thermograms. The palette *Rain*, which passes from violet to red continuously, has been used for the analysis; however, the palette rain 10, which is palette rain but reduced to ten shades, was also tested (Figure 4.4). The result shows that

temperature variations are emphasized, but details in variations are lost. The previous observations about thermograms settings and enhancement can be used for advising field building surveyors. Hence, the level and range of temperature do not need to be adjusted to the precise air leak and surface wall temperature because no temperature variation details need to be known. The airtightness defect could even be located more easily using a palette with few shades in complement to a larger temperature range. However, if small temperature differences between the air leak and the surface wall temperature are expected, these details could be unseen.

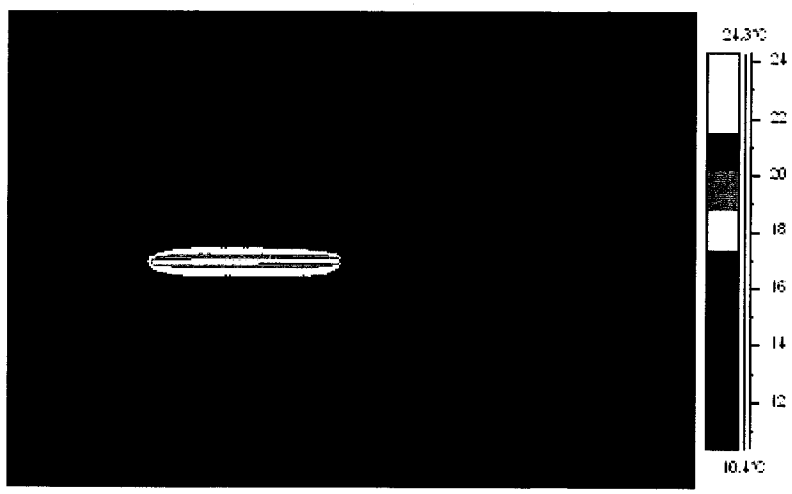

Figure 4.4 Thermogram of the panel surface temperature distribution due to air leaks using a few colors palette

4.2.1 Experimental conditions effects on thermograms

By comparing three thermograms of the surface temperature of the assembly (Figure 4.5) taken respectively with 50, 30 and 10 Pa pressure differences, while the other conditions remained constant, it can be noticed that the temperature pattern is

slightly different in shape. Also, the air leak has an effect on a zone of smaller area as the pressure difference decreases.

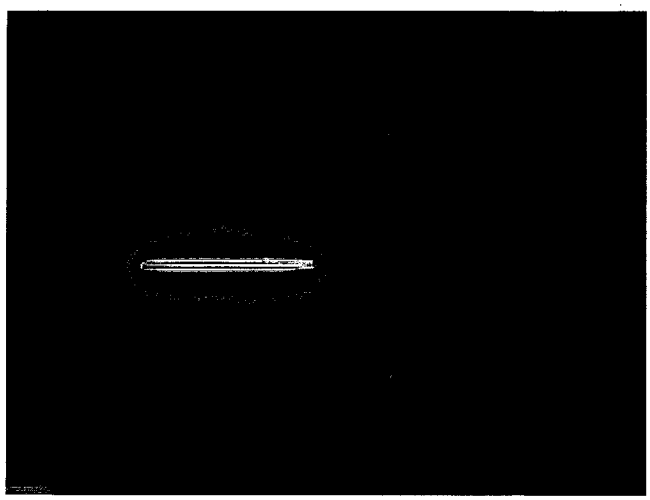

a)

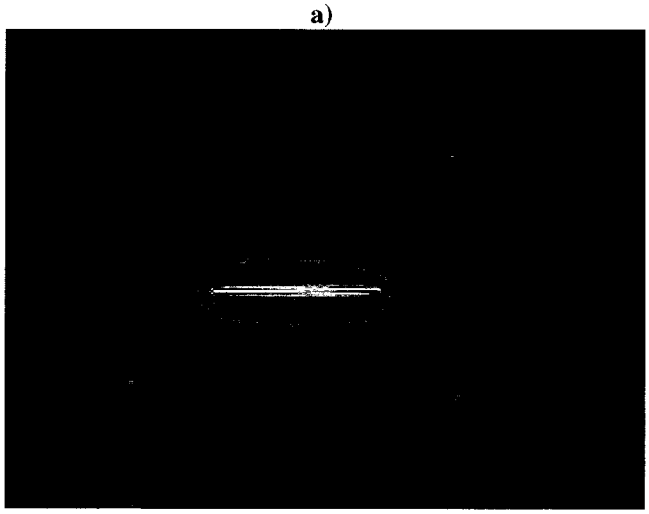

b)

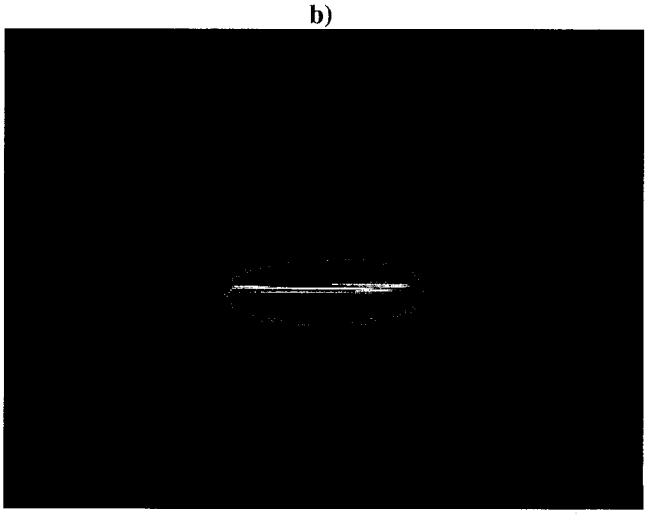

c)

Figure 4.5 Thermogram of the panel surface temperature distribution due to air leaks under 50 Pa (a), 30 Pa (b) and 10 Pa (c) pressure differences

By comparing two thermograms taken under different temperature differences (Figure 4.6), it can be noticed that the air leak has an effect on a zone of smaller area as the temperature difference between the leaking air and the ambient conditions decreases.

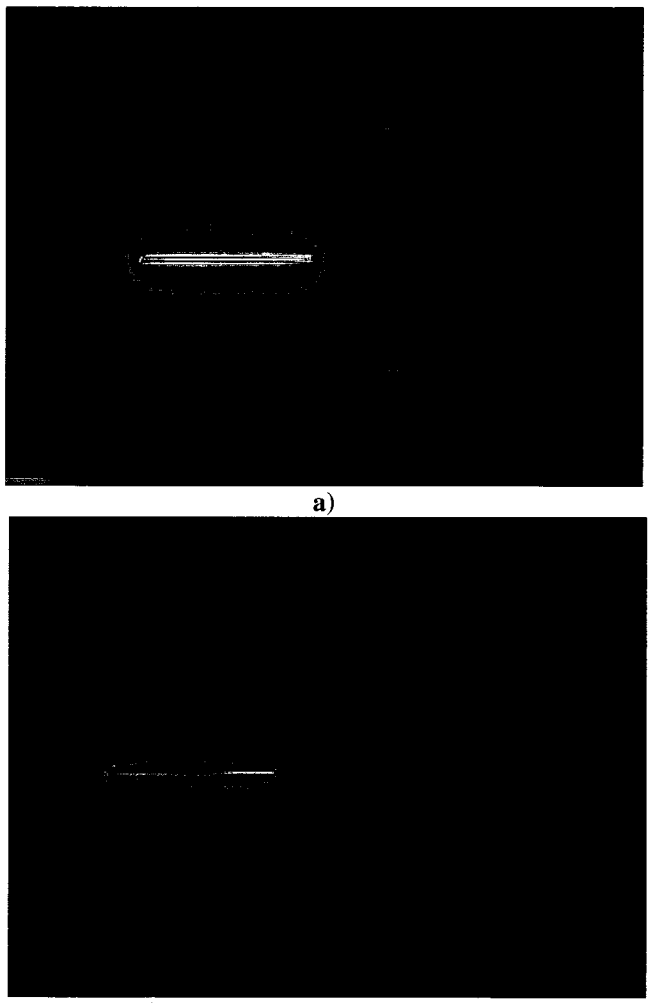

a)

b)

Figure 4.6 Thermogram of the panel surface temperature distribution due to air leaks under 15°C (a) and 10°C (b) temperature differentials between leaking and ambient air temperature

Finally, the comparison of the temperature pattern of leaks coming through different crack widths demonstrates that the air leak affects a zone of larger area when the crack width increases (Figure 4.7).

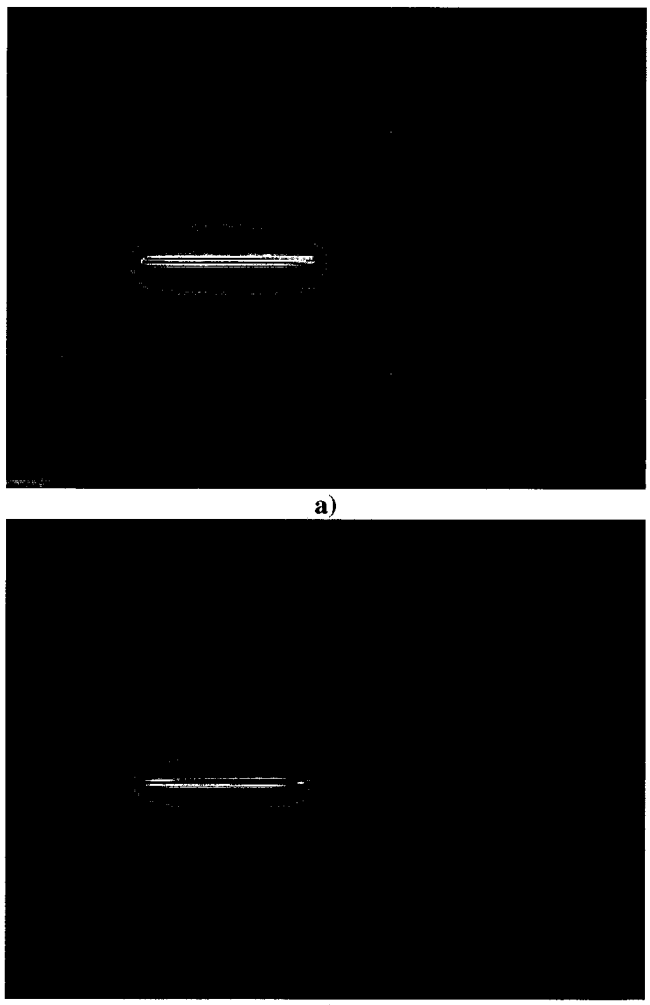

a)

b)

Figure 4.7 Thermogram of the panel surface temperature distribution due to air leaks for 2mm (a) and 1mm (b) crack widths

4.2.2 Screen Thermograms

The thermograms from the perpendicular screen cannot be compared in the same way. Actually, the right paper type has not been used for the first half of the experiments. In addition, the screen was not kept at the right position, i.e. perpendicular to the air jet Moreover, the lens used for this test did not allow the visualization of the total jet in the field of view. For the second half of the experimental work, a wider lens was used and

the paper screen changed together with its support. Nevertheless, the influence the pressure and temperature on the jet visualization was not important. The screen position appeared to differ between one thermogram to another, when looking at the air temperature jet mapping. In addition, the temperature difference from the measured reference emitter and the temperature measured by the thermocouple was varying largely from one thermogram to another.

One of the temperature patterns on the paper screen (Figure 4.8 a) can be compared to the theoretical behavior of a similar jet. The air leak has been considered as a free nonisothermal linear jet (ASHRAE 2001). The jet flow is expected to be approximately two-dimensional and at some distance, to become three dimensional. The air velocities are symmetric with the plane air jet plane. Finally, the trajectory can be affected by the buoyancy effect due to air density differences. Also, the air at the boundary of the jet is entrained in the flow so the volume of air increases so that a secondary circulation is caused in the space.

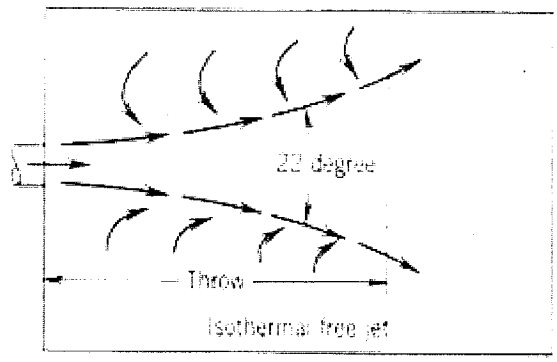

a)

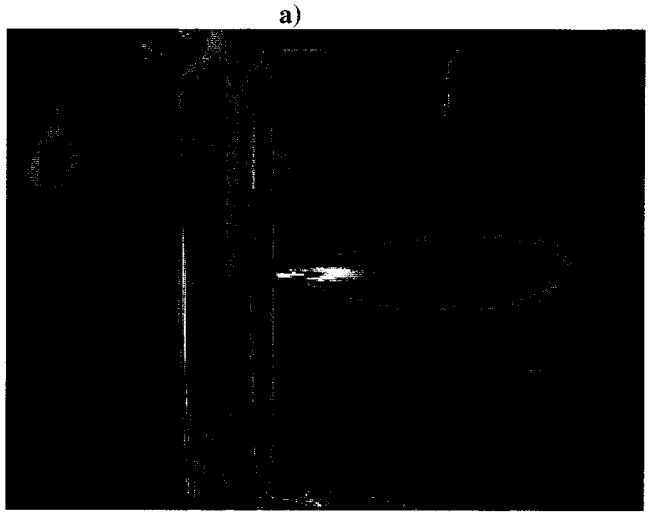

b)

Figure 4.8 Theoretical air jet (from McQuiston et al 2000) (a) and thermogram of the paper screen installed perpendicularly to the air jet (b)

The following general observations can be made:

1. the air jet volume increases effectively because of air entrained in the flow;
2. the trajectory does not seem to be affected by the buoyancy effect due to air density differences; and
3. there is no sign of recirculation or this recirculation is at room air temperature.

In order to use this method for quantitative analysis of air jet temperatures, obviously, a better set up would have to be developed for the screen first. Also, the quantitative analysis of the temperature data would require two dimensions analysis of

the temperature matrices. Energy balance calculations would have to be done to calculate air temperature distributions from paper screen distributions (Hassini 1994). The effect of the screen on the jet should be studied also.

4.2.3 Conclusion of the qualitative analysis

The analysis of the thermograms showed that the shape and area of the zone affected by the air leak change with the different pressure and temperature differentials and crack widths. Also, by comparing the thermograms taken of a screen paper, the air jet of the air leak can be characterized. The air jet behaves as a free air jet not affected buoyancy effect; also, the recirculation induced by the air jet in the room is not visible on the screen thermogram. Since, the qualitative analysis cannot lead to the crack sizing, a quantitative analysis of the assembly surface temperature distributions due to air leaks had to be done in order to develop crack sizing methods.

4.3 Quantitative Analysis

Before starting the quantitative analysis of the assembly surface temperature distributions, the notion of image degradation must be presented since such degradation has an effect on thermographic image and, therefore, on the data to be analyzed in the following two sections.

4.3.1 Data degradations

To introduce the notion of image degradation, the relations between an ideal camera response and the different degradations are mathematically described below. A brief description of the different types of degradation is given also. Detailed explanations

are given about the geometric degradation sources and effects. The effects of the geometric degradation were observed on the experimental results to be analyzed.

There are three types of image degradation: radiometric degradation, geometric degradation and noise. The mathematical relation between these degradations and an ideal camera response is at position (x,y) in the thermographic image (Maldague 2001):

$$I(x,y) = S[h(x,y) * T(x,y) + n(x,y)] \tag{4.1}$$

where I(x,y) represents the camera response at (x,y);

S[ ] represents the effect of radiometric degradation on ideal camera response at (x,y);

h (x,y), represents the effect of the geometric degradation on the camera response at (x,y);

*, the convolution operator, which is the integral of the two functions h (x,y) and T(x,y);

T(x,y), represents the ideal relation between the surface temperature and the camera response at (x,y); and

n(x,y) represents the effect of noise on the ideal camera at (x,y).

The radiometric degradation, also called the vignetting effect, is a reduction of the infrared radiation intensity at the edges of the image due to the limited lens aperture of the camera.

The noise is an unwanted signal in the system. There are two major kinds of noise:

1. the fixed noise has a distinct pattern that can be, for example, caused by sensitivity variations between detectors through the field of view and
2. the random noise is a signal whose value is independent of position and time.

Geometric degradation is discussed in more details in the next section.

4.3.1.1 Geometric degradation

Geometric degradation is mainly due to the diffraction phenomenon. Because of diffraction, the radiant energy from a point source is spread out at the location of the ideal image point (Williams 1972). For example, a radiant energy point source will produce a circular image due to diffraction. Figure 4.9 shows an irradiance distribution of a diffraction pattern for point source.

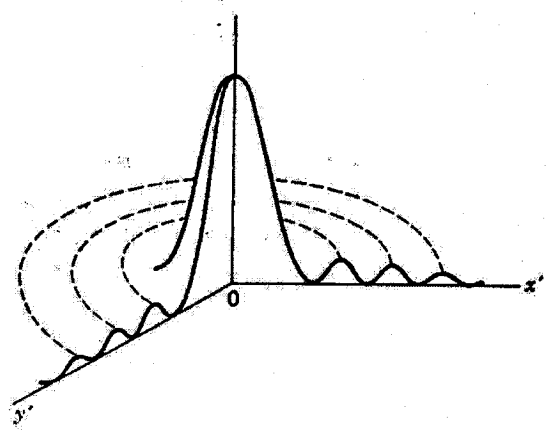

Figure 4.9 Irradiance distribution of a diffraction pattern (from Williams 1972)

The geometric degradation effects are observable on the thermogram when sharp temperature transitions are observed with the camera: a blurring effect is observable at edges in the thermogram.

In terms of camera performance, geometrical degradation of the thermographic data by the camera system has an effect on the slit response function of the camera as presented in section 2.4.2. The performance of the camera in regards to geometric degradation can be fundamentally described by the Modulation Transfer Function (MTF)

of the camera optical system. The MTF is the system magnitude response to sinusoids of different magnitude (ASNT 2005). The MTF can be assessed measuring the Point Spread Function of the system; the PSF is the camera output of a point source located in the field of view of the camera. The two-dimensional Fourier transform of this PSF is the MTF. The integration of the PSF parallel to a line source leads to the Line Spread Function. The LSF integration is equal to the Edge Spread Function, or the output of an edge target. The point spread function will be used in the following analysis when discussing of the geometric degradation effects of the camera system on the thermographic data.

The experimental thermographic data analyzed in the next two sections may have been affected by radiometric degradation and noise; however, only the effects of geometric degradation were observed and taken into account on the experimental data.

4.3.2 Assembly surface temperature distributions analysis

The assembly surface temperature distribution matrices to be analyzed have been extracted from the thermograms. They are adjusted according to the measurement parameters and corrected according to the reference emitter technique.

The final aim of the analysis of these data is the crack sizing. The crack shape was simple to allow the sizing of the crack in terms of width and length. The transversal, across the crack, and longitudinal, along the crack, temperature profiles (Figure 4.10) were used in the analysis instead of whole temperature matrices. Effectively, infrared thermograms are temperature maps from which temperature across one line can be extracted. In this thesis, such data is named temperature profiles.

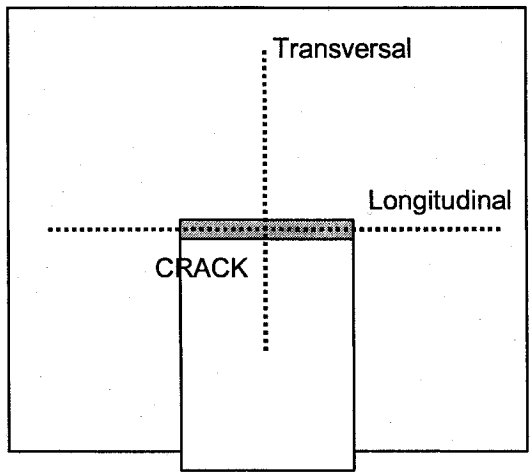

Figure 4.10 Face view of the panel with the crack showing crack longitudinal and transversal axes

In the following sections the profile general trends are first understood. The profiles and the temperatures at the crack location are compared and their relations with real crack dimensions studied. The profiles acquired under different conditions are compared and the relation between the temperatures measured at the crack location and the air temperature measured by a thermocouple are studied in relation with the measured crack dimensions.

4.3.2.1 Profiles Analysis

The analysis of the general trend of temperature profiles has led to the identification of three specific temperature zones in the profiles (Figure 4.11). First, there is the increase of panel surface temperature, outside the crack limits. That has been first associated to the possible recirculating air due the air jet of the leak. This recirculating air, assuming it is warmer than the ambient air, would transfer heat to the wall. However, according to the results obtained from the paper screen paper thermogram (Figure 4.8 b), there is no recirculation or this recirculation is at ambient temperature so the wall surface

temperature around the crack cannot be affected. The retained hypothesis is that heat is transferred mainly by conduction in the material from the air leak at the crack location.

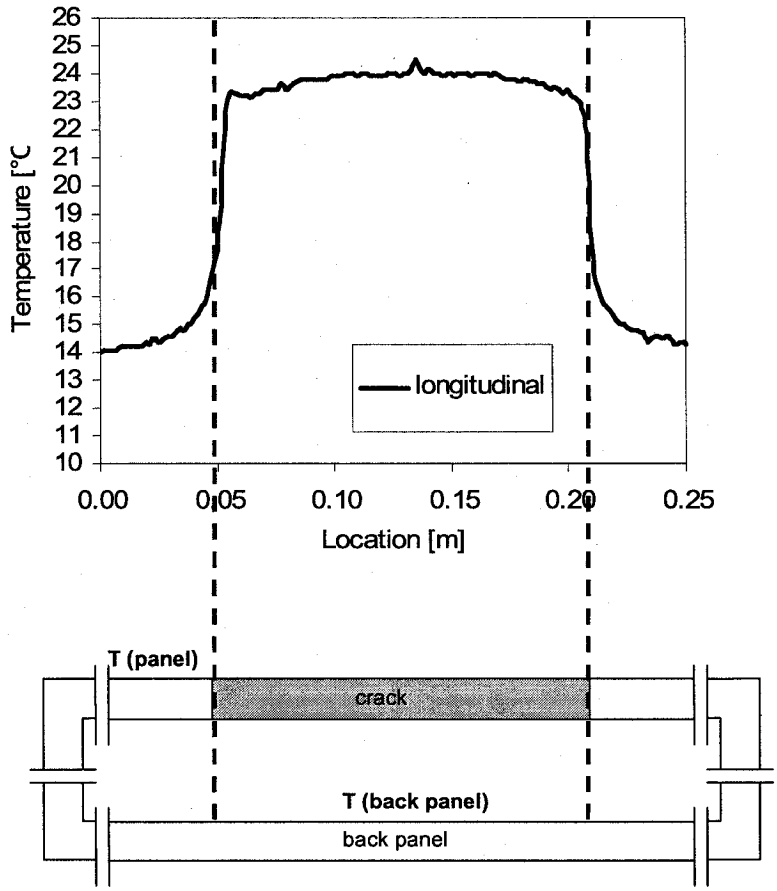

Figure 4.11 Longitudinal temperature profile and sealed box section showing corresponding front and back panel surface temperatures measured

The second zone, near the crack limit locations, is characterized by an abrupt increase of the surface temperature (Figure 4.11). This phenomenon is explained by the point spread function presented in section 4.3.1 that creates a blurring in the thermogram where there is an abrupt change in temperature.

Finally, inside the crack limits there is a temperature plateau that is the temperature at the back of the sealed box.

4.3.2.2 Temperature profiles and crack dimensions

From thermograms acquired under the different testing conditions, temperature profiles measured in the middle of the crack location along the lateral and longitudinal axes are plotted in Figure 4.12 to 4.15. This section looks at the relation between temperature profiles and crack dimensions.

First, temperature plateau sides and maximum temperature peaks are shifting in location from one to the others. For the temperature peaks, for example, Figure 4.12a) shows slight variations in maximum temperature locations; while for 4.13 a) and 4.14a) a distance of 5 to 6 centimeters in the location of maximum temperature is noticeable. The left temperature profiles sides of Figures 4.12b) and 4.14b) have almost all the same locations while the right sides are not together; the left sides of Figure 4.13b) do not correspond also. These shifts have been explained by the method used to retrieve locations of the thermograms temperature data. Markers have been used as references to assign location, in terms of x and y coordinates, to temperature data. These low emissivity markers are identifiable in the thermograms because of the reflected temperature that they mirror. However, the size of the markers used has been determined to allow their clear distinction with the plate temperature. The size of the markers used, 0.004 m X 0.004 m, is equal to 2 to 4 times the temperature data instantaneous field of view depending on the camera distance from the plate. Therefore, it could be anticipated that the assigned locations using the markers differ between the thermograms.

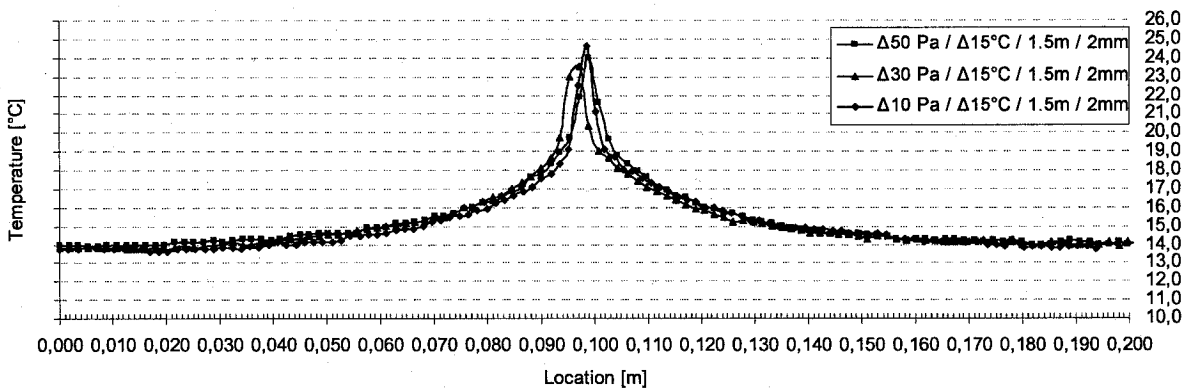

a)

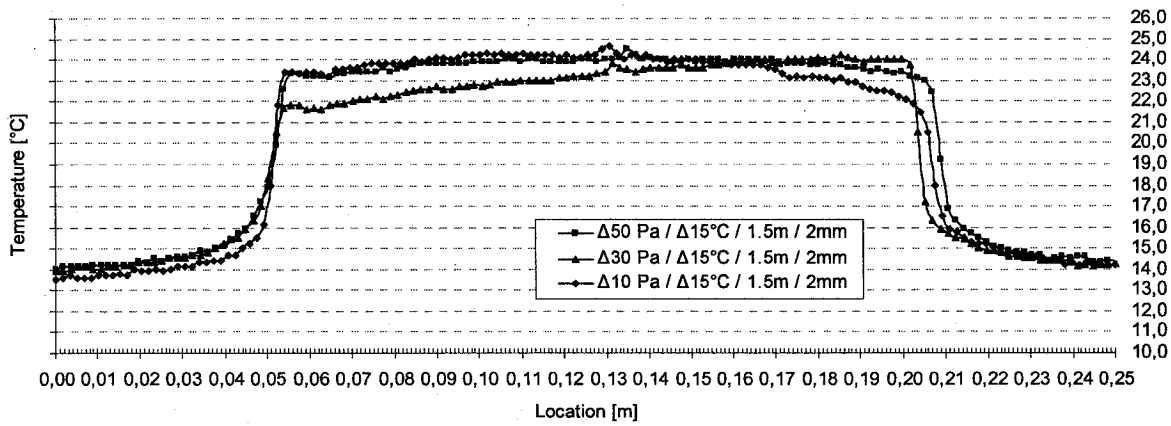

b)

Figure 4.12 Transversal (a) and longitudinal (b) temperature profiles from thermograms taken under 10, 30 and 50 Pa pressure differential

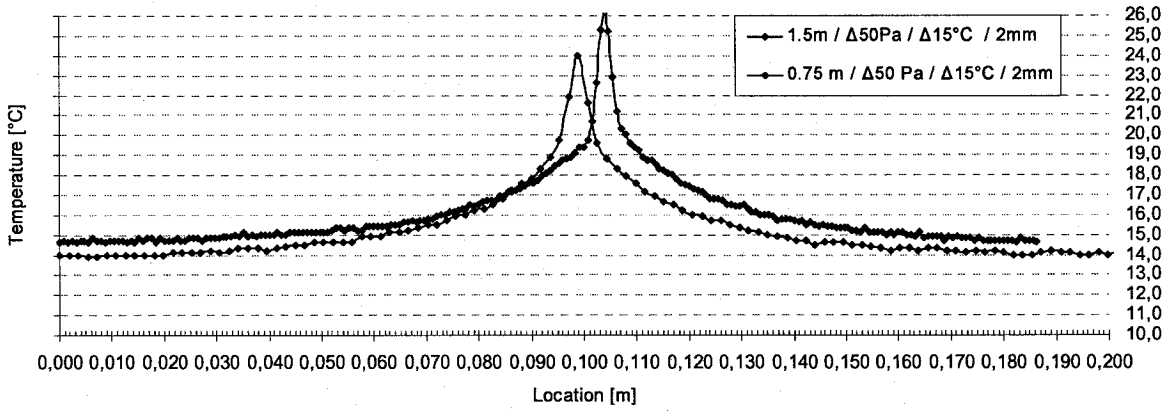

a)

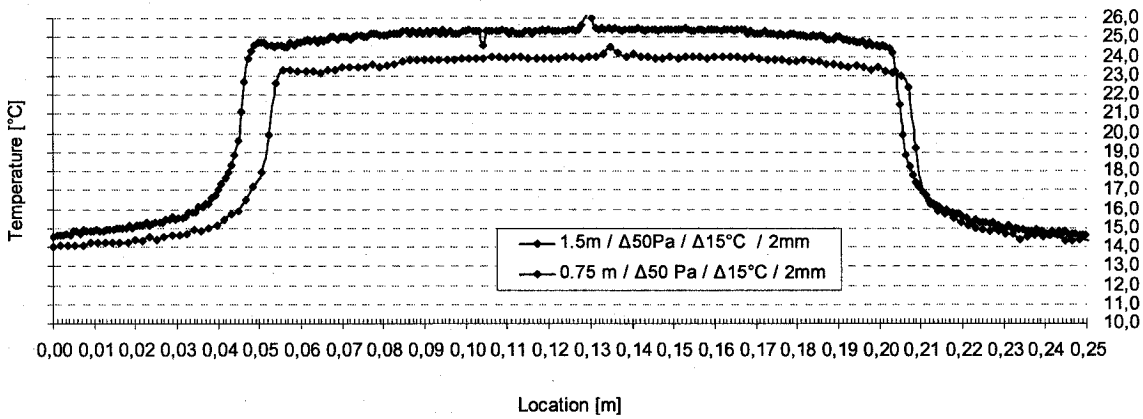

b)

Figure 4.13 Transversal (a) and longitudinal (b) temperature profiles from thermograms recorded under 0.75m and 1.5m distances

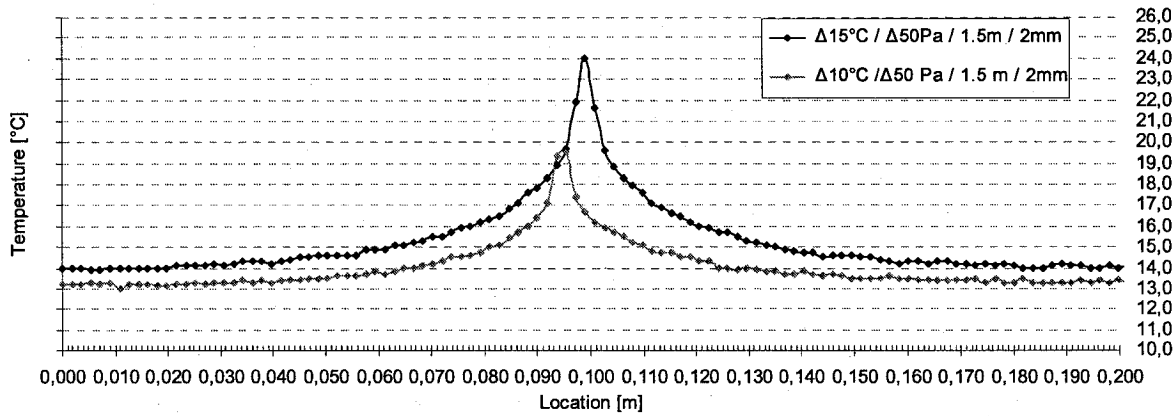

a)

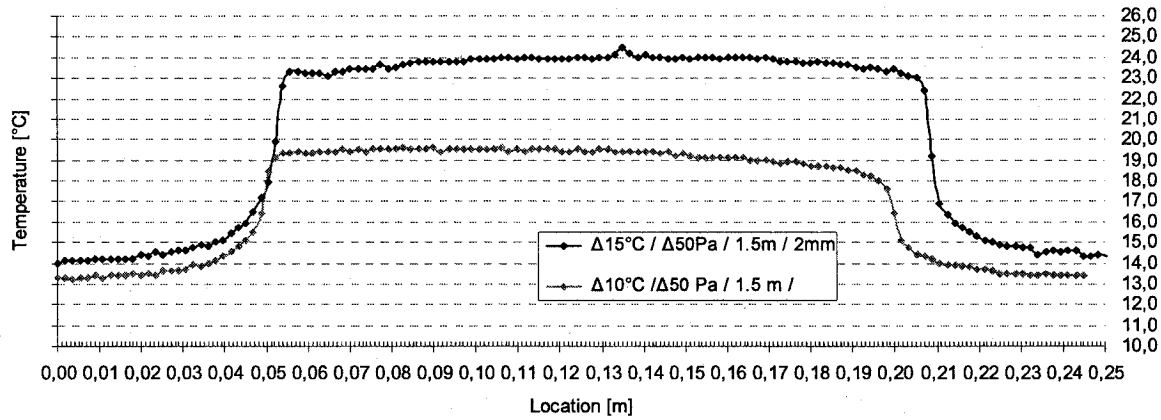

b)

Figure 4.14 Transversal (a) and longitudinal (b) temperature profiles from thermograms recorded using temperature 10°C and 15°C temperature between leaking air and ambient air in the chamber

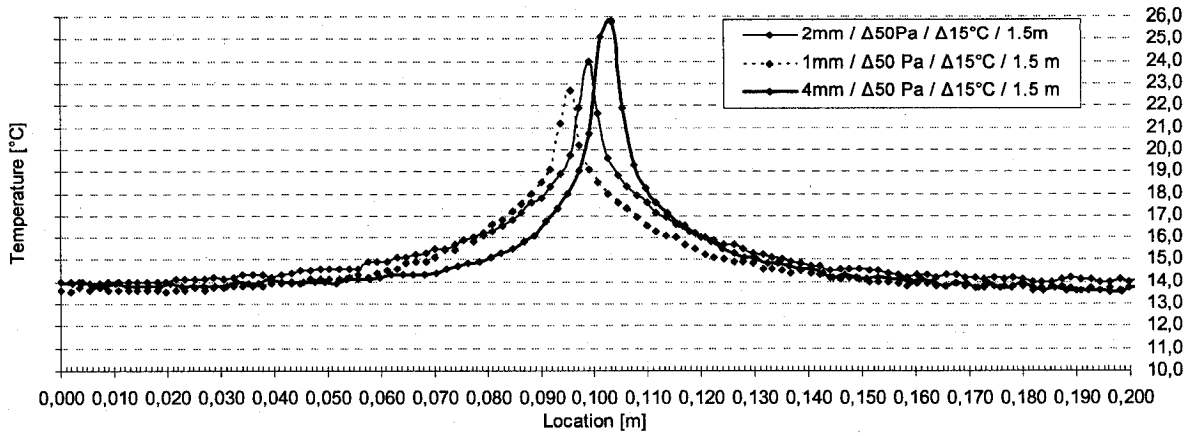

a)

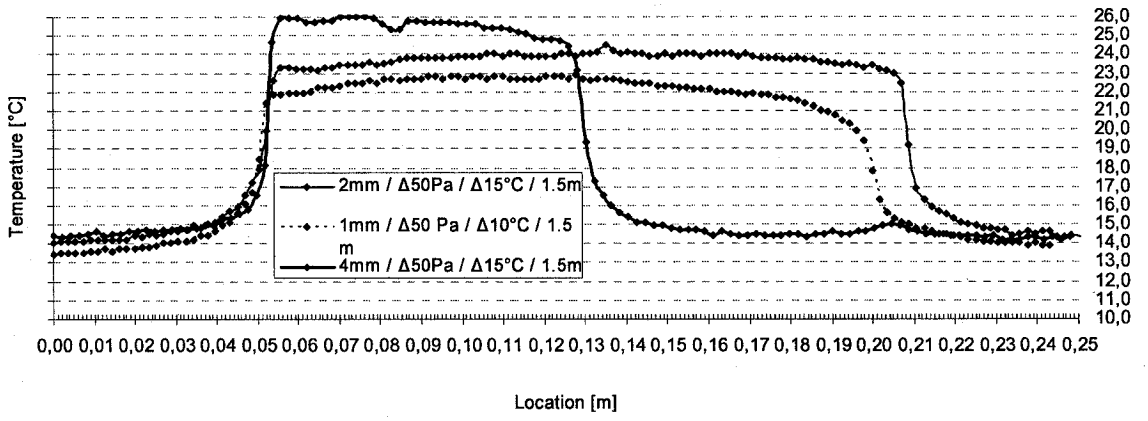

b)

Figure 4.15 Transversal (a) and longitudinal (b) temperature profiles from thermograms recorded using 1 mm, 2 mm, and 4 mm crack widths

In addition to location shifts, both peak widths and distances between plateau sides, and maximum temperatures vary between from one profile to another. For example, the lateral and longitudinal profiles for 1, 2, and 4mm cracks acquired under the same experimental conditions (Figures 4.15a) and b)) show apparent variations in peak widths and distances between plateau sides. The variations in maximum temperature

between the different profiles and their relations with crack dimensions are discussed in the next section of the thesis.

Finally, from the peak widths and distances between plateau sides of the lateral and longitudinal profiles, rough estimate of the crack dimensions can be obtained. However, the blurring at the crack limits do not permit precise sizing.

4.3.2.3 Temperatures at the crack location and crack dimensions

This section looks at the relationship between representativity of temperature measured with infrared thermography at the crack location versus the leaking air temperature in relation to the crack dimensions. The working assumption is that the temperature measured by the camera should be equal to the air temperature measured by the thermocouple installed at the crack location. This thermocouple measured the leaking air temperature. Therefore, this assumption was the basis of the following analysis. Strictly speaking, the temperature that should be measured by an ideal camera within the area of the crack is the surface temperature inside the box, as seen though the crack, (Figure 4.11) that is equal to the temperature of the leaking air measured by the thermocouple.

The averages of the temperatures measured at the crack location were computed for each thermogram acquired under the test conditions (Appendix J). Table 4.1 presents, in addition to averaged temperatures at the crack location, the temperature differences between the averaged temperatures measured at the crack location and the temperatures measured with the thermocouple installed at the crack location. The averaged temperatures and temperature differences under varied pressure differences have been

combined. According to the measurements, the temperatures at the crack location measured with infrared thermography do not vary with pressure difference. However, the opposite, i.e. that the pressure differential would impact the air temperature within the crack location, is expected in the case of complex assemblies as a result of the influence of the pressure difference on the heat transfer process along the path through the assembly.

Table 4.1 Temperatures differences between air leak temperatures measured with a thermocouple and averaged temperature at the crack location using thermography

Tests	Width [mm]	distance [m]	T TC [°C]	mean T IR [°C]	T [°C]
1/3/5	1	0.75	25.1	22.3	-2.9
2/4/6	1	1.5	25.2	21.8	-3.4
7/9/11	1	0.75	20.1	19.5	-0.6
8/10/12	1	1.5	20.1	18.7	-1.4
13/15/17	2	0.75	20.3	20.4	0.1
14/16/18	2	1.5	20.3	19.1	-1.2
19/21/23	2	0.75	25.3	24.9	-0.4
20/22/24	2	1.5	25.2	23.5	-1.7
25/27/29	4	0.75	20.0	20.5	0.5
26/28/30	4	1.5	20.0	19.7	-0.2
31/33/35	4	0.75	25.0	26.3	1.3
32/34/36	4	1.5	25.1	24.7	-0.3

In addition to the leaking air temperature, the distance and the crack width are two parameters that may theoretically influence the temperature to be measured within the crack opening area. In fact, an ideal camera system would measure the average temperature of the surface, i.e. a proportional average of the temperature inside the crack or back panel temperature and on the panel area in the instantaneous field of view area, as seen in Figure 4.16. Since in the case of this experiment, the crack width corresponded from half to 4 fields of view of a detector width, the temperature measured at the crack

location or the temperature of the back panel (Figure 4.11) changed with crack width (Figure 4.18). The temperature measured by the camera at the crack location was also function of the distance (Figure 4.17).

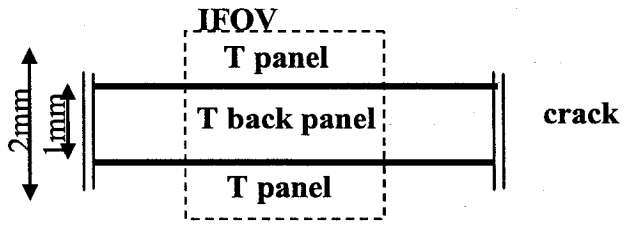

Figure 4.16 Portion of the crack area within the area of a detector field of view for a 1mm crack width and a detector field of view of 2mm at a distance of 1.50 m

First, on the effect of distance, the graph of temperature differences between average temperature and temperature measured at the crack location against distance (Figure 4.17) shows that the distance has a significant impact on the difference magnitude. Almost all the differences of temperature at 1.5m are negative while the differences of temperature at 0.75m vary from -3.4°C to 2°C.

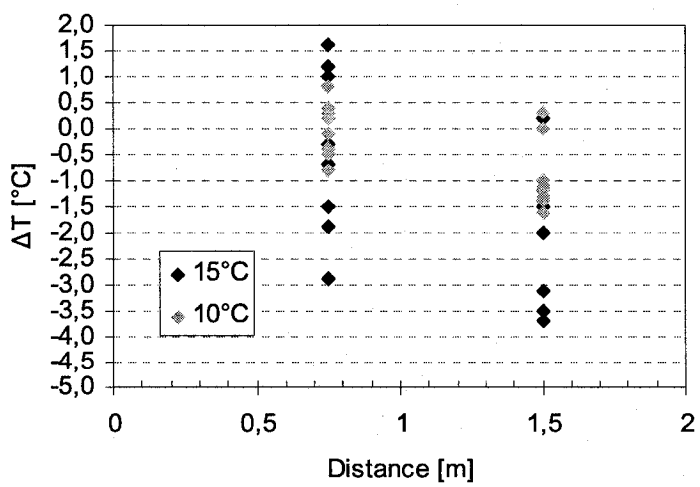

Figure 4.17 Differences between the air temperature measured with infrared camera and the leaking air temperature measured with a thermocouple in relation to the distance

Second, on the effect of crack width, the temperature differences that are plotted in Figure 4.18 show the relationships between crack dimensions and temperature difference separately for each of the distance. The regression lines highlight that the temperature difference increases with the crack width for both distances but that the increase is more important in the case of a distance of 0.75m between the camera and the panel.

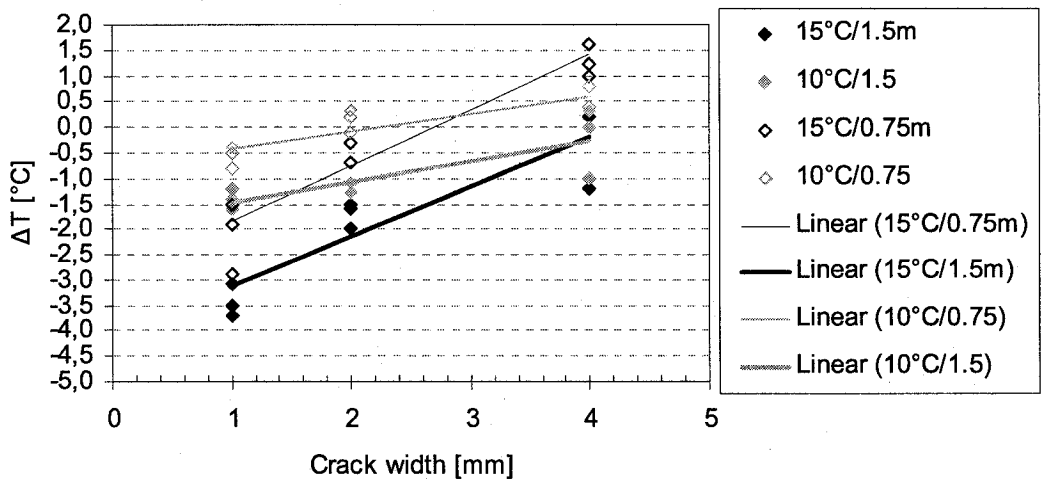

Figure 4.18 Differences between the air temperature measured with infrared camera and the leaking air temperature measured with a thermocouple in relation to the crack width

Also, the camera and the panel were positioned such that the camera's view was perpendicular to the crack. However, the relative position of the crack opening and the instantaneous field of views, due to the non perpendicular position of the camera view and the crack opening, has an effect that can be noticed looking at the maximum temperature variation along almost all longitudinal temperature profile (Figures 4.12 b,

4.13 b, 4.14 b, and 4.15 b). The standard deviation of the maximum temperature computed from the averaged maximum temperature (Appendix J) was used to give an idea of the magnitude of the influence of the crack position: the standard deviation reached 1.9°C for 1.5m of distance looking at 1mm crack with air temperature close to 25°C.

Finally, general relationships can be established between temperatures measured at the crack location and crack width taking into account the distance; however, stronger correlations are required to estimate crack dimensions.

Error on absolute temperature measurements

For this experiment, no surface temperature was measured with a contact sensor, e.g. a thermocouple, to measure the error on temperature measurement using infrared thermography and the reference emitter technique. However, the difference between the temperature measured at the crack location and the air leak temperature measured with the thermocouple can be compared with the calculated error on absolute temperature measurement calculated above to evaluate whether this error is realistic.

The comparison of the temperature measured at the crack location within the crack opening with the theoretical temperature calculated using averaged radiance cannot be performed here since the panel temperature around the crack limit was not known and non uniform. The point spread function on the thermographic data has an effect on the measured temperature of sharp temperature transition patterns also.

Generally, the temperatures measured at the crack location were lower than the temperature measured by the thermocouple due to the small crack width compared to the

instantaneous field of view. However, the temperature difference was positive for the 4 mm width cracks with the camera installed at 0.75m. The temperature difference exceeded 1.5°C at distance of 0.75m and crack of 4mm with air temperature close to 25°C. This difference was superior to the combination, equivalent to 1.1°C; of the calculated temperature measurement uncertainty calculated using a reference emitter (0.6°C) (Section 3.5.3) and the thermocouple uncertainty (0.5°C).

Two explanations are possible for the difference between calculated and measured error on absolute temperature measurement. On one hand, the correction using the reference emitter may not have been precise enough because of the use of the thermocouple for the surface temperature measurement. The use of a RTD for the calculation of the surface temperature may have been more appropriate. On the other hand, analyzing the error for the measurement of absolute temperature using thermography for the actual experiment, many assumptions have been made. These assumptions could have minimized the error value.

4.3.2.4 Conclusion of the quantitative analysis

It was shown by the quantitative analysis that temperature profiles are in fact influenced by the crack dimensions. However, temperature profiles show a gradual increase of temperature at the limits of the cracks and thus cannot be directly used to precisely determine crack dimensions. It was shown also that there are relations between the temperatures measured at the crack location and leaking air temperature. However, more effective relations must be established for crack dimensions estimation.

4.4 Crack sizing

A first initiative for crack sizing was to develop a technique to limit the section of the profiles that belongs directly to the crack opening so that dimensions can be measured. Second, relationships between temperature profile sections that belong to the crack and real crack dimensions was analyzed so that a calibration method could be established.

4.4.1 Profiles segmentation

Segmentation techniques were tested on their effectiveness in crack sizing by the segmentation of the sections of the temperature profiles that belong directly to the crack opening. Segmentation techniques are used to identify and locate automatically defects in thermograms. These techniques are based on a variety of algorithms such as histogram analysis and edges detection. The first purpose of these techniques is to segment the image and isolate regions of interest (ASNT 2005). Also, the analysis of these regions provides defect gross shape and approximate dimensions of the defects. Two of the segmentation techniques were applied and tested for their appropriateness in identifying the sections of the temperature profiles that belong directly to the crack opening.

The histogram technique consists of valleys detection in thermogram histograms, where histograms are a statistic representation of temperature data in the thermograms. The valleys are then used for thresholding where large continuous temperature sections are isolated between sharp temperature increase limits. This method was found to be

inappropriate and the probable reason is the presence of the exponential temperature increase outside the limits of the crack (Figure 4.11) and the magnitude of the crack areas to be detected. As a result, the profiles histograms did not show any apparent valleys so that no temperature sections could be isolated (Figure 4.19).

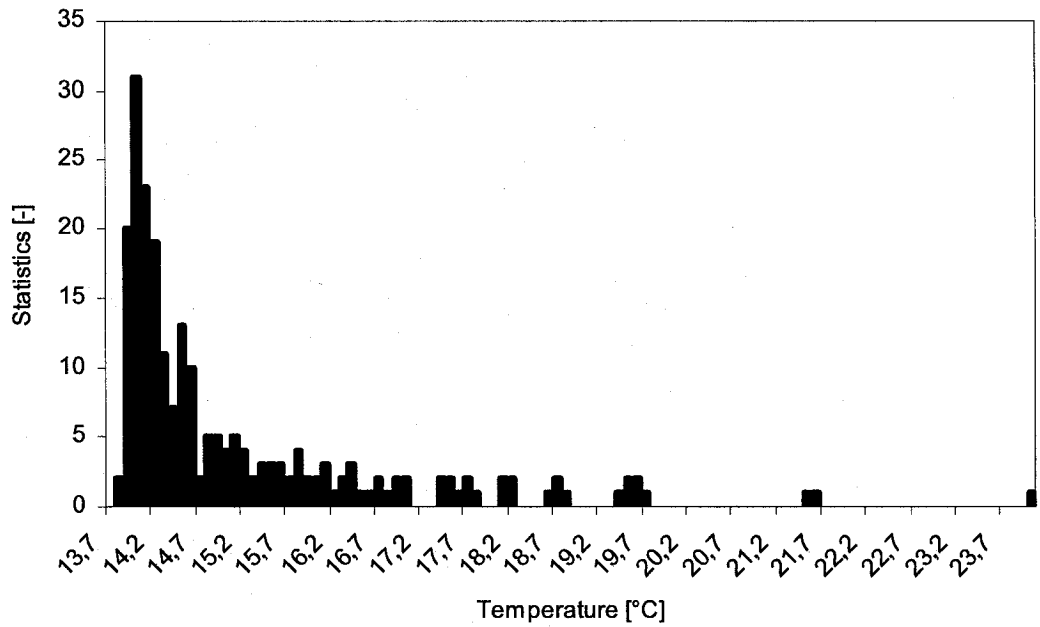

Figure 4.19 Histogram showing the temperature data statistics of a transversal temperature profile

The other segmentation technique used uses the edge detection. The edge detection for image segmentation consists of locating edges based on abrupt changes in intensity in the image. The basic idea in edge detection is the computation of local derivative operators (Gonzalez 1992) that lead to peak values where there are edges. Figure 4.20 illustrates an image where edges in profiles are blurred. The first derivative of the intensity profile shows peak and zero crossing at actual edge locations.

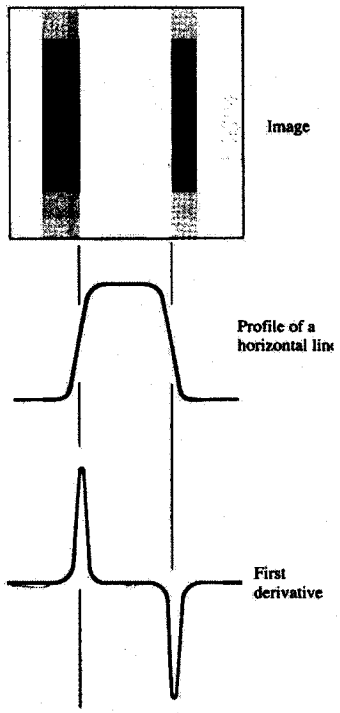

Figure 4.20 Image segmentation principle (from Gonzalez 1992)

The gradient operator is used to differentiate any point (x,y) in the image:

$$\nabla f = \begin{bmatrix} Gx \\ Gy \end{bmatrix} = \begin{bmatrix} \frac{\partial f}{\partial x} \\ \frac{\partial f}{\partial y} \end{bmatrix} \tag{4.2}$$

where ∇ f is for a function f(x,y), the gradient of f at coordinates (x,y);

G_x and G_y, are the gradients of the function f relative to x and y.

The magnitude of the vector rather than the direction being of interest for edge detection, the gradient calculation is simplified:

$$\nabla f = mag(\nabla f) = \left[G_x^{\,2} + G_y^{\,2}\right]^{1/2} \tag{4.3}$$

where G_x and G_y, are the gradients of the function f relative to x and y.

More simplifications have been reported (Fu and Mui 1980), and the gradient magnitude can be calculated with:

$$G(x,y)=\left(f(x,y)-f(x+1,y+1)\right)^2+\left(f(x+1,y)-f(x,y+1)\right)^2 \quad (4.4)$$

where G, is the gradient of the function f at (x,y).

Based on this method, a simplified method was developed for the segmentation of temperature profiles to isolate the section that belongs to the crack, hence allowing the determination of the crack dimensions.

4.4.1.1 Method proposed

Since, in the actual experiment, transversal and longitudinal temperature profiles were analyzed separately, the model was simplified by computing only the magnitude of the one-dimensional gradient:

$$g(x)=T(x+1)-T(x-1) \text{ and} \quad (4.5)$$

$$g(y)=T(y+1)-T(y-1) \quad (4.6)$$

for longitudinal and transversal profiles respectively.

With further simplifications, the differences between each pixel were computed with:

$$g(x)=T(x+1)-T(x) \quad (4.7)$$

$$g(y)=T(y+1)-T(y) \quad (4.8)$$

for longitudinal and transversal profiles respectively.

The gradients calculated between each data, using equations 4.7 and 4.8, led to more precise estimations of the crack dimensions than the ones using equation 4.5 and 4.6. Therefore, the former were used for the estimation of the segmentation process.

The computed differences between data were plotted so that dimensions could be graphically measured. Figure 4.21 presents in a) the horizontal temperature profile and in b) the temperature gradient computed using equations 4.7 and 4.8. The graphical measurement of the length is presented.

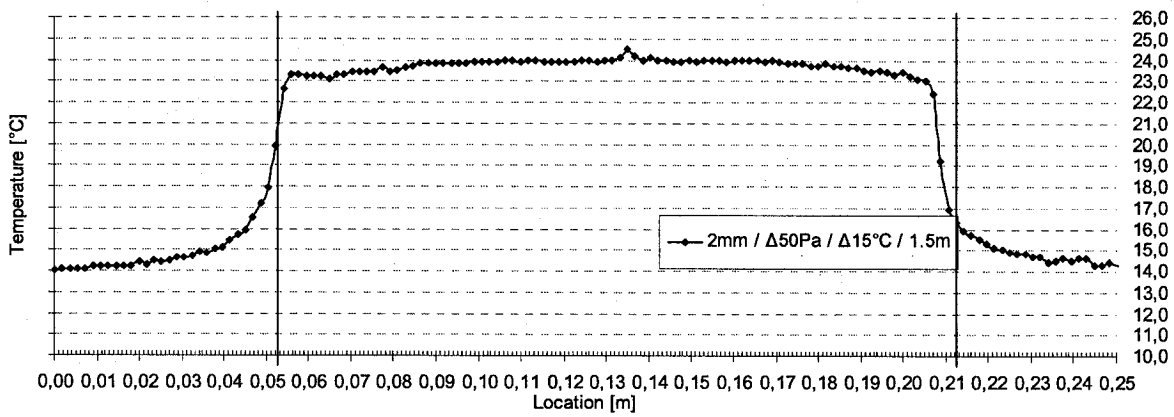

a)

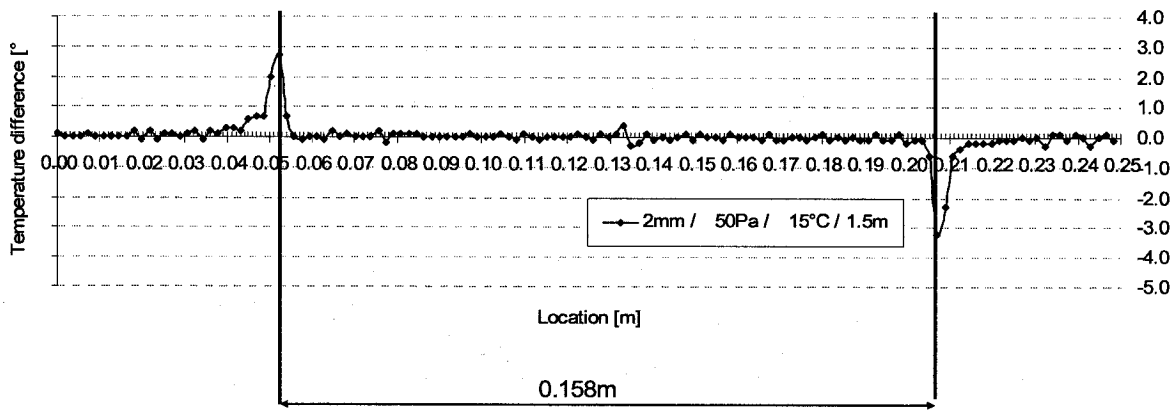

b)

Figure 4.21 Longitudinal temperature profile (a) and corresponding temperature gradient (b) used for graphical estimation of the crack dimensions

4.4.1.2 Estimated dimensions

The crack dimensions estimated from each thermogram applying the segmentation technique to the temperature profile located at the center of the crack opening to estimate the dimensions are presented in Appendix K. The estimated dimensions of the cracks presented in Table 4.2 are averaged over the varied pressure and temperature differences used in the experiment. This approach was possible since only the distance between the camera and the crack panel has a significant influence on the results. This issue is discussed in the section on the influence of conditions on estimated dimensions that follows.

Table 4.2 Widths and lengths estimated using segmentation technique

Tests	width [m]	distance [m]	dT [°C]	dP [Pa]	estimated [m]	σ [m]	[m]	[%]
1/3/5/7/9/11	0.001	1.50	10, 15	10, 30, 50	0.0020	0.0000	0.0010	100
2/4/6/8/10/12	0.001	0.75	10, 15	10, 30, 50	0.0026	0.0005	0.0016	161
13/15/17/19/21/23	0.002	1.50	10, 15	10, 30, 50	0.0030	0.0000	0.0010	50
14/16/18/20/22/24	0.002	0.75	10, 15	10, 30, 50	0.0037	0.0004	0.0017	83
25/27/29/31/33/35	0.004	1.50	10, 15	10, 30, 50	0.0043	0.0005	0.0003	8
26/28/30/32/34/36	0.004	0.75	10, 15	10, 30, 50	0.0043	0.0005	0.0003	8

Tests	length (m)	distance [m]	dT [°C]	dP [Pa]	estimated [m]	σ [m]	[m]	[%]
1/3/5/7/9/11	0.150	1.50	10, 15	10, 30, 50	0.1571	0.0037	0.0071	5
2/4/6/8/10/12	0.150	0.75	10, 15	10, 30, 50	0.1513	0.0027	0.0013	1
13/15/17/19/21/23	0.150	1.50	10, 15	10, 30, 50	0.1580	0.0037	0.0080	5
14/16/18/20/22/24	0.150	0.75	10, 15	10, 30, 50	0.1531	0.0022	0.0031	2
25/27/29/31/33/35	0.075	1.50	10, 15	10, 30, 50	0.0770	0.0009	0.0020	3
26/28/30/32/34/36	0.075	0.75	10, 15	10, 30, 50	0.0748	0.0024	-0.0002	0

Table 4.2 shows that the difference between estimated and measured widths for 1 and 2 mm width for the two distances are of the same magnitude. In one case of a crack of 1mm at 0.75m the difference is equivalent to 161% while in one other case of a 2 mm crack at 1.5 m the difference is equal to 50%.

The average difference for a 4mm crack width is 8%, which is acceptable, and the distance has no effect on the difference magnitude between estimated and measured widths for 4mm crack width.

For the length estimation, the trend observed on the difference between the estimated and measured length is also related to distance: estimated lengths from thermograms acquired at 0.75m distance show smaller differences with measured lengths that estimated lengths from thermograms acquired at 1.5mm distance (Table 4.2). The location markers are probably the major source of the differences on the estimation of lengths. As it has been explained in section 3.1.3, location markers were used to retrieve the locations of the temperature data and the use of these markers clearly led to difference in crack locations. Therefore, it is probable that the use of these markers as references for location assignment to temperature data could lead also to the differences between estimated and measured length. This difference, which is less than 5%, is however acceptable for 0.075m and 0.150m length. Therefore, the distance being acceptably measured using the segmentation method, the rest of the analysis focused on improving the crack sizing for the crack widths.

For length, and the 4mm width, estimation by the method was found to be efficient; however, for the 1 and 2 mm widths estimations, the method needed to be improved. The study of the effects of the conditions on the estimated widths follows in the next section focusing on the estimation of small widths.

Conditions influence on the estimated widths

To assess the influence of the conditions on the estimated width, all the estimated dimensions have been first plotted (Figure 4.22 and Annex L) against each of the conditions: distance, temperature differences, and pressure differences. Figure 4.22 presents the estimated width of a real 1mm crack. The pressure differences and temperature differences do not influence the estimated crack widths. The difference between the estimated and the real dimensions increases with the distance; one exception is the case of a 4 mm crack width.

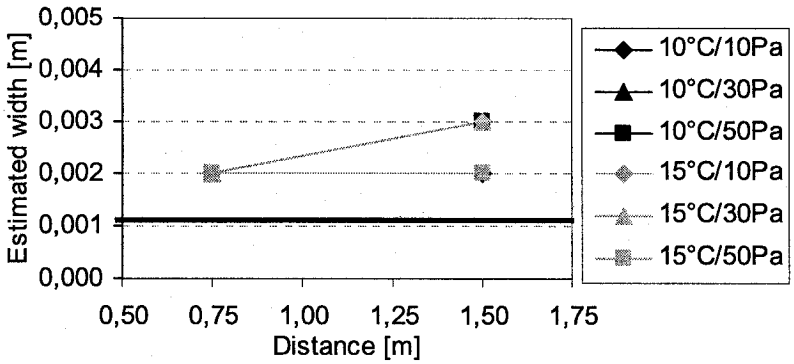

a)

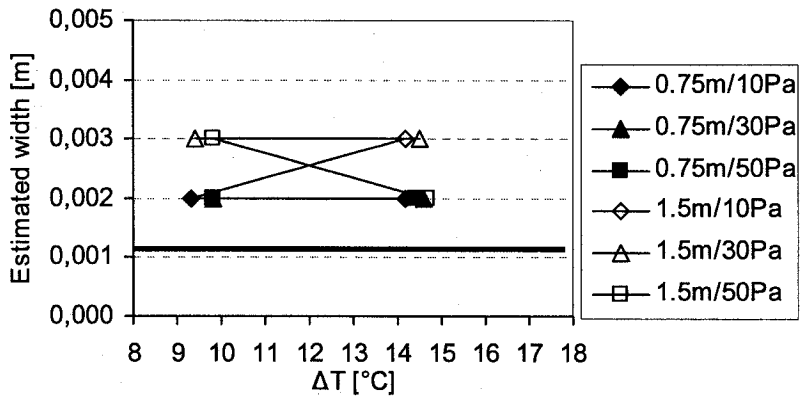

b)

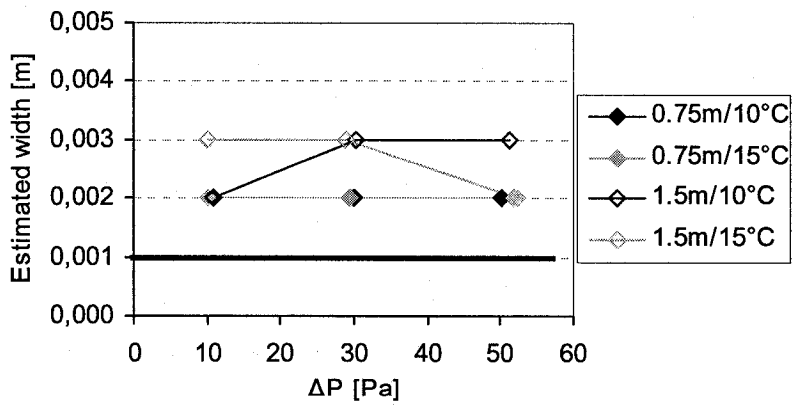

c)

Figure 4.22 Estimated widths against distance (a) temperature difference (b) and pressure difference (c) for a 4mm width crack

A statistical test (t-test) was used then to verify the influence of the distance on the estimated width that was highlighted graphically (Figure 4.22). The statistical test on two means verifies the hypothesis of the difference between the mean of two samples. If the statistical index t, calculated as follows, is greater than the critical value (Walpole 1989), the difference between the two means is significant:

$$t = \frac{(\mu_1 - \mu_2)}{\sqrt{(\sigma_1^2 / n_1) + (\sigma_2^2 / n_2)}} \tag{4.9}$$

where σ_1 and σ_2 are the standard deviations of the two samples [m];

μ_1 and μ_2, the means of the two samples [m]; and

n_1 and n_2, the sample sizes.

The critical t value is selected by assuming α= 0.05 (confidence interval), and a v=n-1 (degree of freedom).

This test was used to verify if the width estimated at 1.5 and 0.75 m distances were effectively different. The t value computed for the different estimated widths are presented in Table 4.3 with the mean and standard deviations of the samples.

Table 4.3 Tests on two means t-values for crack widths estimated with segmentation technique method comparing the widths estimated at 0.75 and 1.5m

	Calculated			Reference		
	mean at 1.5m	mean at 0.75m	t	critical t	α	v
1mm	0.0026	0.0020	2.995	2.015	0.05	10
2mm	0.0030	0.0037	4.287	2.015	0.05	10
4mm	0.0043	0.0043	0.000	2.015	0.05	10

The calculated t-value is higher than the tabulated critical t-value for 1 and 2mm widths but not for the 4mm widths (Table 4.3). Therefore it can be stated that the

estimated width is effectively influenced by the distance in the case of 1 and 2 mm crack widths, but not for 4mm crack widths.

Variation of the estimated width versus the crack length

The width estimated could vary also depending on the position of selected transverse temperature profile along the longitudinal axis of the crack. To verify the influence of the profile position on the estimated width, 20 profiles were extracted of the same thermogram but at different locations through the length of the crack and widths were estimated using the segmentation technique. In order to avoid the border effect, the profiles used for the analysis were centered relatively to the crack length. The standards deviations between the widths estimated from the profiles of the same thermogram are presented in Table 4.4. This computation was done for 2 widths at 0.75 and 1.5 m distances.

Table 4.4 Estimated widths standard deviations using different profiles throughout the crack length

Tests	width	dT	dP	estimated	σ
	[m]	[°C]	[Pa]	[m]	[m]
13	0.002	10, 15	10, 30, 50	0.0030	0.0005
14	0.002	10, 15	10, 30, 50	0.0037	0.0005

The standard deviations of the Table 4.4 are of the same magnitude than the standard deviations calculated between the profiles coming from different thermograms (Table 4.2).

4.4.1.3 Correlation-based model

Because of the magnitude of the difference between estimated and measured width obtained from the estimation of the 1 and 2 mm crack widths, the possibility of

developing a correlation between the estimated and measured crack widths in relation to the conditions parameters have been studied. Several correlation-based models have been considered (Table 4.5). For instance, in the following model:

$$w_m = (a \cdot \Delta P + b \cdot \Delta T + c \cdot D) \cdot w_e \quad (4.10)$$

w_m and w_e are respectively the measured and estimated crack width [m];

a, b, and c, fitted parameters;

ΔP, the pressure difference [Pa];

ΔT, the temperature difference [°C]; and

D, the distance [m].

Table 4.5 Correlation-based model tested and correlation strengths

REGRESSION	R-squared [%]
w=(a*dP+b*dT+c*D)we	12.85
w=(a*dP+b*D)we	(-47.49)
w=(a*dT+b*D)we	5.85
w=(c*D)we	(-91.69)
w=a*dP+b*dT+c*D+we	76.49
w=a*dT+b*D+we	60.01
w=a*dP+b*D+we	67.08
w=b*D+we	60.00
w=a*dP+b*dT+c*D+d*we	97.60
w=a*dP+b*D+d*we	97.59
w=a*dT+b*D+d*we	97.54
w=b*D+d*we	**97.54**
w=a*dP+b*dT+c*D+d*we+e	79.64
w=a*PT+b*D+d*we+e	76.64
w=a*dT+b*D+d*we+e	78.98
w=b*D+d*we+e	76.12

All the estimated widths and measured widths for the 1 and 2 mm cracks were used for the correlations finding, or the all measured and estimated width of the tests 1 to 24. The STATGRAPHICS (version Plus 5.0) software was used for identification of the parameters a, b, and c. The software uses the multilinear least squares method.

In table 4.5, the coefficient of correlation for each model is also presented. The multilinear regression without constant is the regression that shows the highest correlation value, 97.60%. The R-squared value does not change much whether or not the pressure and temperature parameters are included. The appropriate regression between the measured width and the estimated width is then:

$$w = -0.000650602 * D + 0.771084 * we \quad (4.9)$$

where D is the distance (m); and

w_e, the estimated width (m).

The distance is effectively the parameter that influences the relation between estimated and measured crack widths (Figure 4.22).

Figure 4.23 shows the relation between the measured widths and the predicted widths using the estimated widths in the established regression. The plot includes a line with a slope equal to 1 where all the points could be if the prediction would be perfect.

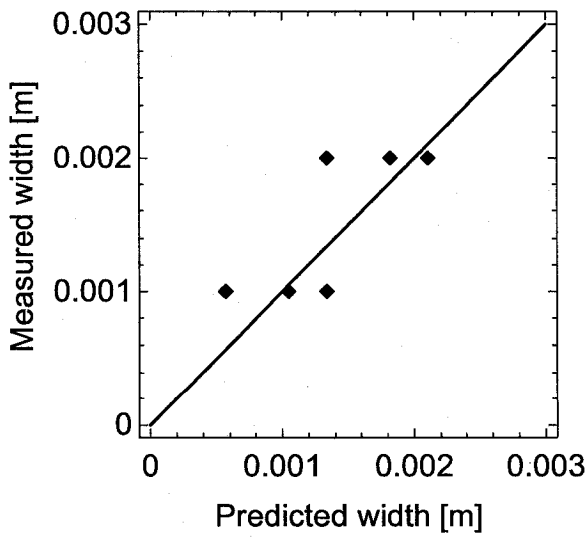

Figure 4.23 Predicted and corresponding measured widths using correlation-based model

Using the estimated width obtained with the segmentation technique and the correlation established (eq. 4.9), a 1 mm crack could be estimated to be 0.5 to 1.5 mm width and a 2mm crack could be estimated to be 1.5 to 2.5 mm width.

4.4.1.4 Conclusions from the use of segmentation technique for crack sizing

The estimation of the crack dimensions can be obtained from the gradients of the transversal and longitudinal temperature profiles selected in thermograms of surface temperature distribution due to air leaks. The dimensions are estimated graphically. The method succeed in measuring the length crack within a 5% error. The estimations are acceptable for length and for crack width of 4 mm. For smallest crack widths, regression curves have been developed including in the relationships the distance between the crack and the camera. The possibilities of a more accurate crack widths estimation method was looked at from defects sizing using a method based on tomography, as presented next.

4.4.2 Profiles calibration

The segmentation techniques have not been developed for precise and accurate defect sizing but for defect detection. To develop a method for precise and accurate building envelope crack sizing using infrared thermography, methods specifically developed for precise and accurate defects sizing were investigated.

The method tested is based on a tomography technique. Tomography is a method used in conjunction with infrared and X-ray cameras. X-ray computed tomography, as a defect sizing technique, is a well established technique used to find surface and inner

defects in materials (Vandersteen 2003). Tomography using infrared thermography, or thermal tomography, is used also to find materials defects in material (Ludwig 2002).

This defect sizing technique requires, first, the computation of the different contrasts values (Figure 4.25). Contrast values, that are computed using a camera response that belongs to a defect, are used to compare the magnitude of the camera response over a defect with a mean camera response, i.e. where there is no defect, in the thermogram.

In section 4.1, the geometric degradation and the mathematical relation between the degradation and the ideal camera response, a convolution, have been introduced. It has been explained that the camera response is equal to the combination of ideal camera response and the point spread function of the system. Since the point spread function is commonly described by a Gaussian function, the curve to be fitted to the camera response defect profile for the computation of the thermal contrast values is associated with an approximate Gaussian function as shown in Figure 4.24.

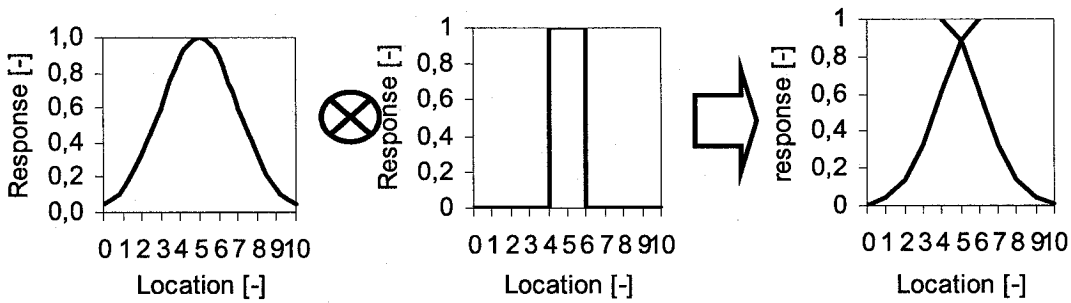

a) b)

Figure 4.24 Convolution of the Gaussian point spread function (a) and a data step function (b) (derived from Vandersteen 2003)

Different computed contrast values, such as peak height (PH), full width at mid height (FWMH), and missing attenuation (MA) are represented in Figure 4.25.

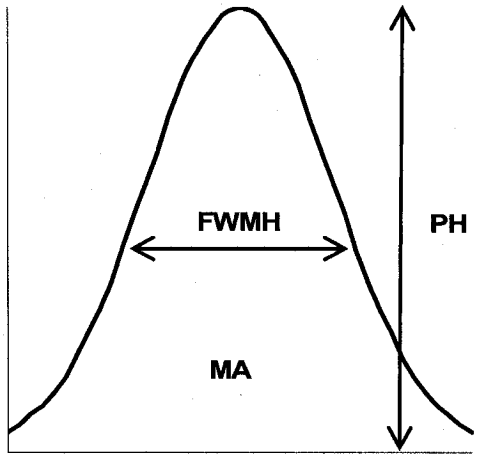

Figure 4.25 Contrast values: Peak Height (PH), Missing Attenuation (MA) and Full Width at Mid Height (FWMH) (derived from Vandersteen 2003)

Since the profiles trends vary with the defect size (Figure 4.24), the values of the contrast values vary also. Then, calibration relationships can be established between contrast values and real crack width.

Using X-Ray computed microtomography, surface defect sizing was studied by Vandersteen *et al* (2003). They established calibration relationships between defects thermal contrast values and real defect dimensions at the surface of crinoidal limestone. Values of the defects thermal contrast have been calculated using the following function for the curve fitting of the data over the defect:

$$Y = PH \exp\left[-\frac{1}{2}\left(\frac{X - x_p}{\Delta x_p}\right)^2 + \mu_{hr}\right] \tag{4.10}$$

where Y and X are respectively the X-ray data value and the data position;

PH is the peak height to be fitted;

x_p, is associated with the central position ;

Δx_p, a peak width rough approximation; and

μ, the mean attenuation.

MA was calculated with:

$$MA = \sqrt{2\pi * PH * \Delta x_p} \tag{4.11}$$

Calibration curves were established using peak height (PH) and missing attenuation (MA) to compare their effectiveness. Missing attenuation (MA), which takes into account the whole fitted function shape, was found a better contrast value to be used for calibration relationship establishment (Vandersteen 2003).

4.4.2.1 Method proposed

The tomography method presented before was tested for crack width sizing using air leak temperature profiles. In this study, two major specific drawbacks were anticipated with respect to the curve fitting procedure:

1. The surface temperature around the crack location is not constant (Figure 4.11) so that the section of the temperature profiles to be fitted to a curve , i.e. the sections of the temperature profiles that belong to the crack and that are affected by the geometric degradation, cannot be easily isolated; and

2. The temperature data, which are computed using the camera calibration curve are not, the ideal data for the curve fitting. Raw camera output data, which are response to the total radiance, are expected to produce better results since the camera calibration curve (eq. 2.23) is not linear with the temperature.

Nevertheless, the transversal temperature profiles were fitted with an approximate Gaussian function to establish the calibration relationships with measured crack width.

Also, the section width of the temperature profiles to be used for the curve fitting is theoretically related to the distance and the crack width (Figure 4.24). However, a fixed segment width was used for each of the two testing distances. The segment width to be used for the curve fitting was fixed to 6mm, equivalent to a fitting to 7 temperature data of the temperature profiles, for thermograms recorded at 0.75m distance and 8mm, equivalent to a fitting to 5 temperature data, for profiles from thermograms recorded at 1.5m distance. These segment widths of temperature data allowed the curve fitting of the data with an approximate Gaussian function (Figure 4.26).

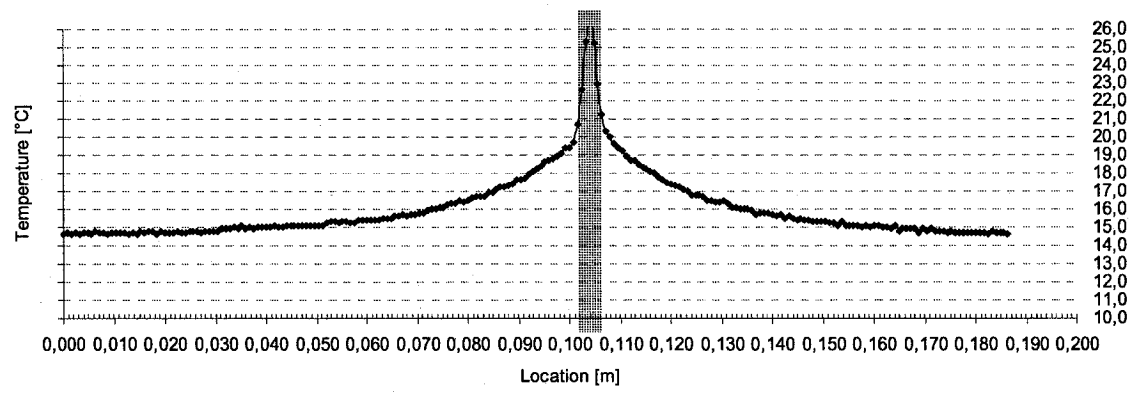

a)

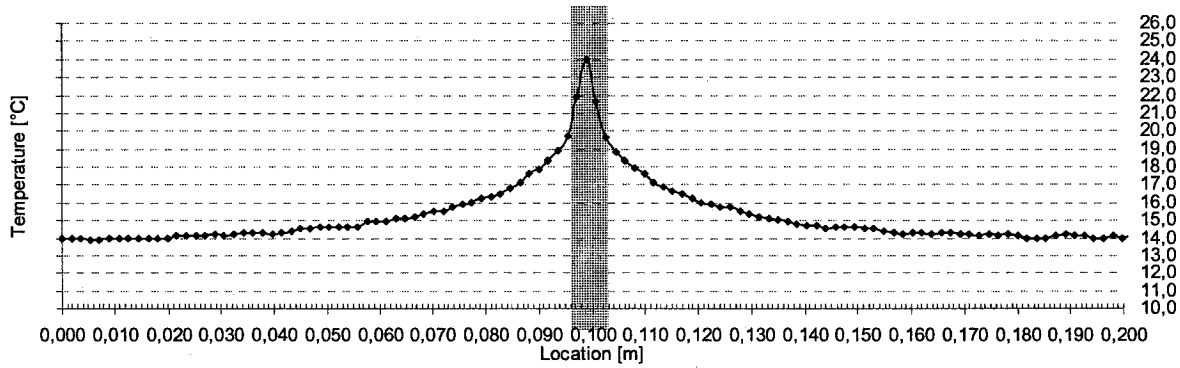

b)

Figure 4.26 Transversal temperature profiles recorded at 0.75m (a) and 1.5m (b) and segments of the profiles used for the curve fitting

Before the fitting, the each temperature data was normalized for the air and surface temperature with:

$$T_N = \frac{T_{IR} - T_p}{T_{TC} - T_p} \tag{4.12}$$

where T_N is the normalized temperature;

T_{IR}, the temperature measured;

T_p, the minimum temperature of the data to be used for the curve fitting [°C] that was assumed to be the panel surface temperature; and

T_{TC}, the air temperature measured by the thermocouple at the crack location [°C].

For each thermogram, 10 lateral temperature profiles were fitted to the following function:

$$Y = a \cdot \exp\left[-\frac{1}{2}\left(\frac{X-b}{c}\right)^2\right] \tag{4.13}$$

where Y is the normalized temperature;

X, the longitudinal position; and

a, b, and c; the parameters to be fitted.

Peak Height (PH) and Missing Attenuation (MA) values were computed for each fitting. PH was equal to parameter a of the fitted function. MA was computed with the following formula:

$$MA = \sqrt{2\pi \cdot a \cdot c} \tag{4.14}$$

where a and c are the parameters from the fitted function.

The contrast values PH and MA were used to establish calibration curves for crack dimensions. The results are presented in the following sections.

4.4.2.2 Contrast values computed

Using the determined sections of data temperature profiles, the curve fitting with the function worked quite well. The R –square correlation strengths are over 95% (Appendix M). An example of the fitting is presented in Figure 4.27.

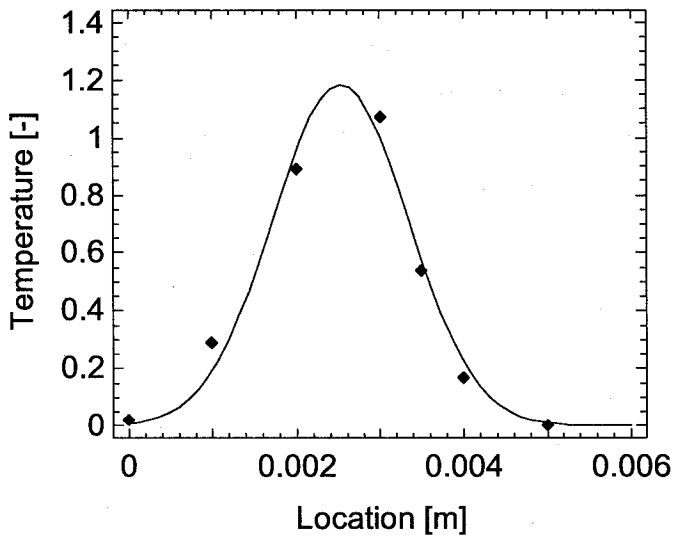

Figure 4.27 Curve fitting of a temperature profile segment used for the computation of the contrast values

The PH and MA average values of the fitted curves are presented for each thermogram in Appendix M and a summary of the results is presented in Table 4.6. The PH and MA values from each crack width were averaged over the different pressures and temperature differences conditions for each distance.

Table 4.6 PH and MA values averaged over the temperatures and the pressures differences

TESTS	width [m]	distance [m]	PH [-]	MA [-]
36,34,32,30,28,26	0.004	1.5	1.164	0.116
24,22,20,18,16,14	0.002	1.5	0.866	0.086
12,10,8,6,4,2	0.001	1.5	0.738	0.075
35,33,31,29,27,25	0.004	0.75	1.394	0.118
23,21,19,17,15,13	0.002	0.75	1.139	0.090
11,9,7,5,3,1	0.001	0.75	0.957	0.074

Influence of the experimental conditions on PH and MA values

Before establishing the calibration curves, the influence of the conditions on PH and MA values were studied as it was done above for the estimation of the dimensions using the segmentation method. All the averaged PH and MA computed from the same thermogram were plotted and linear regressions fitted (Figures 4.28, 4.29, 4.30) against the distance, and the temperature and pressure differences. According to the graphs, the pressure and temperature do not have influence on the PH and MA values. However, the different distances have a significant impact on the PH values computed.

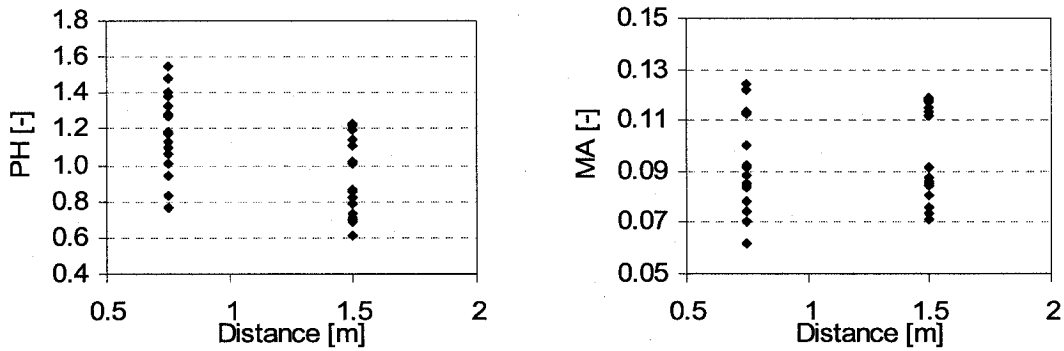

a) b)

Figure 4.28 PH (a) and MA (b) values against the distances

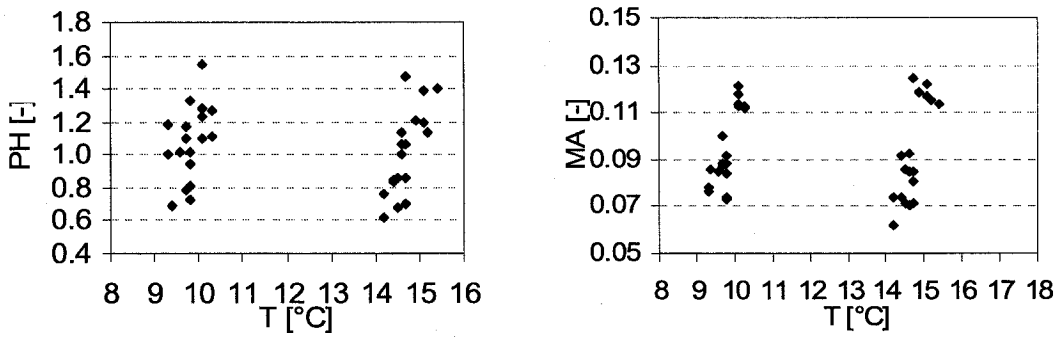

a) b)

Figure 4.29 PH (a) and MA (b) values against the temperature differences

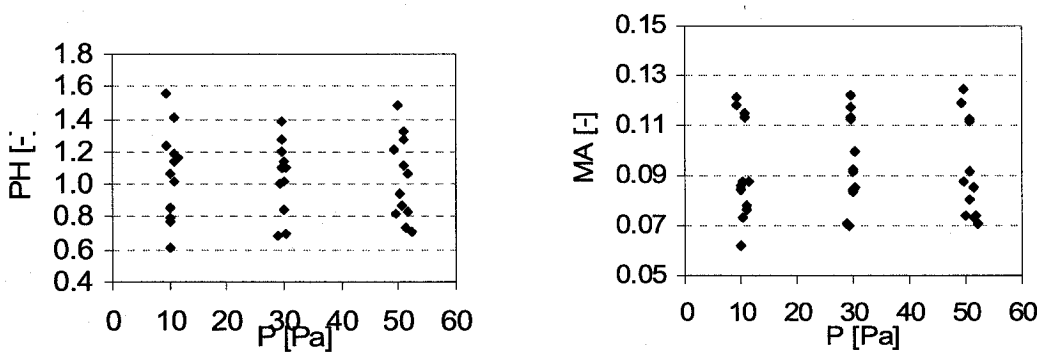

a) b)

Figure 4.30 PH (a) and MA (b) values against the pressure differences

The observations made on conditions influences on the PH and MA values led to the development of calibration curve for the different distances.

4.4.2.3 Calibration curves

The PH and MA values computed in the previous section were then used to establish calibration curves. These curves allow to estimate the crack width using the PH and MA values computed using the temperature profiles.

Calibration curves (Figure 4.31) were produced by plotting the PH and MA values against the crack widths. As the data were separated into series, for the two distances, the influence of the distance parameter on the calibration is highlighted. A linear function was fitted for each distance and the R-square value was depicted.

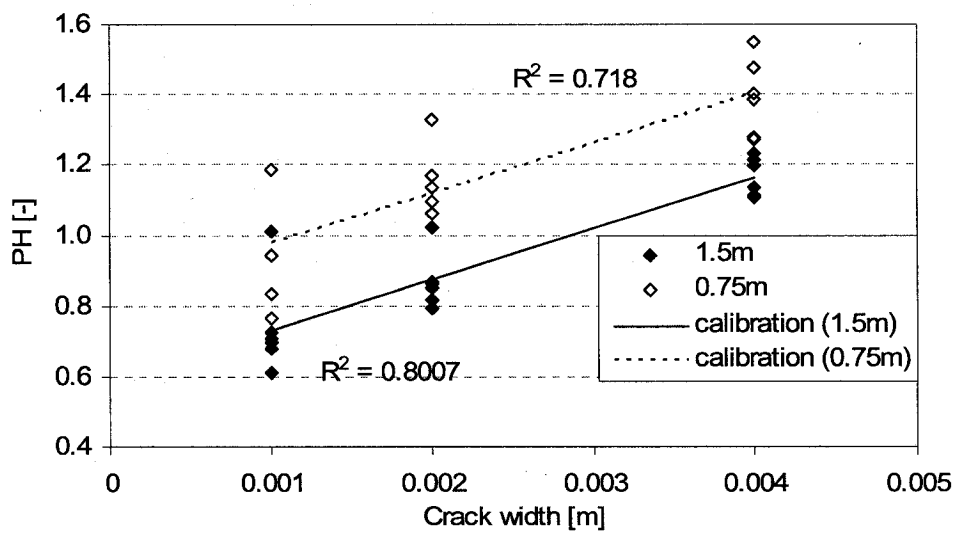

a)

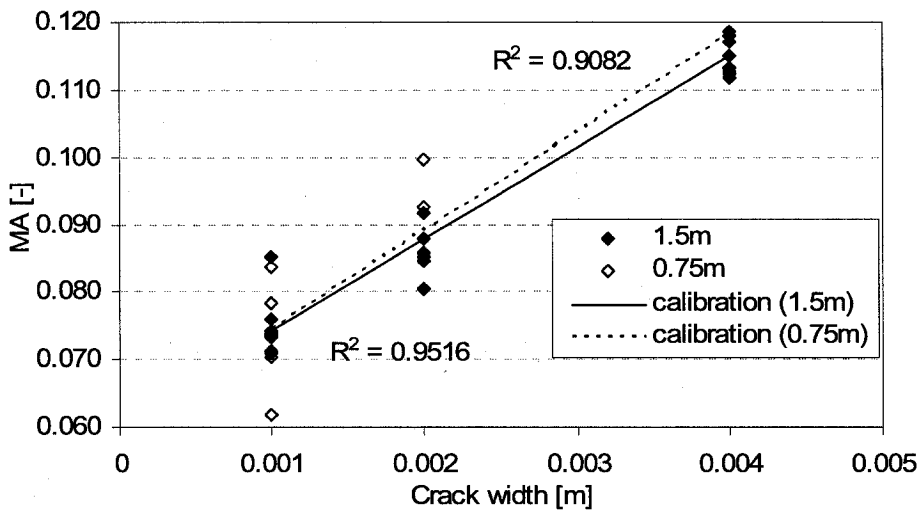

b)

Figure 4.31 Peak Height (a) and Missing Attenuation (b) calibration curves

The PH calibration curve depends on the distance, while the MA calibration curve is independent of the distance. Moreover, the MA values lead to higher R-squared values

for the regression than the PH values. According to these curves, the MA calibration is more accurate and independent of the conditions.

The PH and MA values computed from the experimental data were used to estimate the calibration curves established to estimate crack widths. Figure 4.32 shows the relation between these estimated widths and the measured widths. The plot includes a line with a slope equal to 1 where all the points should be if the estimation would be perfect.

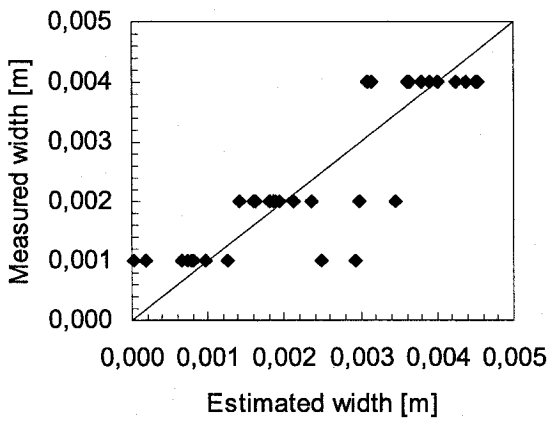

a)

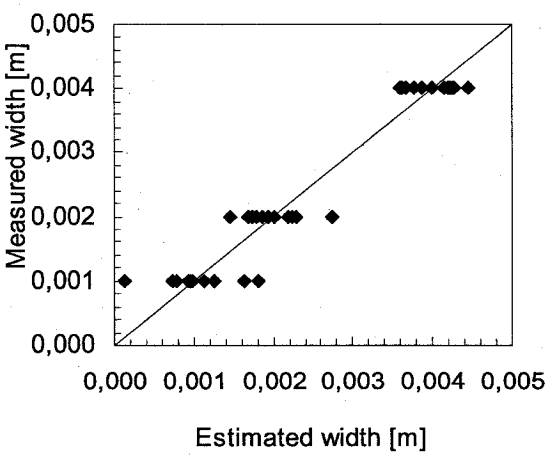

b)

Figure 4.32 Measured and estimated widths using PH (a) and MA (b) calibration curves

The study of the two graphs shows that, first, predictions are more accurate for larger crack widths and, second, predictions are more accurate using the MA calibration curve. For example, estimation of the 1mm crack widths vary from 0 to 3mm using PH calibration curve while predicted widths of 4 mm crack vary from 3 to 4.5 mm. Also, estimated widths of 1mm crack vary from 0 to 3 mm using PH calibration curve while predicted widths vary from 0 to 2 mm using MA calibration curve.

4.4.2.5 Conclusions of the profile calibration method for crack sizing

The estimation of the crack width can be obtained using the profile calibration method. This method consists of the fitting of the crack transversal temperature profiles selected in the thermogram temperature matrix to a Gaussian curve. Then, the contrasts values peak height (PH) and missing attenuation (MA) are computed using the parameters of the fitted curve. Calibration curves are available to estimate crack widths having the computed contrast values. Using this method, the estimations of crack widths from 1 to 4 mm can be done. However, estimations of the crack widths are more accurate for larger crack widths. Also, using MA calibration curve, estimations of the width are more accurate and the same calibration curve can be used for the different conditions tested.

4.5 Conclusion of the sizing techniques

Two methods have been developed for crack width measurement using thermographic data. Using the segmentation technique, crack lengths and large widths can be graphically estimated using the temperature gradients computations. For smaller

crack widths, correlation-based models are established, in addition, to predict the crack widths. Using the calibration techniques, the crack widths can be estimated using contrast values, namely PH and MA, computed from temperature profiles fitting and established calibration curves.

The efficiency of the two methods for the measurement of the smallest crack width tested can be compared: the estimated widths of 1mm crack vary from 0.5 to 1.5 mm using the segmentation technique and the correlation-based model while they vary from 0 to 2 mm using MA calibration curve of the profile calibration technique. For a 4mm crack width, the width were estimated width to be 4.3mm while using the calibration method a 4 mm width is estimated to range from 3.5 to 4.5mm.

In the next section of the thesis, issues related to the use of the results from these two methods in terms of crack areas are studied and discussed.

4.5 Potential use of the methodology

The first stage of the analysis highlighted relations between temperature distributions from thermography and crack dimensions: the temperature profile shape and the temperature at the crack location. Based on these relationships, two methods were developed for crack sizing using temperature profiles.

One principal aim of quantifying air leaks through the building envelope is the use of these quantities in modeling the building energy consumption for the analysis of the effects of retrofit measures. It was stated in the literature review (Section 2.2.3.) that building energy consumption models use the effective leakage area (ELA) or the air change per hour (ACH) as inputs for setting the airtightness of the building envelope.

Infrared thermography, as demonstrated in the preceding sections, can lead to quite exact dimensioning of crack sizes. If these crack dimensions could be used to adjust either the values of ELA or ACH that would results from the sealing of the measured cracks, the impact of these sealing measures on the overall energy consumption of a building could be calculated.

4.5.1 Crack areas and ELA

A first attempt would be to directly subtract from the ELA the crack measured. The use of crack dimensions to directly subtract and areas to ELA is represented in Figure 4.33:

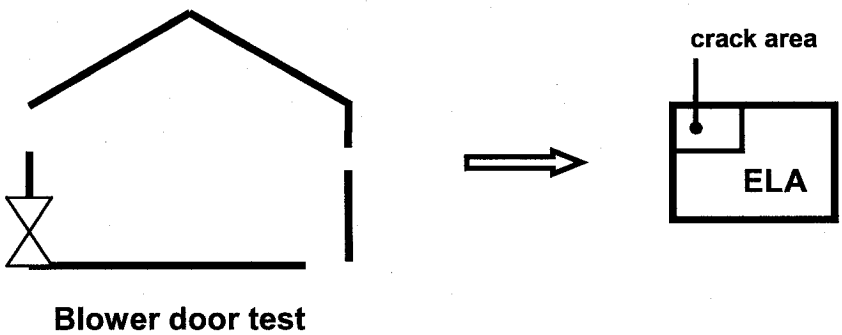

Figure 4.33 The potential use of the measured crack areas: direct subtraction of the areas measured to the ELA

However, it was explained in the literature review that the calculation of effective leakage area provides the area of one large opening that would produce the same flow as measured in the whole building at the reference pressure. The openings across the building envelopes are, however, seldom single and large; cracks are rather small and scattered throughout building envelope. Hence, the ELA does not represent a physical reality in terms of crack area throughout a building envelope.

In order to assess the possibility of subtracting the crack areas measured directly from the ELA, the pressure differences measured across the panel tested and the corresponding flow measured with the Laminar Flow Element were used to calculate an ELA using the ELA equation (eq 2.18):

$$ELA = Q_{LFE} \frac{\sqrt{\rho/2 \cdot \Delta P}}{C_D} \tag{4.15}$$

where ELA is the equivalent leakage area; and

Q_{LFE} is the airflow measured with the laminar flow element [m^3/s];

ρ, the air density [kg/m^3];

ΔP, the reference pressure difference measured across the panel [Pa];

C_D, the discharge coefficient for a large opening, taken to 0.6.

In addition, the crack areas measured and the pressure differences measured across the tested panel were used to calculate an ELA using the ELA equation:

$$Q_E = \frac{area \cdot C_D}{\sqrt{\rho/2 \cdot \Delta p_m}} \tag{4.16}$$

where Q_E is the equivalent airflow calculated [m^3/s];

area, the measured crack area [m^2];

ρ, the air density [kg/m^3];

ΔP, the reference pressure difference measured across the panel [Pa];

C_D, the discharge coefficient for a large opening, taken to 0.6.

The ELA and the airflow calculated using equations 4.15 and 4.16 are presented, with the measured crack area pressure difference, and airflow, in Appendix N. Figure 4.34 shows the effective leakage area calculated (eq. 4.15) versus the crack area, and the

equivalent airflow calculated (eq. 4.16) versus the airflow measured with the laminar flow element.

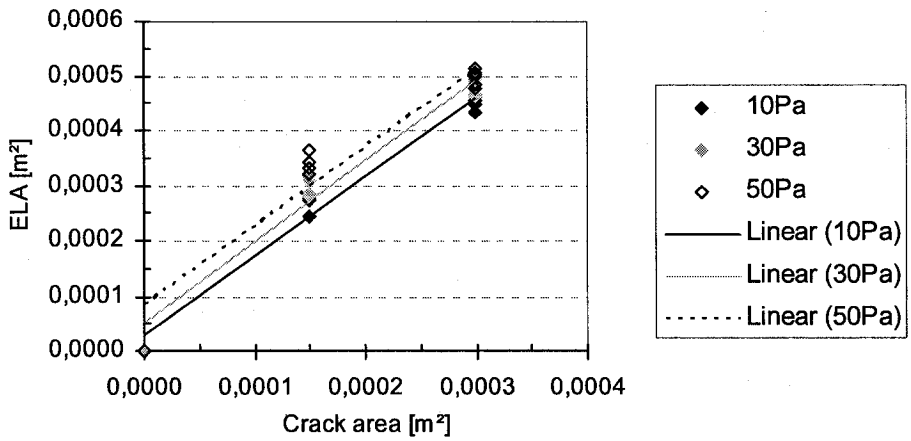

Figure 4.34 Calculated effective leakage area against measured crack areas

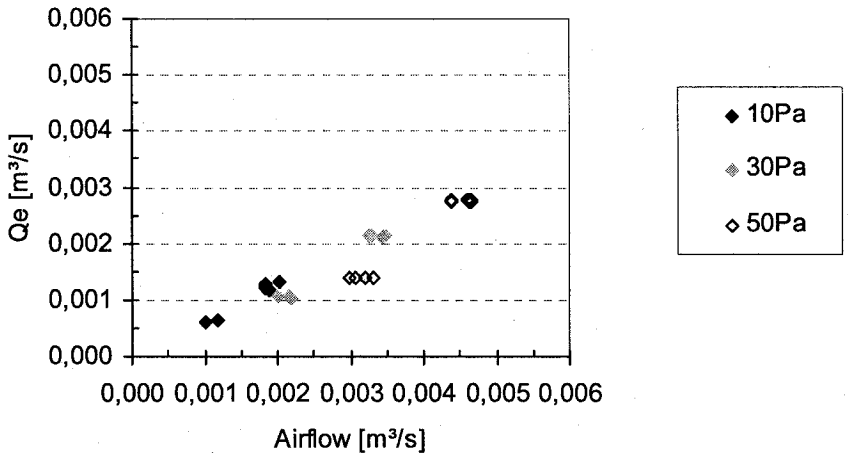

Figure 4.35 Calculated equivalent airflow rate and airflow rate measured

Figure 4.34 shows that the ELA calculation using the flow and the pressure differences measured (eq. 4.15) lead to larger areas than the crack areas measured. Also, the equivalent flow calculation using the crack area and the pressure difference measured

(eq. 4.16) lead to lower airflows than the air flow measured with the laminar flow element. However, the distribution of the data in Figure 4.34 shows that correlations could be established between measured areas and derived ELA's.

Therefore, it would be possible, using correlations established from empirical data models, to subtract an ELA equivalent to the crack area measured to the overall ELA of the building. These correlations-based models would change depending on the pressure difference to be used for the ELA calculation (4 and 10 Pa are commonly used as pressure differences for the calculation of the ELA, as explained in section 2.3.2).

The characteristics of the building envelope cracks are a more complex issue related to the use of the crack dimensions with overall airtightness measurement such as ELA.

4.5.2 Crack characteristics and power law

It was explained in the literature review that the power law is used to characterize the airflow through an entire building envelope combining the different kinds of opening characteristics of the building envelope. The power law describes the airflow through an entire building envelope with an exponent n and a coefficient C. These parameters are measured for a building envelope in the field by a blower door test using a blower door (Section 2.3.2). The power law is:

$$Q = C \cdot \Delta p^n \qquad (2.17)$$

where Q is the total flow through the building envelope (m^3/s);

Δp, the pressure difference through the building envelope; and

C and n, respectively the flow coefficient [$m^3/s/Pa^n$] and exponent [-].

Since the crack characteristics have an influence on the power law equation fitted for a building envelope and the power law is used to calculate the ELA, possible correlation-based models established between crack areas and ELA following the method proposed (Section 4.5.1) would change with different buildings.

Also, the power law combines the different kinds of opening characteristics through the building envelopes. However, all the cracks of this building do not have the same characteristics. Figure 4.36 shows the infiltrations through different types of cracks through the building envelope during the blower door test. Therefore, the effect of the cracks that have different characteristics but the same area would have different effects on the overall airtightness.

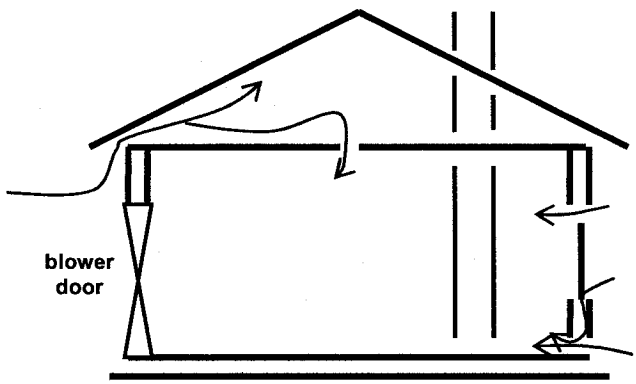

Figure 4.36 Infiltration through the different types of cracks during the blower door test

4.5.3 Description of the airflow through a building envelope crack

A test similar to a blower door test was carried out as a preliminary test before the principal experiment. The first objective of this test was first to assess the airtightness of the box with the tested panel installed closing the variable width crack opening. In addition, a set of pressure differences and flow was recorded for a 2mm crack width to

carry out a blower door test for the sealed box. The power law equation (2.3) was fitted to data so that C and n values can be computed using MatCAD (Appendix O). The fitted value of the exponent n was 0.6, which is near 0.65, a typical value measured when calculating the airtightness of building envelopes (Hutcheon and Handegord 1983). The difference with the value of 0.5 used, for large opening, in the equation for the ELA (eq. 2.218) explains the differences between flows and areas measured and calculated. Such exponent indicates, since it is closer to 0.5 than to 1 (Section 2.3.2), that the air flow through the crack tested is closer to turbulent flow in large short openings than to laminar flow for small long openings. This was a first step to mathematically describe a crack using experimental airflow measurements.

To fully grasp and understand the issues related to the combined use of single defect and overall building airtightness measurements, experiments must be done to study the quantification of airtightness of cracks and whole building. Heat and mass transfer and computed fluid dynamics models can also be used for the study of the airflow behavior through building envelope cracks.

Chapter 5 Conclusions

5.1 Summary and conclusions

The literature review presented the current possibilities when evaluating the building envelope performance. The focus was made on energy conservation related testing and details was given on airtightness assessment, e.g. the airtightness evaluation procedure, such as blower door test using an apparatus to measure the overall airtightness of an envelope. Then, infrared thermography as a technique for building envelope evaluation was introduced. The standard methods developed for building envelope evaluation were presented in details. During building overall airtightness measurement, infrared thermography can be used to precisely locate air leakage sites.

It was concluded that the development of a method to quantify air leak through the building envelope using thermography would be a timely contribution. The specific objective to this project was to develop a method for crack dimensioning.

The experimental set up developed for the development of such method was presented in details. Building envelope air leaks were reproduced in a simplified air leakage set up, using conditions similar to *in situ* surveys, inside an environment chamber. An experimental procedure was developed with special attention given to measure accurate absolute surface temperature distributions. The effectiveness of this method is presented and discussed. The parameters such as emissivity, ambient air relative humidity and temperature, and reflected temperature involved in temperature measurement using thermography can be measured so that temperature measurement can be adjusted. The reflected temperature is the parameter that appeared to be significant for adjustment of temperature under the tested conditions. The reference emitter technique

has been used for the correction of the temperature measured. The measured offset has been actually subtracted from the temperature measured. The error on absolute temperature measurement has been analyzed and computed: 0.6°C is the magnitude of the error on the measurements of a 20°C surface under the tested conditions. However, larger errors, more than 1°C, have been measured on temperatures measured during the experiment due probably to the use of a thermocouple as the contact temperature measurement instead of a RTD. It is possible also that the error was underestimated because of the assumptions made during the error analysis.

The qualitative comparisons of the thermograms showed noticeable changes between temperature patterns for the different pressure and temperature differences and crack dimensions. A complementary method has been proposed for the visualization of the air jet at the exit of the crack using a paper screen. The air jet behaves as a free air jet not affected by buoyancy effects. Also, the recirculation induced by the air jet in the room is not visible on the screen thermograms.

The lateral and longitudinal profiles were used to analyze the assembly surface temperature distributions and to estimate crack dimensions in the two dimensions separately. Relationships between temperature profiles shape and temperature measured at the crack location, and crack widths have been identified. However, stronger relationship possibilities were investigated.

Two methods were proposed for crack dimensioning: profile segmentation and calibration relationships established using thermal contrast. In the segmentation technique based on temperature profiles gradient computation, the temperature peaks appear where there are abrupt temperature changes at the crack limits. This method is efficient to

estimate lengths of 0.075m to 0.150 m with a difference of 5% with the measured length. Crack widths of 4mm can be measured within a difference of 8%. It has been demonstrated neither the pressure and temperature difference, nor the distance has an effect on dimensioning. In the case of 1 and 2mm crack width, the determination in the difference between measured and estimated width went up to 160%. Multilinear regression curves between estimated and real crack widths of these magnitudes have been determined. The distance is one variable to introduce in the regression to increase the correlation strength. Using this method, the estimated widths of 1mm cracks vary from 0.5 to 1.5 mm. The second method consists in fitting temperature profiles, computing thermal contrast values using the fittings, and establishing calibration curves between these contrast values and real crack widths. The fitting procedure has been successfully done on the appropriate sections of the temperature profiles. Two thermal contrast values, peak height (PH) and missing attenuation (MA), have been calculated from these fittings. The calibration curves were established between real crack width and these two parameters. Missing attenuation values drive not only to higher R-square values for the calibration of curve regressions, but also allow using one calibration curve for whichever experimental conditions. Effectively, pressure and temperature differences do not affect the PH and MA values while the PH values change with distance. Using this method, the estimated widths of 1mm cracks vary from 0 to 2 mm.

Therefore, relations exist between temperature profiles due to air leaks obtained from thermography, and experimental conditions and crack widths. Two methods developed in this project, analyzing simple cracks and assemblies, can be used for crack dimensioning from temperature profiles. However, these correlation-based methods are

camera and error dependant. Regressions and calibrations curves would have to be established for different cameras and would be affected by variations in camera accuracy.

Also, issues related to the combined use of single defect and overall building airtightness measurement must be studied since the ELA does not represent a physical reality in terms of total of crack distributed throughout a building envelope.

5.2 Contributions

The contributions of this research are the following:

1. An experimental methodology, in an environmental chamber, to reproduce air leak through a building envelope for infrared thermographic studies was developed;
2. A procedure for accurate assembly surface temperature distribution acquisition, including methods for parameters measurement and reference emitter technique using infrared thermography, and an evaluation of the effectiveness of the method for the actual experimental set up, was presented;
3. A complementary method for the visualization of leaking air jets was developed;
4. A data base of 36 thermograms was produced;
5. Relations between assembly surface temperature distributions due to air leaks and crack widths were analyzed and presented;
6. The development of two methods for crack dimensioning using infrared thermography led to the determination of correlation relationships.

5.3 Recommendations for future work

The following is recommended for future works towards the use of infrared thermography for quantification of air leaks:

1. To quantitatively investigate the effect of air leak paths through complex assemblies on thermogram temperature distributions.
2. To develop a method using infrared screen for the visualization and quantitative temperature distribution measurement of air jet from leak and combine the results with particle illuminated velocimetry measurement.
3. To numerically model air leaks through the building envelope with CFD and to use combined thermography and PIV results for the validation.
4. To investigate possibilities from image processing restoration techniques and pattern recognition for the improvement of temperature data obtain form thermograms in term of accuracy and spatial resolution and/or automatic air leak detection and quantification.
5. To investigate possibilities for the use of quantification of air leaks with commonly used airtightness parameters, such as ELA and ACH, and/or for calculation of moisture accumulation potential.

References

Arasteh, D.K., Beck, F.A., Griffith B.T., Byars, N. and M. Acevedo-Ruiz. 1992. Using the infrared thermography for the study of heat transfer through building envelope components. ASHRAE Transactions: Symposia, AN-92-6- 1, p.819-824.

ASHRAE. 2001. Handbook of Fundamentals, ASHRAE, Atlanta.

ASNT. 2005. Nondestructive Testing Handbook, third edition: Volume 3, Infrared and Thermal Testing, American Society for Nondestructive Testing, 732 p.

ASTM. 1987. Standard Test Method for Determining Airtightness Air Leakage Rate by Fan Pressurization. Standard E779, American Society for Testing and Material, Philadelphia.

ASTM. 1989. Standard Test Method for Steady-State Thermal Performance of Building Assemblies by Means of Guarded Hot Box. Standard C236, American Society for Testing and Material, Philadelphia.

ASTM. 1990a. Standard Test Method for Thermal Performance of Building Assemblies by Means of Calibrated Hot Box. Standard C976, American Society for Testing and Material, Philadelphia.

ASTM. 1990b. Standard Practice for Thermographic Inspection of Insulation Installations in Envelope Cavities of Frame Buildings. Standard C 1060, American Society for Testing and Material, Philadelphia.

ASTM. 1990c. Standard Practice for Calibrations Thin Heat Flux Transducers. Standard C1130, American Society for Testing and Material, Philadelphia.

ASTM. 1991a. Standard Test Method for Determining Rate of Air Leakage through Exterior Windows, Curtain Walls, and Doors under Specified Pressure Differences across the Specimen. Standard E283, American Society for Testing and Material, Philadelphia.

ASTM. 1991b. Standard Test Method for Determining Rate of Air Leakage through Exterior Windows, Curtain Walls, and Doors under Specified Pressure and Temperature Differences across the Specimen. Standard E1424, American Society for Testing and Material, Philadelphia.

ASTM. 1993a. Standard Test Methods for Determining Airtightness Air Change in a Single Zone by Means of a Tracer Gas Dilution. Standard E741, American Society for Testing and Material, Philadelphia.

ASTM. 1993b. Standard Test Method for Field Measurement of Air Leakage Through Installed Exterior windows and Doors. Standard E783, American Society for Testing and Material, Philadelphia.

ASTM. 1995a. Standard Practice for In-Situ Measurement of Heat Flux and Temperature on Building Envelope Components. Standard C1046, American Society for Testing and Material, Philadelphia.

ASTM. 1995b. Standard Practice for Determining Thermal Resistance of Building Envelope Components from In-Situ Data. Standard C1155, American Society for Testing and Material, Philadelphia.

ASTM. 1996. Standard Test Methods for Determining Airtightness of Buildings Using an Orifice Blower Door. Standard E1827, American Society for Testing and Material, Philadelphia.

ASTM.1997a. Standard Test Methods for Measuring and Compensating for Reflected Temperature Using Infrared Imaging Radiometers. Standard E 1862, American Society for Testing and Material, Philadelphia.

ASTM.1997b. Standard Test Methods for Transmittance of an Attenuating Medium Using Infrared Imaging Radiometers. Standard E 1897, American Society for Testing and Material, Philadelphia.

ASTM. 1997c. Standard Practice for Location of Wet Insulation in Roofing Systems Using Infrared Imaging. Standard C 1153, American Society for Testing and Material, Philadelphia.

ASTM. 1998. Standard Practices for Air Leakage Site Detection in Building Envelopes and Air Retarder Systems. Standard C 1186, American Society for Testing and Material, Philadelphia.

ASTM. 1999. Standard Test Methods for Measuring and Compensating for Emissivity Using Infrared Imaging Radiometers. Standard E 1833, American Society for Testing and Material, Philadelphia.

ASTM. 2005. Standard Test Method for Thermal Performance of Building Materials and Envelope Assemblies by Means of a Hot Box Apparatus. Standard C1363, American Society for Testing and Material, Philadelphia.

Ball, W.H. 1961. Thermal Insulation in Dwellings. CBD 16, Canadian Building Digests, Institute for Research in Construction, Ottawa, 7 p.

Cehlin, M., Moshfegh, B. and M. Sandberg. 2000. Visualization and Measurement of Air Temperature using Infrared Thermography. Air Distribution in Rooms, ROOMVENT 2000, Elsevier Sciences, p.339-347.

CGSB. 1986. Determination of the Airtightness of Building Envelopes by the Fan Depressurization Method. Standard CAN/CGSB-149.10-M86, Canadian General Standards Board.

CMHC. 1999. Woodframe Envelopes Best Practices Guide Building Technology, CMHC, Montreal.

Derome D., Desmarais, G., Finet, J.-P. and M. Bérubé,Dufour. 2004. Impact on implementation of retrofit measures by including infrared thermography in energy auditing, Proceedings of Performance of the Exterior Envelopes of Whole Buildings IX, ASHRAE , Clearwater Beach, U.S.A., 14 p.

Desmarais, G. 2000. Impact of Added Insulation on the Hygrothermal Performance of Leaky Exterior Wall Assembly. Master Thesis, Concordia University, Montreal, 213 p.

Dussault, S. 2004. Des gruyères flambant neufs, *Protégez-vous*, Montréal, Canada., pp. 10-13.

Elmahdy, H. 1996. Surface Temperature Measurement of Insulating Glass Units Using Infrared Thermography. ASHRAE Transactions, SA-96-6-2, p.489-496.

Energy Conservatory. 1998. APT System Software User's Guide. The Energy Conservatory, Minneapolis, 156 p.

Flanders, S. 1994. Heat Flux Transducers Measure In-Situ Building Thermal Performance. Journal of thermal insulation and building envelopes, Vol.18, July Issue, p. 28-52.

FLIR. 2004. ThermaCAM S60 Operator's manual. FLIR Systems, Danderyd, 174 p.

FLIR. 2003. ThermaCAM Researcher User's manual. FLIR Systems, Danderyd, 136 p.

Garden, G.K. 1963. Rain Penetration and its Control. CBD 40, Canadian Building Digests, Institute for Research in Construction, Ottawa, 5 p.

Ge, H. 2002. Study on overall performance of metal curtain walls. Ph.D. Thesis, Concordia University, Montreal, 296 p.

Ge, H. and P. Fazio. 2001. Study on Thermal Performance of curtain walls using Infrared Thermography. Proceedings of the International Conference on Building Envelope Systems and Technologies, Ottawa, p.231-235.

Gonzalez, R.C. and R.E. Woods. 1992. Digital Image Processing. Addison-Wesley, Reading MA.,716 p.

Griffith, B.T. and D. Arashteh. 1999. Buildings research using infrared imaging radiometers with laboratory thermal chamber. Thermosense XXI, Proceedings of SPIE, Vol. 3700, p.502-513.

Griffith, B.T., Arasteh, D., Beck, F. and D. Türler. 1995. Issues Associated with the Use of Infrared Thermography for experimental Testing of Insulated Systems. Proceedings of Performance of the Exterior Envelopes of Whole Buildings VI, ASHRAE , Clearwater Beach, U.S.A., pp. 515-525.

Handegord, G.O. 1960. Vapour Barriers in Home Construction. CBD 9, Canadian Building Digests, Institute for Research in Construction, Ottawa, 5 p.

Hart, J.M. 1991. A practical guide to infra-red thermography for building surveys. Building Research Establishment, Watford, 92 p.

Hassani, V.A. 1994. Application of infrared thermography to room air temperature measurements. ASHRAE Transactions, OR-94-21-3, p.1238-1247.

Hutcheon, N.B. and G.O.P. Handegord. 1983. Building Science for a Cold Climate. National Research Council of Canada, Ottawa, 434 p.

ISO. 1983. Qualitative detection of thermal irregularities in building envelopes- Infrared method. Standard 6781, International Organization for Standardization, Switzerland, 12 pages.

Janssens, A. 1998. Reliable Control of Interstitial Condenstaion in Lightweight Roof Systems. Ph.D. Thesis, Catholic University of Leuven, Belgium 217 p.

Latta J.K. 1962. Water and Building Materials. CBD 30, Canadian Building Digests, Institute for Research in Construction, Ottawa, 6 p.

Latta, J.K. 1976. Vapour Barriers: What are they? Are they Effective?. CBD 175, Canadian Building Digests, Institute for Research in Construction, Ottawa, 4 p.

Linden, E., Cehlin, M. and M.Sandberg. 2000. Temperature and Velocity Measurements on a diffuser for displacement ventilation with whole field methods. Air distribution in Rooms, ROOMVENT 2000, Elsevier Sciences, p.339-347.

Ludwig, N. and P. Teruzzi. 2002. Heat Losses and 3D diffusion phenomena for defect sizing procedures in video pulse thermography. Infrared physics & Technology 34, p.63-69.

Maldague, X.P.V. 1994. Infrared Methodology and Technology. Gordon and Breach, 525 p.

Maldague, X.P.V. 2001. Theory and Practice of Infrared Technology for Nondestructive Testing. John Wiley and Sons, Inc., New York, 671 p.

McQuiston, F.C., Parker, J.D. and J.D. Spitler. 2000. Heating, Ventilating, and Air Conditioning. Fifth Edition, John Wiley and Sons, Inc., New York, 623 p.

Meriam Instrument. Laminar Flow Elements, Installation and operation instructions. Meriam Instrument, Cleveland, 11p.

Öhman, C. 2001. Measurement in Thermography. FLIR Systems, Danderyd, 114 p.

Pettersson, P. and A. Bengt. 1980. Thermography, Testing of the Thermal Insulation and Airtightness of Buildings. Swedish Council for Building Research, Stockholm, 227 p.

Retrotec. 1993. Retrotec Operating Manual. Retrotec, Bellingham.

Riley M. 1993. The implementation of the AIM-2 Infiltration Model in Hot2000. CANMET, NRC, Ottawa, 35 p.

Sherman, M. 1992. A Power-Law Formulation of Laminar Flow in Short Pipes, Journal of Fluids Engineering, Vol.114, December issue, p. 601-605.

Türler, D., Griffith, B.T. and D.K Arasteh. 1997. Laboratory Procedures for Using Infrared Thermography Procedures to Validate Heat Transfer Models. Insulation Materials: Testing and Application: Third Volume, ASTM.

Walker, I.S. and D.J. Wilson. 1990. The Alberta Air Infiltration Model. Report 71, The University of Alberta, 39 p.

Walker, I.S., Wilson, D.J. and M.X. Sherman.1997. A comparison of the power law to quadratic formulations for air infiltration calculations, Energy and Buildings, Vol.27, No.3, June issue, 11 p.

Walpole, R.E. and R.H. Myers. 1989. Probability and Statistics for Engineers and Scientists. MacMillan, New York, 765p.

Williams,C.S. and O.A. Becklund. 1972. OPTICS: A Short Course for Engineers & Scientists. Wiley-Intersciences, New York, 397 p.

Wilson, A.G. 1961. Air Leakage in Buildings. CBD 23, Canadian Building Digests, Institute for Research in Construction, Ottawa, 6 p.

Zmeureanu R., Marceau, M.L., Payer, J. and D. Derome. 1998. Evaluation of Energy Performance of Nine Indentical Row Houses in Montreal. Proceedings of Performance of the Exterior Envelopes of Whole Buildings VII, ASHRAE, Clearwater Beach, p. 81-86.

Zmeureanu R. 2000. Cost-Effectiveness of Increasing Airtighness of Houses. Journal of Architectural Engineering, Vol.6, No 3, p.87-90.

Appendix A ThermaCAM S60 calibration curve

A.1 ThermaCAM S60 calibration curve

//

ThermaCAM S60

camera constants $R := 15016$ $B := 1398.7$ $F := 1$

$x := 153, 154.. 313$ (K)

$$I(x) := \frac{R}{\exp\left(\frac{B}{x}\right) - F}$$ (unit)

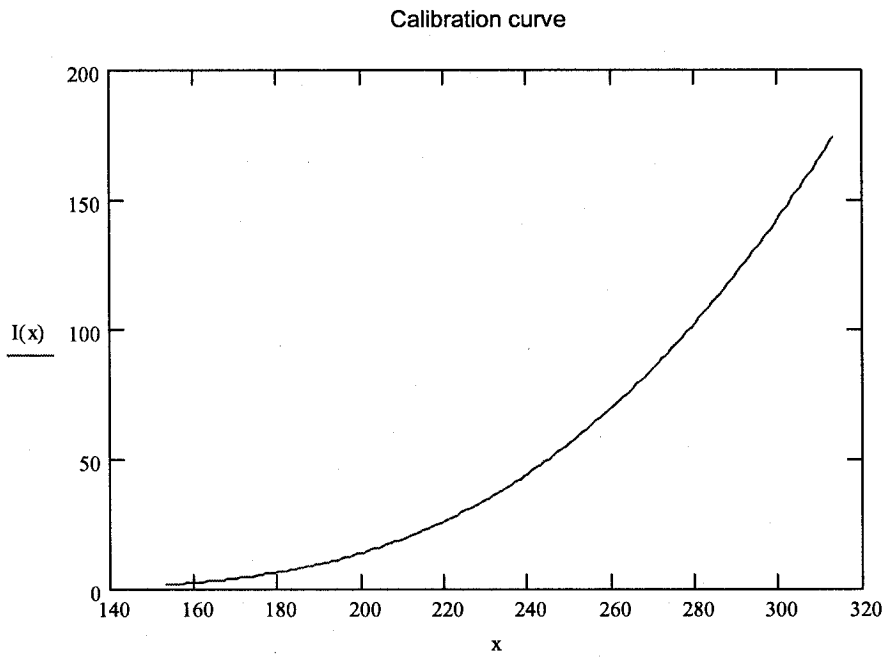

//

Appendix B Experimental conditions

TEST	**#**		
opening	0 mm		
ten minutes average			
amdiant temperature		0 °C	
air temperature		0 °C	
reference emitter		0 °C	
ten minutes before			
pressure			
		0 Pa	
flow			
	0 cfm	**LFE temp.**	**corr.**
corrected	0 cfm	0 °C	0
		density	
m3/s	0	0	
kg/s	0		
m3/s	0	0	
		air temp.	
		0 °C	
at thermogram recording time			
amdiant temperature		0 °C	
air temperature		0 °C	
reference emitter		0 °C	
pressure			
	0 Pa		
flow			
	0 cfm	**LFE temp.**	**corr.**
corrected	0 cfm	0 °C	0
		density	
m3/s	0	0	
kg/s	0		
m3/s	0	0	
		air temp.	
		0 °C	
distance			
0 m			

Figure B.1 Conditions parameters data sheet

Appendix C Experimental protocol

C.1 Experimental procedure

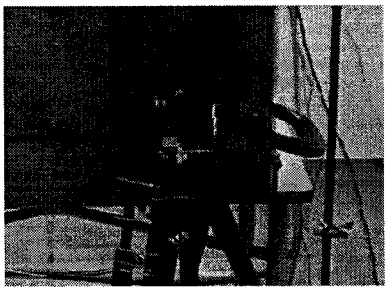

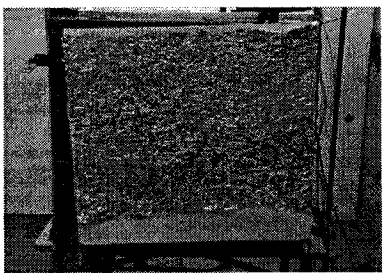

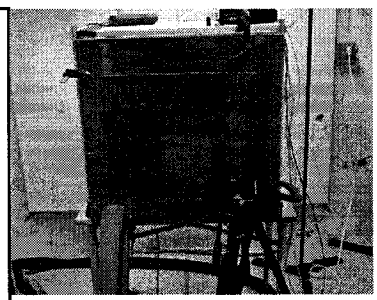

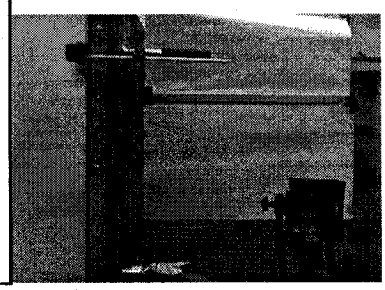

under stable testing conditions (36 tests)

1. Two preliminary tests

a. Emissivity measurement

Piece of plywood heated for the plywood emissivity measurement

b. Reflected temperature measurement

Aluminum foil used for the measurement of the reflected

2. Main test

Thermogram recording in front of the panel

Reference emitter used to estimate the temperature offset measured by the camera installed in the field of view of the tested panel thermograms

3. Supplementary test

Thermogram recording of the paper screen

Paper screen used for the recording of air jet temperature distribution visualization

DATA PROCESSING

C.2 Data processing procedure

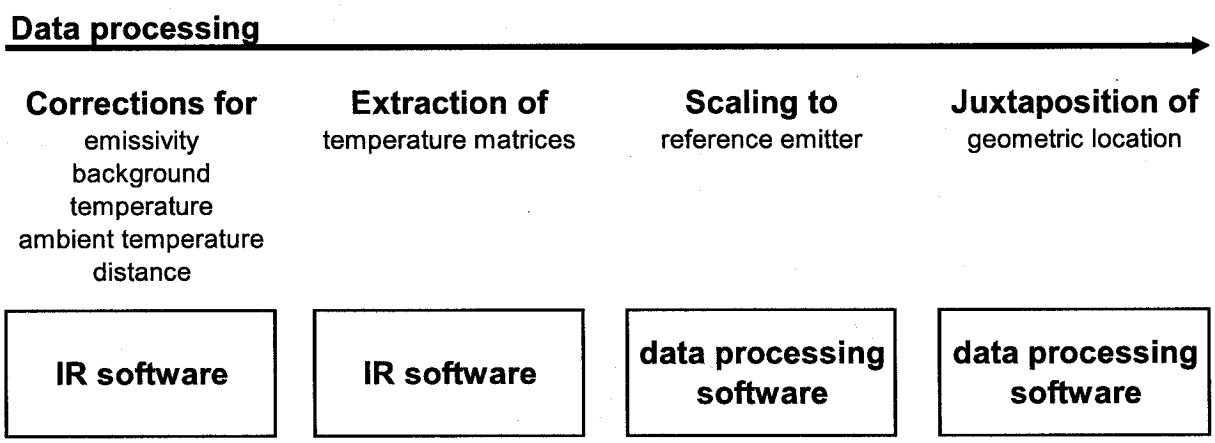

Appendix D Reference emitter

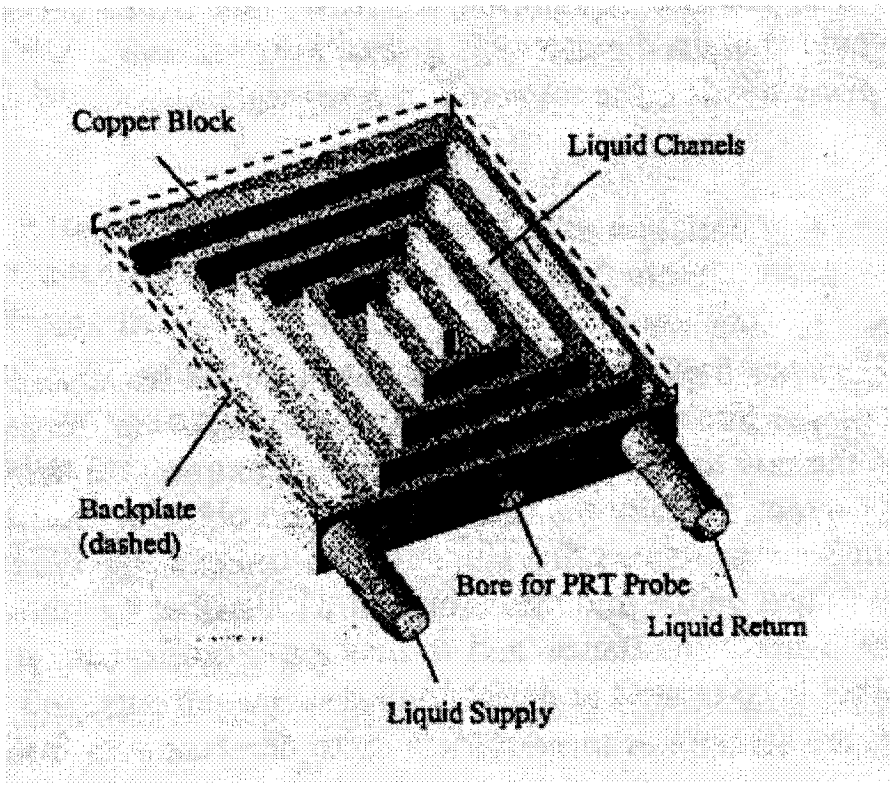

Figure D.1 Configuration of the reference emitter (from Griffith *et al* 1999)

Appendix E Error Analysis

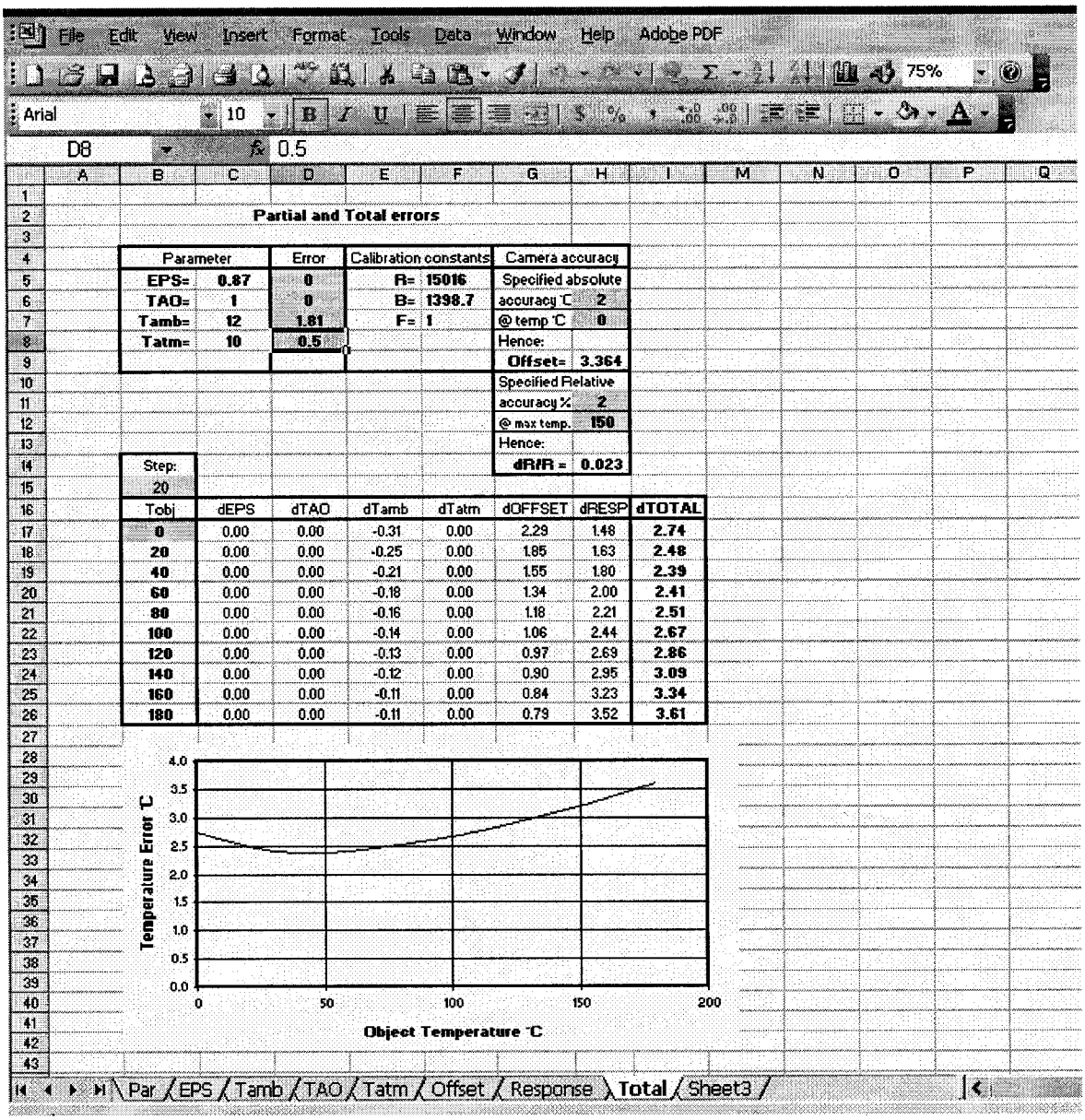

Partial and Total errors

Parameter		Error
EPS=	0.87	0
TAO=	1	0
Tamb=	12	1.81
Tatm=	10	0.5

Calibration constants	
R=	15016
B=	1398.7
F=	1

Camera accuracy	
Specified absolute accuracy °C	2
@ temp °C	0
Hence: Offset=	3.364
Specified Relative accuracy %	2
@ max temp.	150
Hence: dR/R =	0.023

Step: 20

Tobj	dEPS	dTAO	dTamb	dTatm	dOFFSET	dRESP	dTOTAL
0	0.00	0.00	-0.31	0.00	2.29	1.48	2.74
20	0.00	0.00	-0.25	0.00	1.85	1.63	2.48
40	0.00	0.00	-0.21	0.00	1.55	1.80	2.39
60	0.00	0.00	-0.18	0.00	1.34	2.00	2.41
80	0.00	0.00	-0.16	0.00	1.18	2.21	2.51
100	0.00	0.00	-0.14	0.00	1.06	2.44	2.67
120	0.00	0.00	-0.13	0.00	0.97	2.69	2.86
140	0.00	0.00	-0.12	0.00	0.90	2.95	3.09
160	0.00	0.00	-0.11	0.00	0.84	3.23	3.34
180	0.00	0.00	-0.11	0.00	0.79	3.52	3.61

Figure E.1 Error calculation results screen using 'Temp_err.xls'

E.2 Error analysis

//

RADIOMETRY

$$I_s = \frac{1}{\varepsilon \cdot \tau} \cdot I_{tot} - \frac{1-\varepsilon}{\varepsilon} \cdot I_a - \frac{1-\tau}{\varepsilon \cdot \tau} \cdot I_{atm}$$

CALIBRATION

$$Ts = \frac{B}{\ln\left(\frac{R}{I_s}\right)}$$

ThermaCAM S60

$R := 15016$

$B := 1398.7$

$F := 1$

Equivalent total temperature error

$\Delta T_{tot} := 0.08$ *(NDTE)*

ERROR CALCULATION

$$\Delta T = \sqrt{\left(\frac{\delta T_s}{\delta T_a} \cdot \Delta T_{ref}\right)^2 + \left(\frac{\delta T_s}{\delta T_{tot}} \cdot \Delta T_{tot}\right)^2}$$

($\Delta\varepsilon$=0, $\Delta\tau$=0 and Tatm no effect)

Conditions

$\varepsilon := 0.87$ $\tau := 1$

$T_s := 293$ $T_{ref} := 285$

$$I_{ref} := \frac{R}{\left(\frac{B}{e^{T_{ref}}} - F\right)}$$

$$I_s := \frac{R}{\left(\frac{B}{e^{T_s}} - F\right)}$$

$$I_{tot} := \varepsilon \cdot I_s + (1-\varepsilon) I_{ref}$$

$I_{ref} = 111.784$ $I_s = 127.95$ $I_{tot} = 125.848$

$$T_{tot} := \frac{B}{\ln\left(\frac{R}{I_{tot}}\right)}$$

$T_{tot} = 292.505$

Partial error Tref

$$\Delta T_{ref} := 0.5$$

$$\Delta T_s(T_{ref}) := \frac{1-\varepsilon}{\varepsilon} \cdot \frac{I_{ref}}{I_s} \cdot \frac{T_s^{\,2}}{T_{ref}^{\,2}} \cdot \Delta T_{ref}$$

$$\Delta T_s(T_{ref}) = 0.069$$

Partial error T

$$\Delta T_s(T_{tot}) := \frac{T_s^{\,2}}{I_s} \cdot \frac{1}{\varepsilon \cdot \tau} \cdot \frac{I_{tot}}{T_{tot}^{\,2}} \cdot \Delta T_{tot}$$

$$\Delta T_s(T_{tot}) = 0.091$$

IR total uncertainty

$$\Delta T = \sqrt{\Delta T_s(T_{ref})^2 + \Delta T_s(T_{tot})^2} \qquad \Delta T := \sqrt{0.069^2 + 0.091^2}$$

$$\Delta T = 0.114$$

IR TOTAL UNCERTAINTY

$$\Delta T_{tc} := 0.5$$ *(uncertainty thermocouple)*

$$\Delta T_{total} := \Delta T + \Delta T_{tc} \qquad \Delta T_{total} = 0.614$$

//

Appendix F Measurement of experimental conditions

Table F.1 Testing conditions measured

TESTS	Width [m]	Distance [m]	T amb [°C]	T air [°C]	dT [°C]	dP [Pa]	Flow [m3/s]
1	0,001	0,75	10,9	25,1	14,2	10,0	0,0010
2	0,001	1,5	10,9	25,1	14,2	10,2	0,0010
3	0,001	0,75	10,6	25,2	14,6	29,4	0,0022
4	0,001	1,5	10,8	25,3	14,5	28,9	0,0022
5	0,001	0,75	10,7	25,1	14,4	51,8	0,0030
6	0,001	1,5	10,5	25,2	14,7	52,3	0,0032
7	0,001	0,75	10,8	20,1	9,3	11,0	0,0012
8	0,001	1,5	10,8	20,1	9,3	11,0	0,0012
9	0,001	0,75	10,3	20,1	9,8	30,0	0,0020
10	0,001	1,5	10,8	20,2	9,4	30,4	0,0020
11	0,001	0,75	10,3	20,1	9,8	50,1	0,0033
12	0,001	1,5	10,3	20,1	9,8	51,3	0,0031
13	0,002	0,75	10,6	20,3	9,7	11,5	0,0020
14	0,002	1,5	10,6	20,3	9,7	10,2	0,0018
15	0,002	0,75	10,6	20,3	9,7	30,4	0,0033
16	0,002	1,5	10,7	20,3	9,6	29,9	0,0033
17	0,002	0,75	10,5	20,3	9,8	50,8	0,0044
18	0,002	1,5	10,5	20,3	9,8	49,6	0,0044
19	0,002	0,75	10,6	25,3	14,7	10,0	0,0018
20	0,002	1,5	10,7	25,2	14,5	10,0	0,0018
21	0,002	0,75	10,6	25,2	14,6	30,1	0,0035
22	0,002	1,5	10,7	25,1	14,4	30,1	0,0035
23	0,002	0,75	10,7	25,3	14,6	51,6	0,0047
24	0,002	1,5	10,6	25,3	14,7	50,6	0,0046
25	0,004	0,75	9,9	20	10,1	9,4	0,0018
26	0,004	1,5	9,9	20	10,1	9,4	0,0018
27	0,004	0,75	9,8	19,9	10,1	29,8	0,0035
28	0,004	1,5	9,8	19,9	10,1	29,8	0,0035
29	0,004	0,75	9,7	20	10,3	50,8	0,0045
30	0,004	1,5	9,7	20	10,3	50,8	0,0045
31	0,004	0,75	9,6	25	15,4	10,7	0,0018
32	0,004	1,5	9,7	24,9	15,2	10,7	0,0018
33	0,004	0,75	9,7	24,8	15,1	29,8	0,0034
34	0,004	1,5	9,7	24,8	15,1	29,6	0,0034
35	0,004	0,75	10,5	25,2	14,7	49,8	0,0047
36	0,004	1,5	10,3	25,2	14,9	49,2	0,0047

Appendix G Dedicated software screen used for steady-state assessment

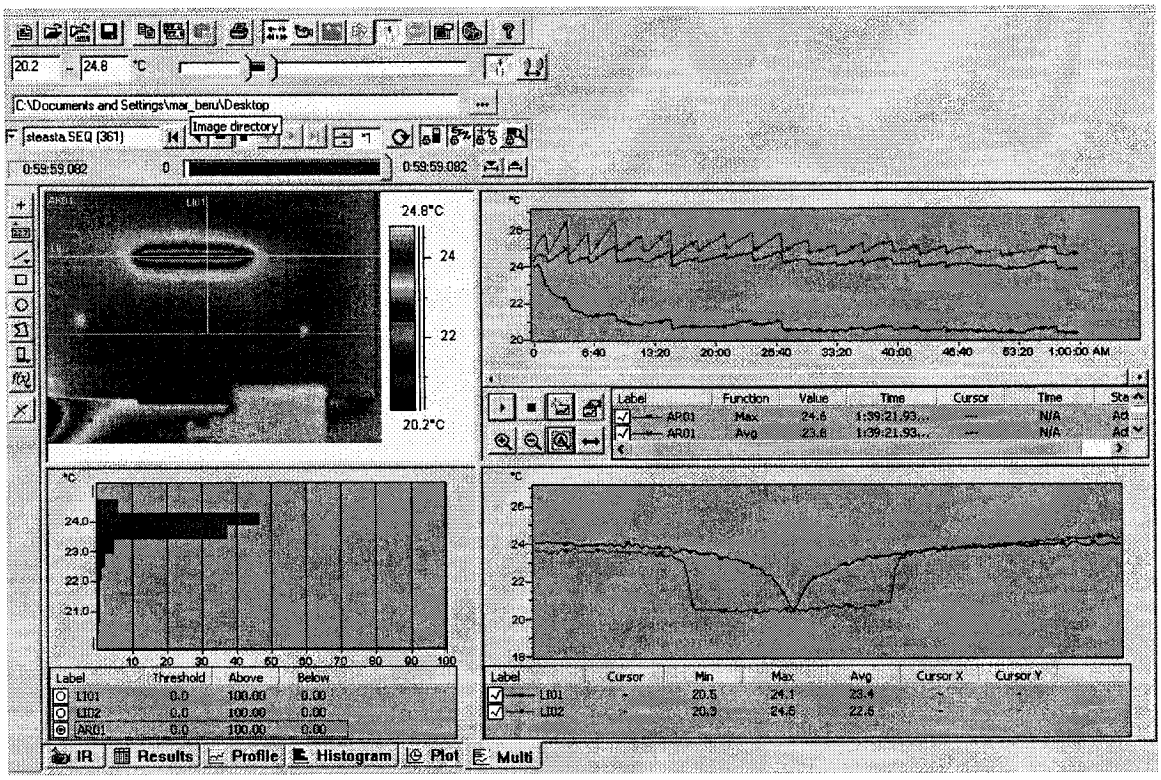

Figure G.1 Dedicated software screen used for steady-state assessment

Appendix H Relative magnitudes of radiation sources under the tested conditions

H.1 MathCAD Calculation of relative magnitudes of radiation sources under the tested conditions

//

Relative magnitude of radiation sources

camera constants $R := 15016$ $B := 1398.7$ $F := 1$

Radiation emitted

$T_s := 293$

$$I(T_s) := \frac{R}{\exp\left(\frac{B}{T_s}\right) - F} \quad \text{(unit)}$$

$I(T_s) = 127.95$

$\varepsilon := 0.87$

$Istot := \varepsilon \cdot I(T_s)$

$Istot = 111.316$

Radiation reflected

$T_{ref} := 285$

$$I(T_{ref}) := \frac{R}{\exp\left(\frac{B}{T_{ref}}\right) - F} \text{(unit)}$$

$I(T_{ref}) = 111.784$

$Ireftot := (1 - \varepsilon) \cdot I(T_{ref})$

$Ireftot = 14.532$

$Itot := Istot + Ireftot$ $Itot = 125.848$

$\frac{Istot}{Itot} = 0.885$

$\frac{Ireftot}{Itot} = 0.115$

88% of the radiation that reach the detector is radiation emitted while 12% is reflected radiation of the background

//

Appendix I Comparison between linear and nonlinear corrections

I.1 Comparison between linear and nonlinear corrections for a 20°C surface

//

REFERENCE EMITTER NON LINEAR CORRECTION

camera constants $R := 15016$ $B := 1398.7$ $F := 1$

non linear correction on a 20C surface
equivalent to a temperature linear correction of 0.5C on a 10C reference

---

Reference Emitter Radiation

$Ts1 := 283$

$$I(Ts1) := \frac{R}{\exp\left(\frac{B}{Ts1}\right) - F} \text{ (unit)}$$

$I(Ts1) = 107.946$

$T_{ref} := 285$

$$I(T_{ref}) := \frac{R}{\exp\left(\frac{B}{T_{ref}}\right) - F} \text{ (unit)}$$

$I(T_{ref}) = 111.784$

$\varepsilon := 0.87$

$Is1tot := \varepsilon \cdot I(Ts1)$

$Is1tot = 93.913$

$Ireftot := (1 - \varepsilon) \cdot I(T_{ref})$

$Ireftot = 14.532$

$I1tot := Is1tot + Ireftot$ $I1tot = 108.445$ (unit)

Measured Reference Emitter Radiation

$Ts2 := 283.5$

$$I(Ts2) := \frac{R}{\exp\left(\frac{B}{Ts2}\right) - F} \text{ (unit)}$$

$I(Ts2) = 108.898$

$T_{ref} := 285$

$$I(T_{ref}) := \frac{R}{\exp\left(\frac{B}{T_{ref}}\right) - F} \text{ (unit)}$$

$I(T_{ref}) = 111.784$

$\varepsilon := 0.87$

$Is2tot := \varepsilon \cdot I(Ts2)$

$Is2tot = 94.741$

$Ireftot := (1 - \varepsilon) \cdot I(T_{ref})$

$Ireftot = 14.532$

$I2tot := Is2tot + Ireftot$ $I2tot = 109.273$ (unit)

Radiation correction

$109.273 - 108.445 = 0.828$ (unit)

Surface Radiation

$Ts3 := 293$

$$I(Ts3) := \frac{R}{\exp\left(\frac{B}{Ts3}\right) - F} \text{ (unit)}$$

$I(Ts3) = 127.95$

$\varepsilon := 0.87$

$Is3tot := \varepsilon \cdot I(Ts3)$

$Is3tot = 111.316$

$T_{ref} := 285$

$$I(T_{ref}) := \frac{R}{\exp\left(\frac{B}{T_{ref}}\right) - F} \text{ (unit)}$$

$I(T_{ref}) = 111.784$

$Ireftot := (1 - \varepsilon) \cdot I(T_{ref})$

$Ireftot = 14.532$

$I3tot := Is3tot + Ireftot$ $I3tot = 125.848$ (unit)

Measured Surface Radiation

$I4tot := 125.848 + 0.828$

$I4tot = 126.676$

$Is4tot := I4tot - Ireftot$

$Is4tot = 112.144$ $R := 15016$ $B := 1398.7$ $F := 1$

$$I4 := \frac{Is4tot}{\varepsilon}$$

$I4 = 128.901$

$$Ts4 := \frac{B}{\ln\left(\frac{R}{128.901 - F}\right)}$$

$Ts4 = 293.498$

non linear correction

$\Delta T := Ts4 - Ts3$

$\Delta T = 0.498$

I.2 Comparison between linear and nonlinear corrections for a 25°C surface

//

REFERENCE EMITTER NON LINEAR CORRECTION

camera constants $R := 15016$ $B := 1398.7$ $F := 1$

non linear correction on a 20C surface
equivalent to a temperature linear correction of 0.5C on a 10C reference

---

Reference Emitter Radiation

$Ts1 := 283$

$$I(Ts1) := \frac{R}{\exp\left(\frac{B}{Ts1}\right) - F} \text{ (unit)}$$

$I(Ts1) = 107.946$

$\varepsilon := 0.87$

$Is1tot := \varepsilon \cdot I(Ts1)$

$Is1tot = 93.913$

$T_{ref} := 285$

$$I(T_{ref}) := \frac{R}{\exp\left(\frac{B}{T_{ref}}\right) - F} \text{ (unit)}$$

$I(T_{ref}) = 111.784$

$Ireftot := (1 - \varepsilon) \cdot I(T_{ref})$

$Ireftot = 14.532$

$I1tot := Is1tot + Ireftot$ $I1tot = 108.445$ (unit)

Measured Reference Emitter Radiation

$Ts2 := 283.5$

$$I(Ts2) := \frac{R}{\exp\left(\frac{B}{Ts2}\right) - F} \text{ (unit)}$$

$I(Ts2) = 108.898$

$\varepsilon := 0.87$

$Is2tot := \varepsilon \cdot I(Ts2)$

$Is2tot = 94.741$

$T_{ref} := 285$

$$I(T_{ref}) := \frac{R}{\exp\left(\frac{B}{T_{ref}}\right) - F} \text{ (unit)}$$

$I(T_{ref}) = 111.784$

$Ireftot := (1 - \varepsilon) \cdot I(T_{ref})$

$Ireftot = 14.532$

$I2tot := Is2tot + Ireftot$ $I2tot = 109.273$ (unit)

Radiation correction

$109.273 - 108.445 = 0.828$ (unit)

Surface Radiation

$Ts3 := 298$

$I(Ts3) := \frac{R}{\exp\left(\frac{B}{Ts3}\right) - F}$ (unit)

$I(Ts3) = 138.718$

$T_{ref} := 285$

$I(T_{ref}) := \frac{R}{\exp\left(\frac{B}{T_{ref}}\right) - F}$ (unit)

$I(T_{ref}) = 111.784$

$\varepsilon := 0.87$

$Is3tot := \varepsilon \cdot I(Ts3)$

$Is3tot = 120.685$

$Ireftot := (1 - \varepsilon) \cdot I(T_{ref})$

$Ireftot = 14.532$

$I3tot := Is3tot + Ireftot$ $I3tot = 135.217$ (unit)

Measured Surface Radiation

$I4tot := 135.217 + 0.828$

$I4tot = 136.045$

$Is4tot := I4tot - Ireftot$

$Is4tot = 121.513$ $R := 15016$ $B := 1398.7$ $F := 1$

$I4 := \frac{Is4tot}{\varepsilon}$

$I4 = 139.67$

$T4 := \frac{B}{\ln\left(\frac{R}{139.67 - F}\right)}$

$T4 = 298.563$

non linear correction

$\Delta T := T4 - Ts3$

$\Delta T = 0.563$

Table I.3 Temperature offsets measured over the reference emitter

Test	T ref [°C]	T ir ref [°C]	T [°C]
1	10.6	10.7	-0.1
2	10.6	10.8	-0.2
3	10.4	10.4	0
4	10.5	10.7	-0.2
5	10.5	10.7	-0.2
6	10.4	10.6	-0.2
7	10.4	10.4	0
8	10.4	10.8	-0.4
9	10.3	10.3	0
10	10.4	10.4	0
11	10.4	10.4	0
12	10.3	10.4	-0.1
13	10.4	10.1	0.3
14	10.4	10.8	-0.4
15	10.4	10.4	0
16	10.4	10.5	-0.1
17	10.4	10.5	-0.1
18	10.4	10.5	-0.1
19	10.3	10.3	0
20	10.4	10.6	-0.2
21	10.4	10.3	0.1
22	10.4	10.6	-0.2
23	10.5	10.5	0
24	10.4	10.7	-0.3
25	10.4	10.7	-0.3
26	10.3	10.4	-0.1
27	10.4	10.6	-0.2
28	10.3	10.4	-0.1
29	10.4	10.9	-0.5
30	10.4	10.7	-0.3
31	10.4	10.6	-0.2
32	10.5	10.7	-0.2
33	10.4	10.9	-0.5
34	10.5	10.9	-0.4
35	10.5	10.9	-0.4
36	10.5	10.7	-0.2

Appendix J Temperature measured at the crack location

Table J.1 Temperatures measured at the crack location

Test	Width [mm]	distance [m]	dP [Pa]	T TC [°C]	mean T IR [°C]	σ [°C]	dT [°C]
1	1	0.75	10	25.1	22.2	1.7	-2.9
2	1	1.5	10	25.1	21.4	1.1	-3.7
3	1	0.75	30	25.2	23.3	1.2	-1.9
4	1	1.5	30	25.3	21.8	1.9	-3.5
5	1	0.75	50	25.1	23.6	0.8	-1.5
6	1	1.5	50	25.2	22.1	0.9	-3.1
7	1	0.75	10	20.1	19.7	0.6	-0.4
8	1	1.5	10	20.1	18.9	0.5	-1.2
9	1	0.75	30	20.1	19.6	0.5	-0.5
10	1	1.5	30	20.2	18.6	0.3	-1.6
11	1	0.75	50	20.1	19.3	0.5	-0.8
12	1	1.5	50	20.1	18.7	0.3	-1.4
13	2	0.75	10	20.3	20.6	0.4	0.3
14	2	1.5	10	20.3	19	0.5	-1.3
15	2	0.75	30	20.3	20.2	0.6	-0.1
16	2	1.5	30	20.3	19.2	0.3	-1.1
17	2	0.75	50	20.3	20.5	0.4	0.2
18	2	1.5	50	20.3	19.2	0.5	-1.1
19	2	0.75	10	25.3	24.6	0.8	-0.7
20	2	1.5	10	25.2	23.7	0.6	-1.5
21	2	0.75	30	25.2	24.9	0.6	-0.3
22	2	1.5	30	25.1	23.1	0.7	-2.0
23	2	0.75	50	25.3	25.2	0.3	-0.1
24	2	1.5	50	25.3	23.7	0.3	-1.6
25	4	0.75	10	20.0	20.8	0.4	0.8
26	4	1.5	10	20.0	20.3	0.4	0.3
27	4	0.75	30	19.9	20.2	0.2	0.3
28	4	1.5	30	19.9	18.9	0.7	-1.0
29	4	0.75	50	20.0	20.4	0.1	0.4
30	4	1.5	50	20.0	20.0	0.6	0.0
31	4	0.75	10	25.0	26.0	0.3	1.0
32	4	1.5	10	25.0	25.0	0.3	0.0
33	4	0.75	30	24.9	26.1	0.3	1.2
34	4	1.5	30	25.0	25.2	0.2	0.2
35	4	0.75	50	25.2	26.8	0.4	1.6
36	4	1.5	50	25.2	24.0	1.1	-1.2

Appendix K Estimated dimensions using segmentation technique

Table K.1 Estimated dimensions using segmentation technique

	Test Conditions					Analysis Results					
Tests	Width	Length	distance	T	P	estimated width	width	width	estimated length	lenght	lenght
	[m]	[m]	[m]	[°C]	[Pa]	[m]	[m]	[%]	[m]	[m]	[%]
1	0.001	0.15	0.75	14.2	10.0	0.002	0.001	100	0.156	0.006	4
2	0.001	0.15	1.5	14.2	10.2	0.003	0.002	200	0.152	0.002	1
3	0.001	0.15	0.75	14.6	29.4	0.002	0.001	100	0.152	0.002	1
4	0.001	0.15	1.5	14.5	28.9	0.003	0.002	200	0.148	-0.002	-2
5	0.001	0.15	0.75	14.4	51.8	0.002	0.001	100	0.158	0.008	5
6	0.001	0.15	1.5	14.7	52.3	0.003	0.002	200	0.149	-0.001	-1
7	0.001	0.15	0.75	9.3	11.0	0.002	0.001	100	0.155	0.005	3
8	0.001	0.15	1.5	9.3	11.0	0.002	0.001	100	0.153	0.003	2
9	0.001	0.15	0.75	9.8	30.0	0.002	0.001	100	0.163	0.013	9
10	0.001	0.15	1.5	9.4	30.4	0.003	0.002	200	0.155	0.005	3
11	0.001	0.15	0.75	9.8	50.1	0.002	0.001	100	0.158	0.008	6
12	0.001	0.15	1.5	9.8	51.3	0.002	0.001	100	0.152	0.002	1
13	0.002	0.15	0.75	9.7	11.5	0.003	0.001	50	0.161	0.011	7
14	0.002	0.15	1.5	9.7	10.2	0.004	0.002	100	0.151	0.001	1
15	0.002	0.15	0.75	9.7	30.4	0.003	0.001	50	0.156	0.006	4
16	0.002	0.15	1.5	9.6	29.9	0.004	0.002	100	0.155	0.005	3
17	0.002	0.15	0.75	9.8	50.8	0.003	0.001	50	0.161	0.011	7
18	0.002	0.15	1.5	9.8	49.6	0.003	0.001	50	0.150	0.000	0
19	0.002	0.15	0.75	14.7	10.0	0.003	0.001	50	0.151	0.001	1
20	0.002	0.15	1.5	14.5	10.0	0.004	0.002	100	0.155	0.005	3
21	0.002	0.15	0.75	14.6	30.0	0.003	0.001	50	0.160	0.010	6
22	0.002	0.15	1.5	14.4	30.0	0.004	0.002	100	0.153	0.003	2
23	0.002	0.15	0.75	14.6	50.0	0.003	0.001	50	0.159	0.009	6
24	0.002	0.15	1.5	14.7	50.0	0.004	0.002	100	0.155	0.005	3
25	0.004	0.075	0.75	10.1	9.5	0.004	0.000	0	0.076	0.001	1
26	0.004	0.075	1.5	10.1	9.5	0.004	0.000	0	0.070	-0.005	-7
27	0.004	0.075	0.75	10.1	29.8	0.005	0.001	25	0.077	0.002	3
28	0.004	0.075	1.5	10.1	29.8	0.004	0.000	0	0.076	0.001	1
29	0.004	0.075	0.75	10.3	50.8	0.004	0.000	0	0.076	0.001	1
30	0.004	0.075	1.5	10.3	50.8	0.005	0.001	25	0.076	0.001	1
31	0.004	0.075	0.75	15	10.7	0.004	0.000	0	0.078	0.003	4
32	0.004	0.075	1.5	15	10.7	0.004	0.000	0	0.075	0.000	0
33	0.004	0.075	0.75	15.1	29.6	0.004	0.000	0	0.078	0.003	4
34	0.004	0.075	1.5	15.1	29.6	0.005	0.001	25	0.076	0.001	1
35	0.004	0.075	0.75	14.9	49.3	0.005	0.001	25	0.077	0.002	3
36	0.004	0.075	1.5	14.9	49.3	0.004	0.000	0	0.076	0.001	1

Appendix L Influence of conditions parameters on dimensions estimated

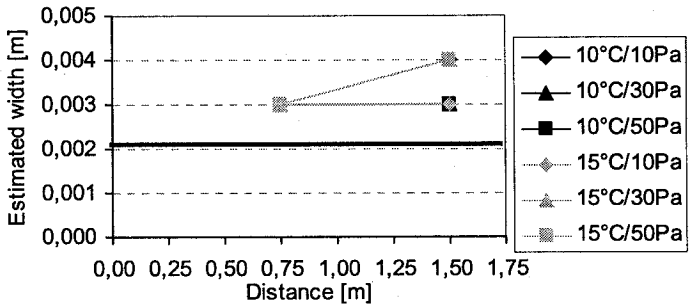

a)

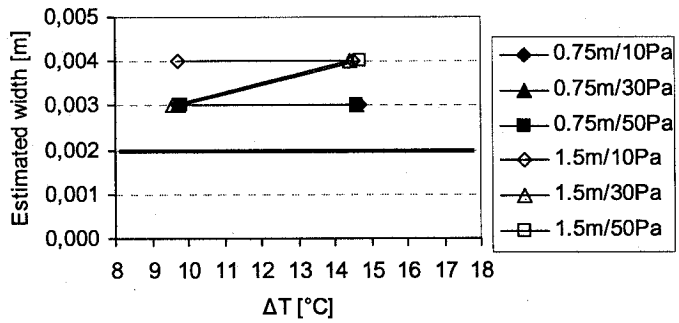

b)

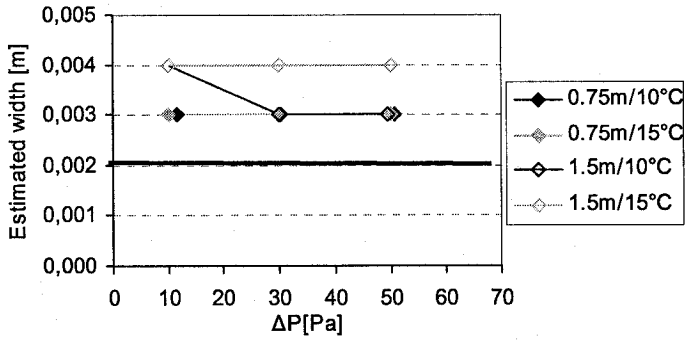

c)

Figure L.1 Estimated widths against distance (a) temperature difference (b) and pressure difference (c) for a 2mm width crack

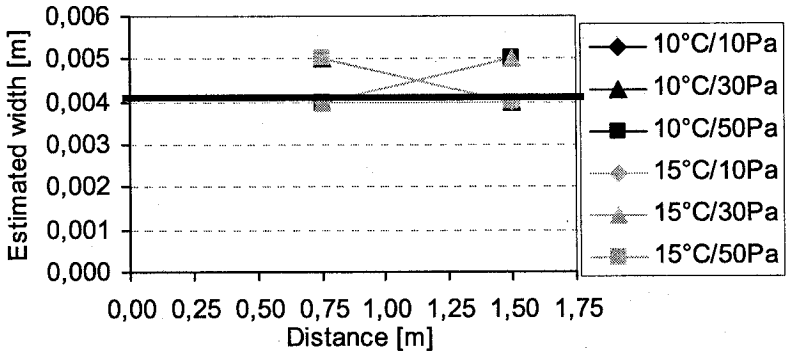

a)

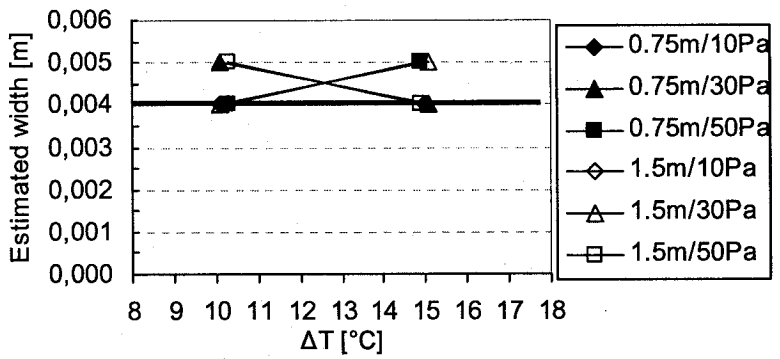

b)

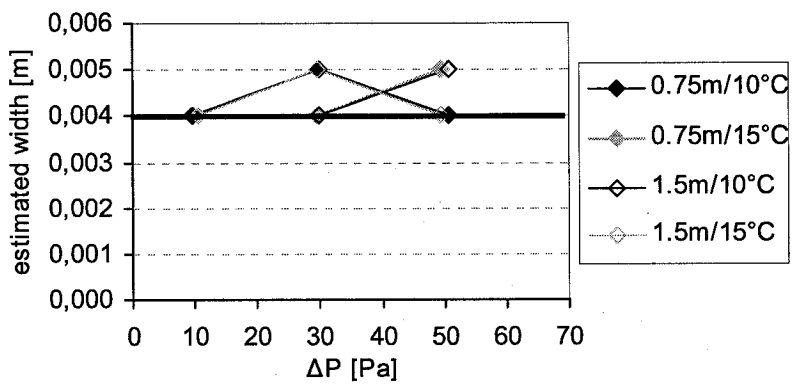

c)

Figure L.2 Estimated widths against distance (a) temperature difference (b) and pressure difference (c) for a 4mm width crack

Appendix M PH and MA values

Table M.1 PH and MA values computed

TEST	width [m]	distance [m]	t [°C]	p [Pa]	PH	σPH	MA	σMA	R^2 [%]
1	0.001	0.75	14.2	10.0	0.764	0.0532	0.0619	0.0017	97.21
2	0.001	1.5	14.2	10.2	0.613	0.0143	0.0736	0.0027	99.82
3	0.001	0.75	14.6	29.4	1.008	0.0163	0.0703	0.0019	97.45
4	0.001	1.5	14.5	28.9	0.681	0.0352	0.0711	0.0012	98.31
5	0.001	0.75	14.4	51.8	0.833	0.0238	0.0738	0.0010	99.57
6	0.001	1.5	14.7	52.3	0.705	0.0809	0.0710	0.0016	97.49
7	0.001	0.75	9.3	11.0	1.184	0.0409	0.0783	0.0009	99.36
8	0.001	1.5	9.3	11.0	1.008	0.0421	0.0760	0.0015	99.90
9	0.001	0.75	9.8	30.0	1.011	0.0210	0.0836	0.0008	98.02
10	0.001	1.5	9.4	30.4	0.693	0.0078	0.0852	0.0036	99.69
11	0.001	0.75	9.8	50.1	0.941	0.0224	0.0741	0.0012	97.38
12	0.001	1.5	9.8	51.3	0.726	0.0373	0.0732	0.0255	96.91
13	0.002	0.75	9.7	11.5	1.167	0.0246	0.0879	0.0023	99.44
14	0.002	1.5	9.7	10.2	0.790	0.0179	0.0877	0.0013	98.70
15	0.002	0.75	9.7	30.4	1.094	0.0234	0.0997	0.0019	97.74
16	0.002	1.5	9.6	29.9	1.017	0.0823	0.0846	0.0017	98.83
17	0.002	0.75	9.8	50.8	1.325	0.0313	0.0916	0.0011	98.60
18	0.002	1.5	9.8	49.6	0.816	0.0271	0.0878	0.0014	99.41
19	0.002	0.75	14.7	10.0	1.058	0.0156	0.0845	0.0014	96.96
20	0.002	1.5	14.5	10.0	0.859	0.0515	0.0858	0.0021	99.39
21	0.002	0.75	14.6	30.1	1.132	0.4763	0.0925	0.0008	96.50
22	0.002	1.5	14.4	30.1	0.847	0.0086	0.0917	0.0008	98.86
23	0.002	0.75	14.6	51.6	1.061	0.0157	0.0852	0.0009	97.15
24	0.002	1.5	14.7	50.6	0.864	0.0546	0.0804	0.0016	99.15
25	0.004	0.75	10.1	9.4	1.549	0.0300	0.1215	0.0008	98.16
26	0.004	1.5	10.1	9.4	1.232	0.0508	0.1178	0.0023	99.04
27	0.004	0.75	10.1	29.8	1.278	0.0220	0.1127	0.0013	98.04
28	0.004	1.5	10.1	29.8	1.104	0.0251	0.1133	0.0011	99.35
29	0.004	0.75	10.3	50.8	1.270	0.0762	0.1123	0.0019	99.15
30	0.004	1.5	10.3	50.8	1.108	0.0339	0.1119	0.0013	96.46
31	0.004	0.75	15.4	10.7	1.403	0.0536	0.1133	0.0025	98.37
32	0.004	1.5	15.2	10.7	1.134	0.0372	0.1150	0.0021	96.91
33	0.004	0.75	15.1	29.8	1.387	0.0269	0.1222	0.0017	99.77
34	0.004	1.5	15.1	29.6	1.195	0.0383	0.1169	0.0015	96.28
35	0.004	0.75	14.7	49.8	1.476	0.0652	0.1245	0.0030	97.89
36	0.004	1.5	14.9	49.2	1.213	0.0162	0.1184	0.0009	96.79

Appendix N Effective leakage areas calculated from flows measured for each test

Table N.1 Effective leakage areas calculated from flows measured for each test

	Measured conditions			Calculated	
	P	area	flow	ELA	Qe
TESTS	[Pa]	[m²]	[m³/s]	[m²]	[m³/s]
1	10.0	0.0002	0.0010	0.0002	0.0006
2	10.2	0.0002	0.0010	0.0002	0.0006
3	29.4	0.0002	0.0022	0.0003	0.0010
4	28.9	0.0002	0.0022	0.0003	0.0010
5	51.8	0.0002	0.0030	0.0003	0.0014
6	52.3	0.0002	0.0032	0.0003	0.0014
7	11.0	0.0002	0.0012	0.0003	0.0006
8	11.0	0.0002	0.0012	0.0003	0.0006
9	30.0	0.0002	0.0020	0.0003	0.0011
10	30.4	0.0002	0.0020	0.0003	0.0011
11	50.1	0.0002	0.0033	0.0004	0.0014
12	51.3	0.0002	0.0031	0.0003	0.0014
13	11.5	0.0003	0.0020	0.0005	0.0013
14	10.2	0.0003	0.0018	0.0004	0.0012
15	30.4	0.0003	0.0033	0.0005	0.0021
16	29.9	0.0003	0.0033	0.0005	0.0021
17	50.8	0.0003	0.0044	0.0005	0.0028
18	49.6	0.0003	0.0044	0.0005	0.0027
19	10.0	0.0003	0.0018	0.0005	0.0012
20	10.0	0.0003	0.0018	0.0005	0.0012
21	30.1	0.0003	0.0035	0.0005	0.0021
22	30.1	0.0003	0.0035	0.0005	0.0021
23	51.6	0.0003	0.0047	0.0005	0.0028
24	50.6	0.0003	0.0046	0.0005	0.0028
25	9.4	0.0003	0.0019	0.0005	0.0012
26	9.4	0.0003	0.0019	0.0005	0.0012
27	29.8	0.0003	0.0035	0.0005	0.0021
28	29.8	0.0003	0.0035	0.0005	0.0021
29	50.8	0.0003	0.0046	0.0005	0.0028
30	50.8	0.0003	0.0046	0.0005	0.0028
31	10.7	0.0003	0.0018	0.0004	0.0013
32	10.7	0.0003	0.0018	0.0004	0.0013
33	29.8	0.0003	0.0034	0.0005	0.0021
34	29.6	0.0003	0.0034	0.0005	0.0021
35	49.8	0.0003	0.0047	0.0005	0.0027
36	49.2	0.0003	0.0046	0.0005	0.0027

Appendix O Blower door test of the sealed box with the crack panel

O.1 Blower door test results and calculations

//

Sealed Box with the crack BLOWER DOOR Test

measured pressure[PA] and flow [m3/s]:

data :=

7.4726	0.0013
10.2126	0.0015
15.4435	0.0019
19.9271	0.0025
25.1580	0.0028
31.1361	0.0033
34.8724	0.0036
42.3451	0.0039
50.3160	0.0043
54.3014	0.0045
62.2722	0.0048
65.5104	0.0049
73.4812	0.0053
0.0000	0.0000

crack area

area := 0.3·0.002

area = $600.000000 \times 10^{-6}$

vx := data$^{\langle 0 \rangle}$

vy := data$^{\langle 1 \rangle}$

$$vg := \begin{pmatrix} 0.0011 \\ 0.5995 \\ 0 \end{pmatrix}$$

pwr := pwrfit(vx, vy, vg)

$pwr_0 = 417.131044 \times 10^{-6}$ $pwr_1 = 596.100669 \times 10^{-3}$ $pwr_2 = -51.980900 \times 10^{-6}$

$p(x) := pwr_0 \cdot x^{pwr_1} + pwr_2$

$p(50) = 4.243677 \times 10^{-3}$

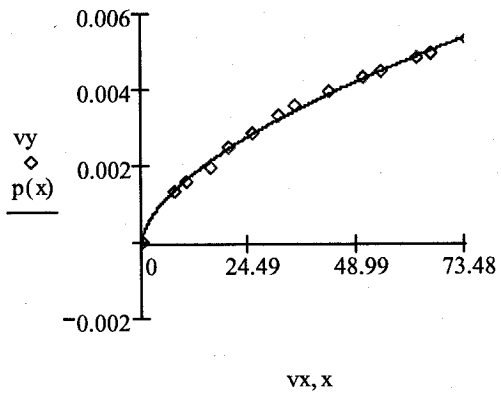

$C := pwr_0$

$C = 417.131044 \times 10^{-6}$

$n := pwr_1$

$n = 596.100669 \times 10^{-3}$

calculation of the ELA at 4Pa

$p := 4$

$Q := C \cdot p^n$

$Q = 953.149175 \times 10^{-6}$

$$ELA := Q \frac{\left(\frac{1 \cdot 1.2}{2 \cdot p}\right)^{0.5}}{0.6}$$

$ELA = 615.255147 \times 10^{-6}$

$ELA = 615.255147 \times 10^{-6}$

//